UNIVERSIDADE ESTADUAL PAULISTA

"JÚLIO DE MESQUITA FILHO"

CAMPUS DE GUARATINGUETÁ

VICTOR CORREA LATTARI

Analysis of Dust Production in Planetary Rings and Investigation of the Delivery of Water to the Terrestrial Planets During Planet Formation

Guaratinguetá

2024

Victor Correa Lattari

Analysis of Dust Production in Planetary Rings and Investigation of the Delivery of Water to the Terrestrial Planets During Planet Formation

Doctoral Thesis presented to the Graduate Program in Physics and Astronomy of the São Paulo State University "Júlio de Mesquita Filho" as a partial requirement to obtain the degree of Doctor in Physics and Astronomy

Supervisor: Prof. Dr. Rafael Sfair

Guaratinguetá

2024

Lattari, Victor Correa
L364a Analysis of dust production in planetary rings and investigation of the delivery of water to the terrestrial planets during planet formation / Victor Correa Lattari - Guaratinguetá, 2024.
117 f : il.
Bibliografia: f. 77-81

Tese (Doutorado) – Universidade Estadual Paulista, Faculdade de Engenharia e Ciências de Guaratinguetá, 2024.

Orientador: Prof. Dr. Rafael Sfair

1. Planetas. 2. Asteróides. 3. Sistema solar. 4. Astronomia. I. Título.

CDU 523.4(043)

Luciana Máximo
Bibliotecária/CRB-8/3595

unesp

UNIVERSIDADE ESTADUAL PAULISTA
CAMPUS DE GUARATINGUETÁ

VICTOR CORRÊA LATTARI

ESTA TESE FOI JULGADA ADEQUADA PARA A OBTENÇÃO DO TÍTULO DE
"DOUTOR EM FÍSICA"

PROGRAMA: FÍSICA
CURSO: DOUTORADO

APROVADA EM SUA FORMA FINAL PELO PROGRAMA DE PÓS-GRADUAÇÃO

Prof. Dr. Ernesto Vieira Neto
Coordenador

BANCA EXAMINADORA:

Prof. Dr. RAFAEL SFAIR DE OLIVEIRA
Orientador - UNESP

Prof. Dr. ERNESTO VIEIRA NETO
UNESP

Profª. Drª. SILVIA MARIA GIULIATTI WINTER
UNESP

ICP Brasil
Documento assinado digitalmente
FERNANDO VIRGILIO ROIG
Data: 08/03/2024 17:37:07-0300
Verifique em https://validar.iti.gov.br

Prof. Dr. FERNANDO VIRGILIO ROIG
ON

Prof. Dr. NELSON CALLEGARI JÚNIOR
UNESP – RIO CLARO

***MARÇO* de 2024**

CURRICULUM DATA

VICTOR CORREA LATTARI

BIRTH	02/12/1992 - São Paulo / SP
AFFILIATION	Waldir Lucas Lattari
	Luciana Silva Correa Lattari
2012 / 2016	Bachelor of Physics
	São Paulo State University
2017 / 2019	Master in Physics
	São Paulo State University
2019 / 2024	PhD in Physics
	São Paulo State University

I dedicate this thesis to my parents,
Luciana Silva Correa Lattari and Waldir Lucas Lattari.

ACKNOWLEDGEMENTS

I would like to express my gratitude to my parents, Luciana and Waldir, my brother Matheus, my girlfriend Gabriela, and my friends, especially those who have been with me throughout my undergraduate, master's, and doctoral studies: Tiago Francisco, Patricia Buzzatto, Gustavo Madeira, and Luana Liberato. I am thankful to my advisor, Rafael Sfair, who has been with me since the beginning of my undergraduate studies and has consistently provided invaluable guidance and support throughout this journey. I also thank my co-advisor, André Izidoro, who gave me the great opportunity to do the exchange program, without which this experience would have been impossible. I express my gratitude to the members of the doctoral committee, Silvia Maria Giuliatti Winter, Ernesto Vieira Neto, Fernando Virgilio Roig, and Nelson Callegari Junior, for their constructive criticisms, which played a significant role in completing this work. Lastly, I would like to thank CAPES for the financial support, without which the development of this work would have been unfeasible.

This work was supported by the following entities:
CAPES - Coordenação de Aperfeiçoamento de Pessoal de Nível Superior
Process Number: 1684418
This study was financed in part by the Coordenação de Aperfeiçoamento de Pessoal de Nível Superior - Brasil (CAPES) - Finance Code 001
DFG German Research Foundation project 446102036
FAPESP (Processo 2016/24561-0)

“Every Pawn is a potential Queen.“
(James Mason)

LIST OF FIGURES

LIST OF TABLES

CONTENTS

ABSTRACT

In this thesis, we discuss about two main different subjects. In the first part we discuss about Saturn's G-ring arc, while in second part about water delivering to the terrestrial planets during the growth of Jupiter and Saturn. Here starts the part I. Arcs within planetary rings are densely populated regions, believed to form through collisions between interplanetary particles and a satellite embedded within the arc. These collisions can disintegrate material from the satellite, generating dust and smaller bodies. Fragment collisions further contribute to dust production and the formation of larger bodies within the arc. Previous studies have revealed that these arcs primarily consist of micrometer-sized particles. However, these particles face challenges due to perturbative forces, diminishing their lifespan and removing them from the arc. Estimates indicate that dust particles affected by solar radiation pressure would be expelled from the arc within 40 years, posing a challenge to sustaining the dust material. To address this, we propose a refined model of dust generation, considering collisions between macroscopic bodies present in the arc. Through simulations, we demonstrate that disruptive impacts with these bodies contribute significantly to dust deposition within the arc, potentially prolonging its existence. Our findings suggest that these bodies could continually generate dust material, potentially replenishing and sustaining the arc over time. Here starts the part II. Evidence from Earth's water D/H ratio suggests that one of the main sources of Earth's water may have been carbonaceous chondrites' parent bodies. Our simulations simultaneously model the growth and/or migration of Jupiter and Saturn and the accretion of terrestrial planets. We are particularly interested in investigating the influence of the growth and migration of Jupiter and Saturn on the delivery of water-rich planetesimals into the inner solar system. We explored Jupiter and Saturn formed nearly in situ and migrating planetesimals were distributed into two rings. The so-called "inner ring" was assumed to contain water-poor planetesimals distributed from 0.5 to 1.5 AU. The so-called outer ring contained water-rich planetesimals distributed from 5 to 20 AU. Planetary embryos in the inner ring start with their masses between those of the Moon and Mars. Our simulations were integrated using a modified version of the Symba integrator for 100 million years. Our results indicate that the growth and migration of Jupiter and Saturn can deliver about 0.1-1% of water-rich material originally from the outer ring into the terrestrial region, depending on model-assumed parameters. S-type asteroids observed in the belt are traditionally associated with planetesimals from the inner ring. C-type asteroids in the belt are thought to sample planetesimals from the giant planet region. Our simulations where Jupiter and Saturn formed nearly in situ can naturally deliver water to Earth and explain the currently observed fractions between C and S-type asteroids in the belt. On the other hand, the simulations, where Jupiter and Saturn migrated from distant regions, deliver all of Earth's water but tend to implant relatively larger fractions of water-rich planetesimals into the belt than the observed ones, making this scenario potentially inconsistent with the current asteroid belt.

KEYWORDS: planetary ring arcs, Aegaeon, planet formation, water delivery, terrestrial planet formation.

TO THE READER

This thesis is divided into two distinct parts, each one discusses about separate yet interconnected topics. First part focuses on the Saturn's G-ring arc, while the second part explores the delivery of water to the terrestrial planets during the growth of Jupiter and Saturn. The second part of this thesis was developed under supervision of André Izidoro and Rajdeep Dasgupta during my exchange at Rice University. Each part of this thesis can be read independently.

Part I review the dynamics and dust production of Saturn's G-ring arc. These arcs are regions more densely populated than other parts of the ring. They are tenuous and mainly composed of micrometric particles that are highly perturbed by external forces. In this work, we suggest a new mechanism to recompile these micrometric parts in the arc, as their lifetime is too short.

Part II investigates the delivery of water delivery to the terrestrial planets during the formation of the Solar System. In this work, we explored different scenarios for the formation of Jupiter and Saturn. Our results suggest that the growth and/or migration of these giant planets can delivery scatter 0.1-1% of the planetesimals from the H_2O zone ring to the terrestrial planets. Here we also discuss about the proportion of S and C type planetesimals placed in the asteroid belt.

Part I

Dust production in the G-ring arc

1 INTRODUCTION

In early 2004, images from the Cassini spacecraft showed the presence of small satellites Methone, Pallene, Polideuces, Dafne, and Anthe. Two of them, Anthe and Methone, are immersed in two faint arcs confined by the eccentric corotation resonances with the satellite Mimas (10:11 and 14:15, respectively). The material found in these arcs likely represents debris that collided with these satellites at low velocity and became trapped in the same resonance in the same way as the source satellite (HEDMAN et al., 2007).

Figure 1.1 shows the Cassini images that revealed an arc structure at the edge of Saturn's inner G ring. This arc is located around 167500 km from Saturn's center and 250 km wide, which is small compared to the width of the G ring (about 9000 km). The G-ring arc is trapped in the 7:6 eccentric corotational resonance with Mimas. However, unlike the E and F rings, located near the moon that supports the material to them (Enceladus), the G ring is located more than 15,000 km away from known moons closer (HEDMAN et al., 2007).

Figure 1.1 – G ring arc images obtained in September 19th, 1994 at 12:37, 13:11, 13:44 e 14:18 UT. In this image, it is possible to follow the arc's movement.

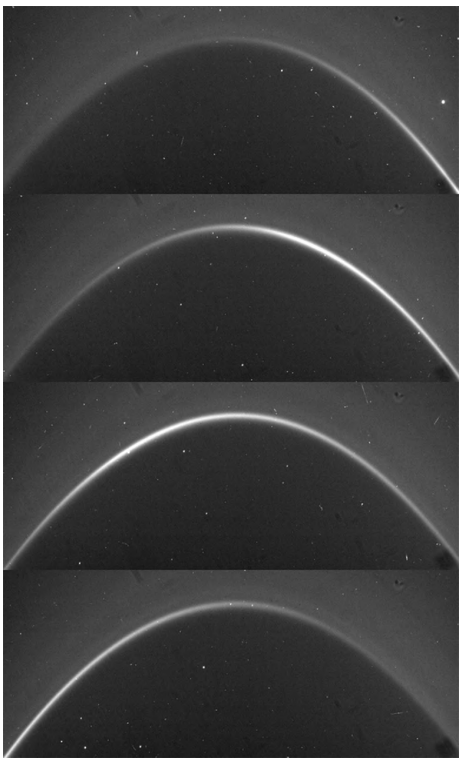

source: Hedman et al. (2007).

Figure 1.2 illustrates the images of the G-ring arc, acquired at low phase angles and high resolution, that detected the presence of a small satellite. This object was announced in an IAU (International Astronomical Union) circular and named "Saturn LIII/Aegaeon"(PORCO, 2009). Hedman et al. (2010) suggested that this small satellite has an irregular shape and a smooth surface due to the constant bombardment of dust grains. To determine its size, they used the same albedo as used for the satellite

Pallene, giving a value of 240 m for a radius and a mass of about 3×10^{10} kg (assuming a density of 0.5 g/cm^3).

Figure 1.2 – Two images obtained in August 15th, 2008 showing the presence of a small satellite near the center of the arc.

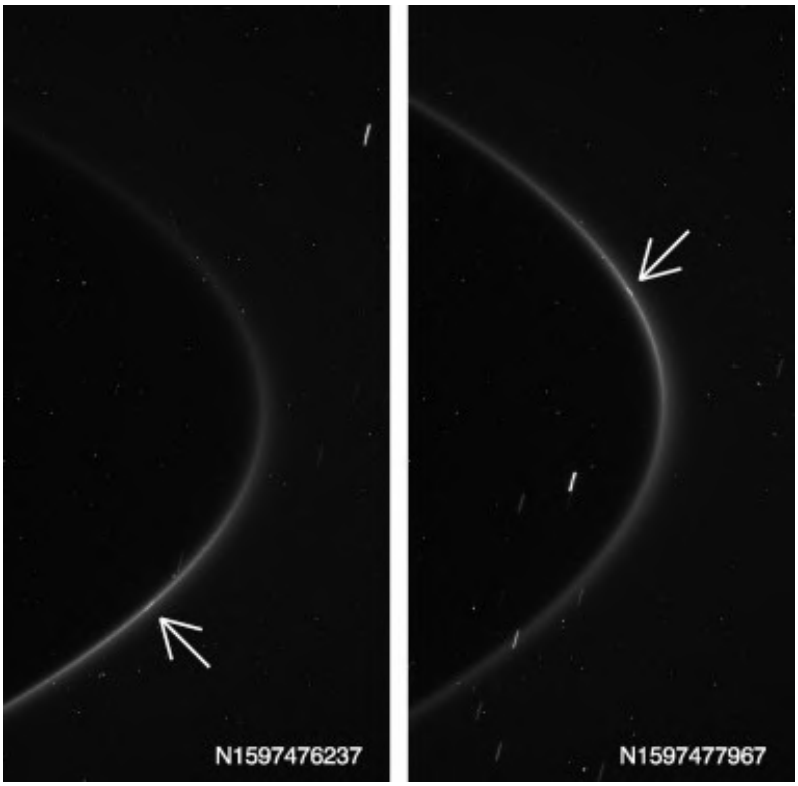

source: Hedman et al. (2010).

Hedman et al. (2010) calculated and analyzed the geometric orbital elements of the satellite Aegaeon (Tab. 1.1).

Table 1.1 – Geometric elements of the satellite Aegaeon

Elements	Mean value
a (km)	167494±4
e	0.0002±0.0002
i (°)	0.0010±0.0009

source: Hedman et al. (2010).

Hedman et al. (2010) also observed perturbations in the semi-major axis and coupling variations in the eccentricity and inclination of the small satellites. These perturbations indicate an influence of other resonances in the Aegaeon's orbit. Figure 1.3 shows that the Aegaeon's orbit is trapped in the 7:6 eccentric corotation resonance (CER) but also perturbed by the 7:6 Lindblad resonance (ILR) with the Mimas satellite. Callegari Jr and Rodríguez (2023) studied the full equations of motion of clones of Aegaeon and showed that its orbit has an important forced component in eccentricity due to the 7:6 resonance. As a consequence, Callegari Jr and Rodríguez (2023) showed that the transitions between circulation and oscillation of the Lindblad angle (see Fig. 1.3) are consequences of a forced component in eccentricity in the orbit of Aegaeon due to resonance.

Figure 1.3 – (a) Resonant angle CER 7:6 ($\varphi = 7\lambda_{Mimas} - 6\lambda_{Aegaeon} - \varpi_{Mimas}$). (b) The Fourier spectrum of the resonant angle shows that the dominant period is 1260 days with an amplitude of 10°. (c) Resonant angle ILR 7:6 ($\varphi = 7\lambda_{Mimas} - 6\lambda_{Aegaeon} - \varpi_{Aegaeon}$). (d) The Fourier spectrum of the resonant angle shows that the dominant period is 820 days with an amplitude of 35°.

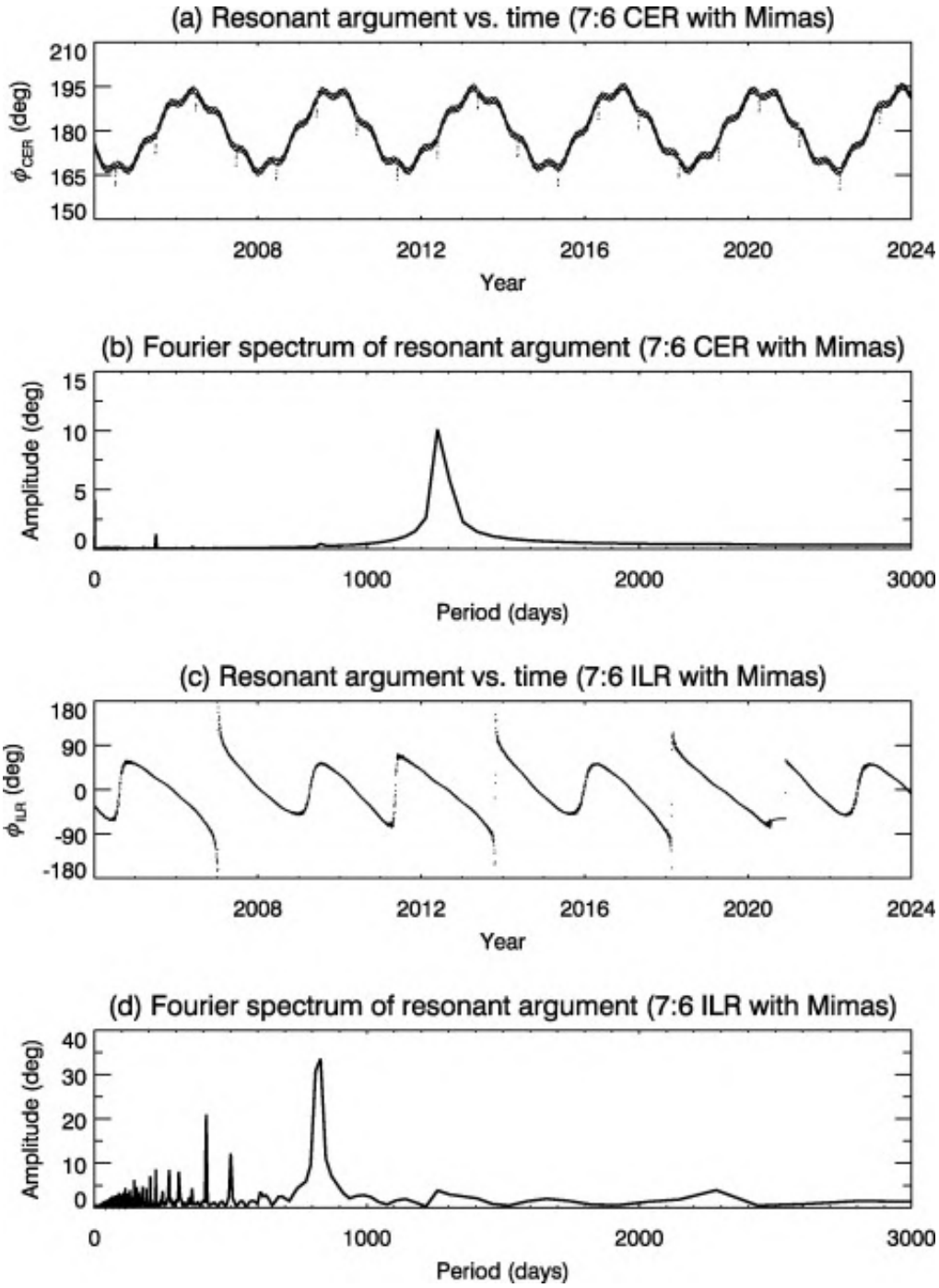

source: Hedman et al. (2010).

The G-ring arc consists mainly of micron-sized particles. However, these particles are strongly affected by external forces such as solar radiation pressure, electromagnetic force, and plasma radiation. Therefore, these forces tend to shorten the lifetime of these particles (HEDMAN et al., 2010). To evaluate one of these perturbations, Madeira et al. (2018) explored the effect of solar radiation pressure, which mainly increases their eccentricity. As a result, they observed that the time to decrease the mass amount in 90% of the arc is 26 years for a particle with a radius of 10 μm, and only three years for 1 μm.

This result raises the hypothesis that there must be a resupply mechanism to keep the particles inside the arc. So, Madeira et al. (2018) also estimated the mass production rate produced by the collisions between interplanetary particles and the satellite Aegaeon. Therefore, they observed that these collisions with the satellite Aegaeon would take more than 30 thousand years to produce the amount of dust present in the arc. However, this production rate to resupply the material corresponds to 3 orders of magnitude of the time required for the solar radiation pressure to remove the particles in the arc. Therefore, this result leads to the conclusion that another dust production mechanism is needed to resupply the particles in the arc.

A possible alternative arises from the difference between the equivalent normal area, described by the Eq. 1.1, of the G-ring arc and its satellite. This parameter defines the area that an ideal material would have to reflect the same amount of brightness of the ring.

$$A = r_0 \int W d\lambda, \tag{1.1}$$

where, r_0 is the mean radius of the ring, λ is the mean longitude and W is the brightness of the ring.

From Eq. 1.1, Hedman et al. (2010) calculated the equivalent normal areas of the arcs of Aegaeon, Anthe, and Methone obtaining 50, 1.0 and 0.3 km^2, respectively. This result shows that the G-ring arc is two orders of magnitude brighter than the other arcs. However, this difference becomes more evident when comparing the equivalent area of the arcs with those of their corresponding satellites. The satellite Aegaeon has 0.07 km^2, while Anthe 0.84 km^2 and Methone 2.21 km^2. These parameters show that the satellites Anthe and Methone have a normal area predominant in their arcs. However, the G ring arc is at least 500 times brighter than its satellite. In other words, the brightness of the arcs of the satellites Anthe and Methone comes from their satellites, while in the G ring arc, it does not come from Aegaeon but from the other objects immersed in the arc.

This disparity between the normal equivalent area of the G ring arc and its satellite creates a possibility that Aegaeon could share its arc with numerous other macroscopic bodies. According to the resolution of the Cassini's cameras, these objects must have radii from 1 to 100 m (HEDMAN et al., 2010). Hedman et al. (2010) mentioned that if these objects were greater than 100 m in radius, they would be detected by the Cassini's cameras. Therefore, the possibility of Aegaeon sharing its arc with other macroscopic bodies raised the hypothesis that these objects may be the mechanism of dust resupply due to collisions between them and interplanetary particles.

Assuming an ice composition (density of 0.92 g/cm3), the total mass of these objects can be estimated from Cassini's instrument LEMMS (Magnetospheric Imaging Instrument's Low Energy), which measures the flux of electrons in the rings. Looking at the G ring arc, this equipment measured drops in the electron flux between 1 and 10 MeV. This reduction indicates that the total mass of the other bodies present in the arc can be in the order of 10^8 to 10^{10} kg. However, the total amount of dust is at a maximum of 10^6 kg. It suggests that the arc may have more objects than only the satellite Aegaeon to explain the drop in the electron flux (HEDMAN et al., 2007). Furthermore, as this drop happened in a small region (around only 250 km), the total mass can not be concentrated in only one satellite and should be spread over numerous objects (HEDMAN et al., 2007).

The presence of these other bodies in the G-ring arc and only one larger body (Aegaeon) suggests that the formation of this system may have occurred as a result of a catastrophic collision in which the Aegaeon satellite would be the most considerable remaining body (HEDMAN et al., 2010). From another point of view, Araujo, Neto and Foryta (2016) proposed another theory for G-ring arc formation. In this case, Mimas captured Aegaeon from the A-ring when it was migrating outwards. After the migration, the satellite became trapped in the 7:6 resonance and generated the arc. However, the results from Madeira et al. (2018) suggest that the migration theory is unlikely to occur due to the short lifetime of the ring particles. Besides this, the presence of only a single arc in the ring and the possibility of existing a large number of meter-sized fragments support that the arc may be created by a larger destroyed satellite.

On the other hand, Hedman et al. (2010) mention that these macroscopic bodies can influence the dynamics colliding with Aegaeon. Collisions in dense arcs and confined by corotation resonances tend to increase the amplitude of the liberation of the particles and make their escape from resonance (dissipating energy)(PORCO, 1991; NAMOUNI; PORCO, 2002). However, because the arc has only one large body moving in a sea of smaller bodies, the collisions would mainly cause a decrease in the Aegaeon (HEDMAN et al., 2010)'s eccentricity and inclination.

In this work, we will study the theory proposed by (HEDMAN et al., 2010) and investigate the influence of these macroscopic bodies on the dust production for the arc. We will will use the combination of N-body simulations and SPH (Smoothed Particle Hydrodynamics) simulations to investigate the possibility of these bodies contribute to the dust production for the arc. In this work, we analyzed both the possibilities, collisions between two macroscopic bodies and impacts of these bodies on Aegaeon.

Following this hypothesis, we found out that the impacts of these bodies on Aegaeon can be the source for dust production to the arc, while the collisions between them are not efficient producing dust material. Finally, we evaluated the amount of dust material in the arc as a function of the time, interpolating the dust produced by the impacts of these bodies on Aegaeon with the life decay for the particles in the arc estimated by (MADEIRA et al., 2018).

The first part of this thesis is followed as

- In Chapter 2, we summarize the results from the N-body simulations,

- In Chapter 3, we summarize the SPH simulations and estimate the dust evolution of the arc,
- In Chapter 4, we finalize with Final Considerations and Future Steps.
- Finally, we present the paper submitted to the special issue of Philosophical Transactions A, associated with the Colloquium honoring Prof. Bruno Sicardy in Paris Appendix A.

2 SIMULATIONS

In this Chapter, we will present the method used to determine the initial conditions for the simulations of the bodies immersed in the G ring's arc. Here, all the orbital elements (a, e, I, Ω, ϖ, and λ) cited will be referred to as the geometric elements that we used to carry out the numerical simulations.

2.1 DETERMINING THE G-RING ARC

Firstly, we will introduce the method to create the G ring's arc trapped in the 7:6 eccentric corotational resonance with Mimas. The orbital elements of the Aegaeon and Mimas satellites were obtained from the Horizons system from NASA (*National Aeronautics and Space Administration*) on 08/22/2008 UT 00:00:00 and are shown in Table 2.1.

Table 2.1 – Orbital elements of Aegaeon and Mimas.

Orbital Elements	Aegaeon	Mimas
a ($\times 10^5$ km)	1.6803398728	1.8600466879
e ($\times 10^{-2}$)	0.3133178063	1.7245224226
I (°)	0.0017328550	1.5641747812
ϖ (°)	142.49114788	163.18023984
Ω (°)	236.30175623	259.15258436
M (°)	5.3481201068	197.73278953

source: (MADEIRA et al., 2018)

In sequence, the orbital elements from Table 2.1 were converted into geometric orbital elements. Then, we adjusted the semi-major axis to reproduce the resonant angles shown in Hedman et al. (2010). This condition was accomplished when $a = 167493.5484$ km, this position corresponds to 0.907451 of the Mimas geometric semi-major axis.

We performed the numerical simulations using the REBOUND package (REIN; SPIEGEL, 2015) with the IAS15 integrator. This integrator has a variable step, and its precision has an order of 10^{-15}. We normalized the gravitational constant using the semi-major axis of 185520 km, the time in days, and the mass is normalized by Saturn's mass (Tab. 2.2). In this case, the gravitational constant corresponds to 44.334508068 $[d^{3/2}][t^{-1}][M^{-1/2}]$ (d unit of distance, t of time and M of mass).

Table 2.2 – Saturn's physical parameters.

Mass (kg)	5.683×10^{26}
Equatorial radius (km)	60268
J_2	0.016290543820
J_4	-0.000936700366
J_6	0.000086623065

source: Hedman et al. (2010)

Figures 2.1 and 2.2 show the evolution of the resonant angles 7:6 CER ($\varphi_{cr} = 7\lambda_M - 6\lambda_A - \varpi_M$) and 7:6 CLB ($\varphi_{Lb} = 7\lambda_M - 6\lambda_A + \varpi_M$). The amplitudes and the periods are consistent with angles proposed by Hedman et al. (2010). The resonant angle φ_{cr} has an amplitude of $\sim 15°$ around $180°$ with a period of ~ 3.4 years, while the resonant angle φ_{Lb} circulates $0°$.

Figure 2.1 – Evolution of the resonant angle φ_{cr} in function of the time.

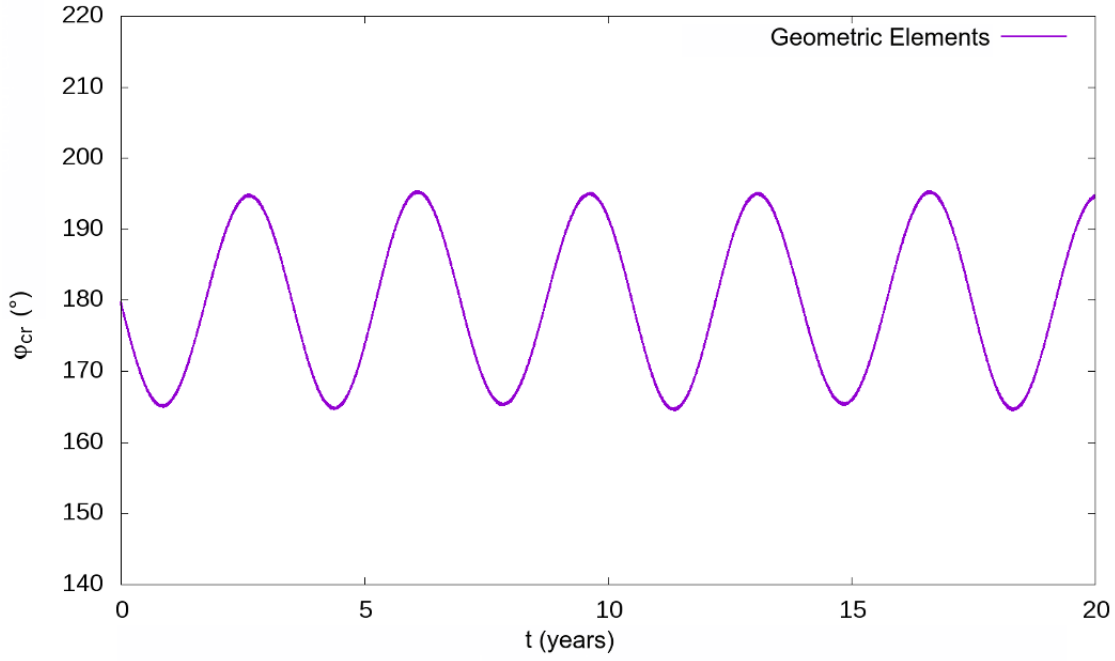

Figure 2.2 – Evolution of the resonant angle φ_{Lb} in function of the time.

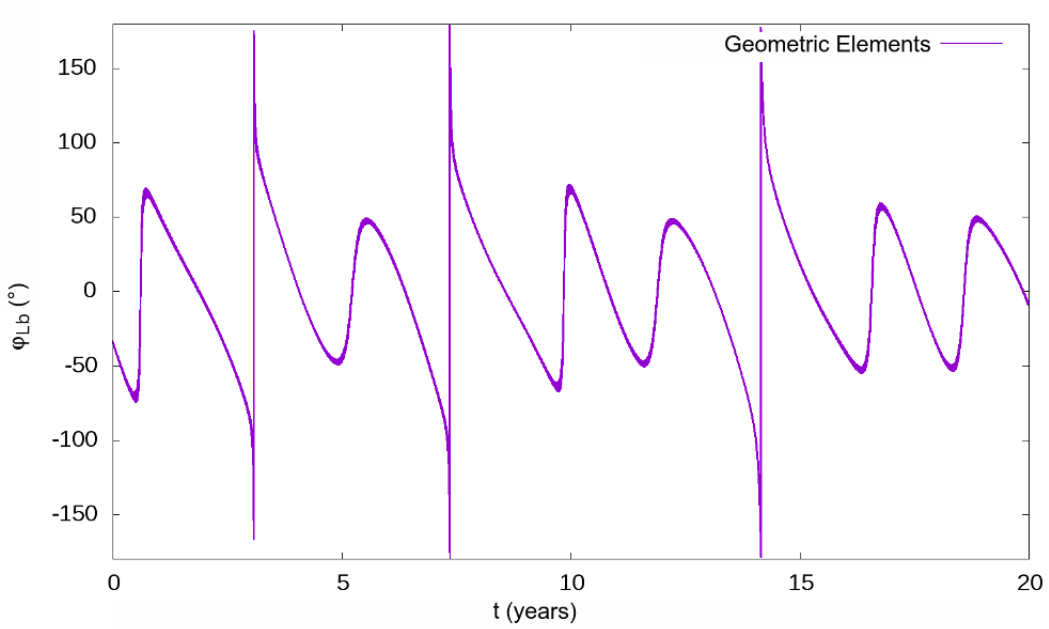

Figure 2.3 illustrates the evolution of geometric orbital elements of the Aegaeon's satellite. The semi-major axis changes by ~ 17 km, while the eccentricity and inclination have few variations.

Figure 2.3 – Evolution of the Aegaeon's geometric elements a, e and I in function of the time.

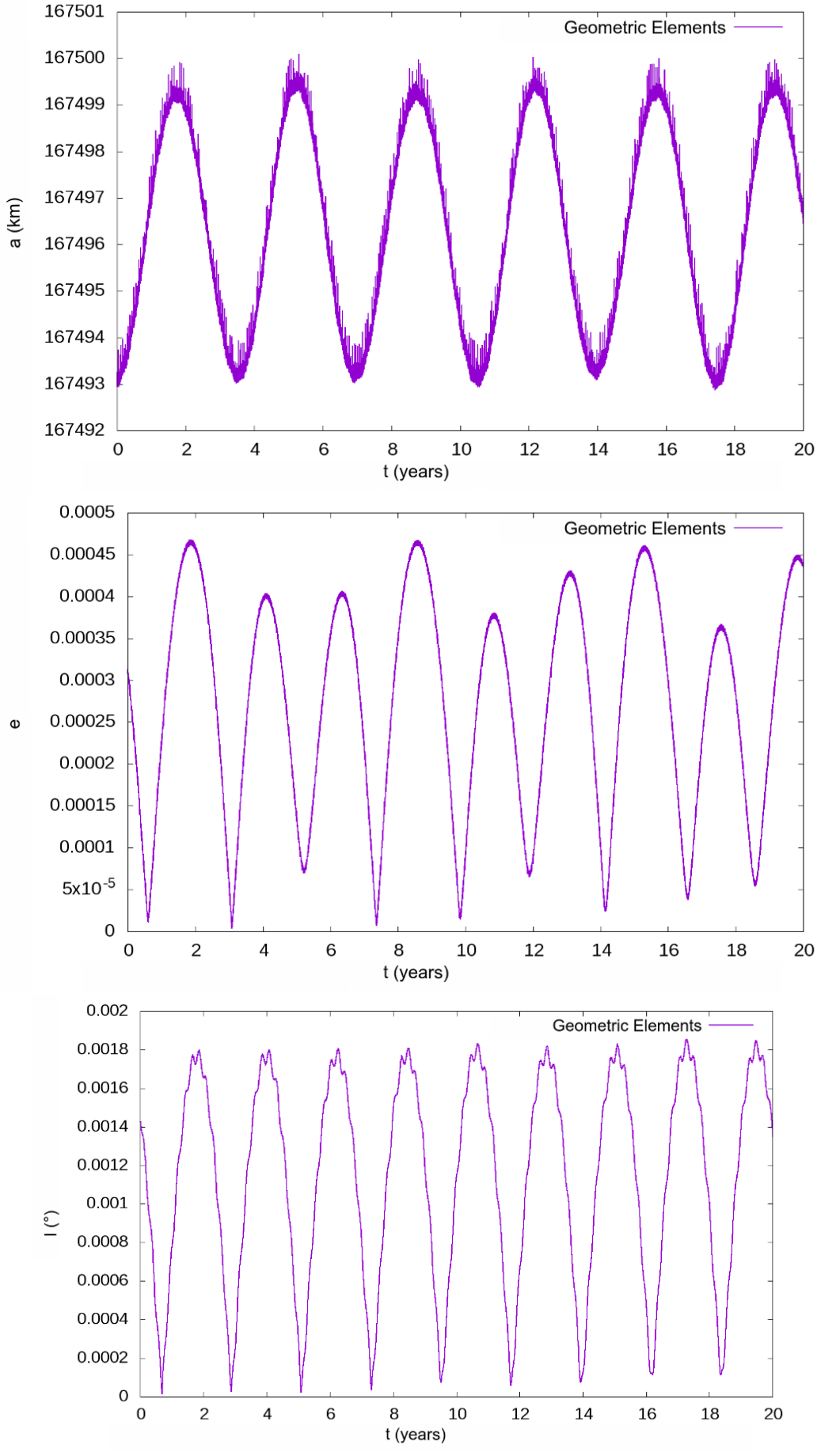

To determine the position of the resonant sites of the 7:6 eccentric corotation resonance with Mimas, we initially distributed 10000 particles between 167450 and 167535 km in semi-major axis and 0 to 360 ° in mean longitude. The particles were distributed randomly in this range using the function *randon_uniform*. This function returns a random variable uniformly distributed within a previously defined interval.

We then numerically integrated these bodies over 20 years. This period is sufficient to determine if the bodies are trapped in the corotation resonance since φ_{Cr} is ~ 3.4 years. In sequence, we divided the bodies into resonants and non-resonants depending on the resonant angle φ_{Cr}. We impose that for the bodies being trapped, the angle must librate, and its amplitude must be at a maximum of $160°$ to avoid bodies that would be intercalating between the resonant sites. Figure 2.4 illustrates the six resonance sites and the corotation resonance, Lindblad resonance, and the position of Aegaeon.

Figure 2.4 – Location of the G ring resonant sites (purple), the corotation (solid line), and Lindblad (dashed line) resonances. Aegaeon is highlighted in orange. The green dots represent the bodies outside the resonance.

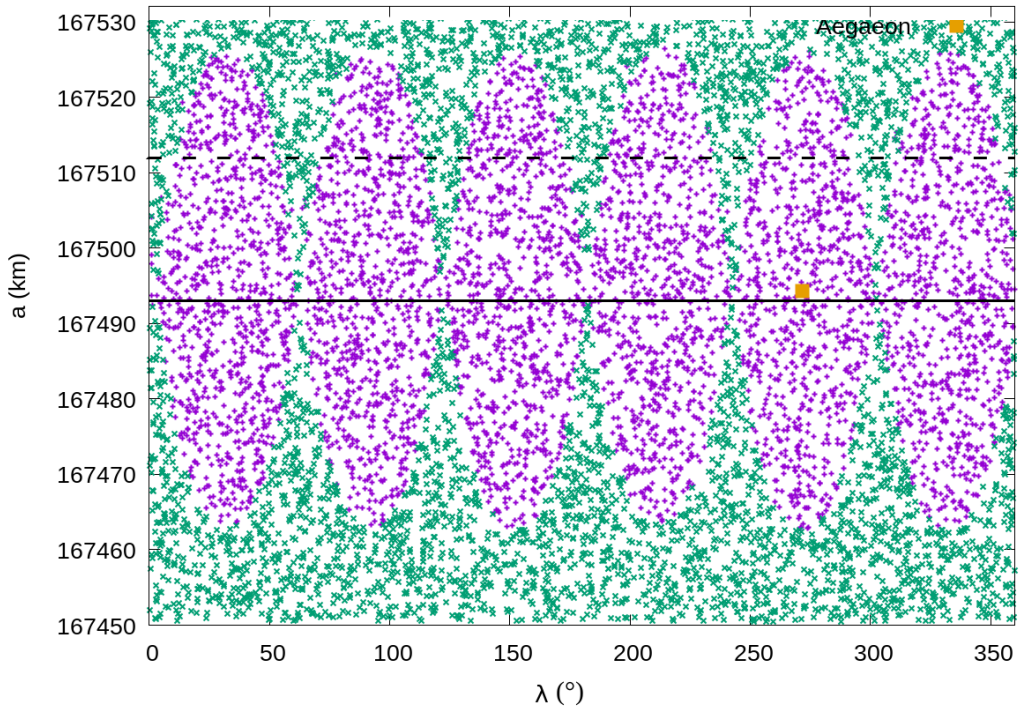

After the simulation, we obtained that $\sim 65\%$ of the initial bodies were trapped in the corotation resonance. There are six resonant sites with a radial width of 63 km (see Lattari (2019)). Figure 2.5 shows a zoom-in of the G-ring arc. The satellite is highlighted in yellow, while the other bodies are presented in purple. This final distribution was used for the numerical simulations we will introduce in sequence.

2.2 OUTCOME OF THE COLLISIONS IN THE G-RING ARC

To analyze the production of dust generated by super-catastrophic collisions between the macroscopic bodies present in the G ring arc, we carried out four numerical simulations with 20 m because it

Figure 2.5 – Initial distribution of bodies in the resonant site of the satellite Aegaeon (orange).

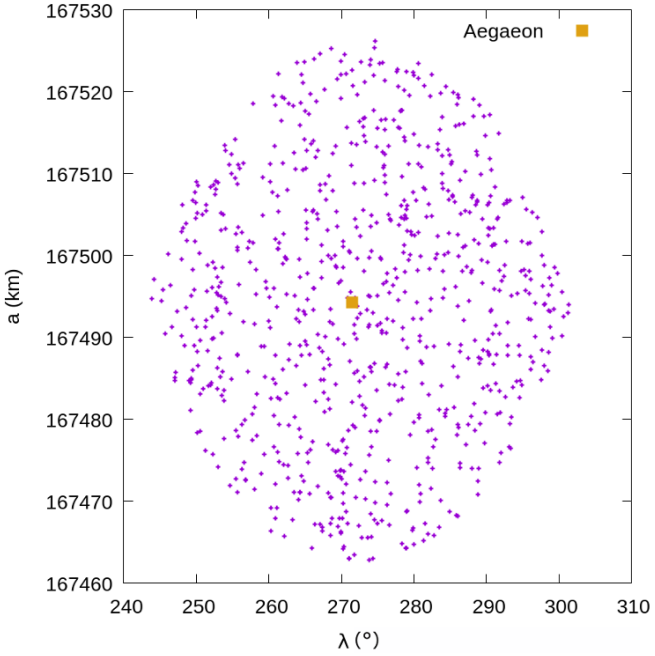

is hard to estimate the radius of these bodies. We chose to simulate the bodies as being porous with $d = 0.5$ g/cm^3 and non-porous with $d = 0.9$ g/cm^3. In addition, we chose to analyze the Aegaeon's effect on the dynamic of the collisions, comparing simulations including on excluding it. The total number of macroscopic bodies was determined using the maximum amount of mass that can be distributed in the arc in the order 10^{10} (HEDMAN et al., 2007). Table 2.3 shows the initial conditions for our four simulations.

Table 2.3 – Initial conditions of the simulations. The symbol d represents the density of macroscopic bodies, and N is the total number of bodies for each simulation. In the last column, the x indicates the presence of Aegaeon in the simulation, while - indicates the simulation without the small satellite.

Simulation	d g/cm^3	N	Aegaeon
1*	0.5	2040	x
2*	0.5	2040	-
3*	0.9	980	x
4*	0.9	980	-

We performed the numerical simulations using the REBOUND package with the IAS15 integrator (REIN; SPIEGEL, 2015). To determine the initial orbital distribution of the macroscopic bodies, we randomly chose initial conditions from the distribution of bodies as shown in Fig. 2.5. The collision condition was defined as a direct collision using the REBOUND function *reb_collision_direct*. After the code detects one impact, it calls the function *outcome_collisions* that we implemented in the code.

This function saves the outcome of every collision that happened in the simulation. Then, it calculates the relative velocity v_i, the impact angle (θ) and saves the state vectors and the time of each

collision. Besides this, we also take care of the indices of each body to be sure that we are not looking at the same collision since the REBOUND package changes the position of each particle after one body is removed from the simulation.

We performed the simulations over a total of 1000 years. We considered Saturn, Mimas, and Aegaeon as active in the simulation, so they affect themselves and the other bodies in the simulation. The macroscopic bodies were considered massless, so they do not affect the other bodies[1]. Table 2.4 summarizes the total number of collisions that happened between the macroscopic bodies and the total number of impacts with Aegaeon, comparing simulations using different densities and when Aegaeon was or was not included in the simulation.

Table 2.4 – Distribution of the collisions.

d (g/cm^3)	Aegaeon's presence	Number of collisions with Aegaeon	Number of Collisions between the bodies
0.5	yes	142	233
0.5	no	-	232
0.9	yes	83	78
0.9	no	-	89

Table 2.4 shows that roughly $\sim 40\%$ of the total number of collisions happened with Aegaeon for the simulation with density equals to 0.5 g/cm^3, while when the density is 0.9 g/cm^3 roughly 50% happened with the small satellite. This table also shows that Aegaeon does not effectively change the number of collisions between the macroscopic bodies. It happens because Aegaeon is located near to the center of the resonance and its orbit in the rotating frame is small. Therefore, it does not affect the orbit of the bodies far way from the center of the resonance.

Figure 2.6 presents a heatmap of the relative velocity as a function of impact angle in collisions between a 20 m radius body and Aegaeon. The left graph depicts simulations with a 0.5 g/cm^3 body density, while the right with 0.9 g/cm^3. We can verify that typical collision velocities are around 5 m/s, ranging from 1 to 15 m/s, with impact angles predominantly between 30 and 50 degrees. No notable variance is observed between simulations with different body densities, as density variations only affect the number of bodies in the simulations.

Figure 2.7 illustrates a heatmap of relative velocity against impact angle for collisions between two 20 m radius bodies. The upper panels represent simulations with d=0.5 g/cm^3 density, and the lower with d=0.9 g/cm^3. The left plots include Aegaeon, while the right exclude it. These results indicate typical relative velocities of approximately 0.5 m/s, with velocities extending up to 10 m/s depending on the location of the bodies. The impact angles are predominantly below 60°, typically around 30°. Notably, Aegaeon's presence significantly influences the distribution of velocities and impact angles. The distribution appears more uniform in simulations excluding Aegaeon, suggesting its significant effect on the velocities of bodies within the arc, particularly during close encounters. Comparing the typical collision velocity of 0.5 m/s between two macroscopic bodies with the 5 m/s impact velocity involving Aegaeon, it is evident that Aegaeon contributes to the acceleration of these bodies upon

[1] These bodies are at least 1800 times less massive than Aegaeon.

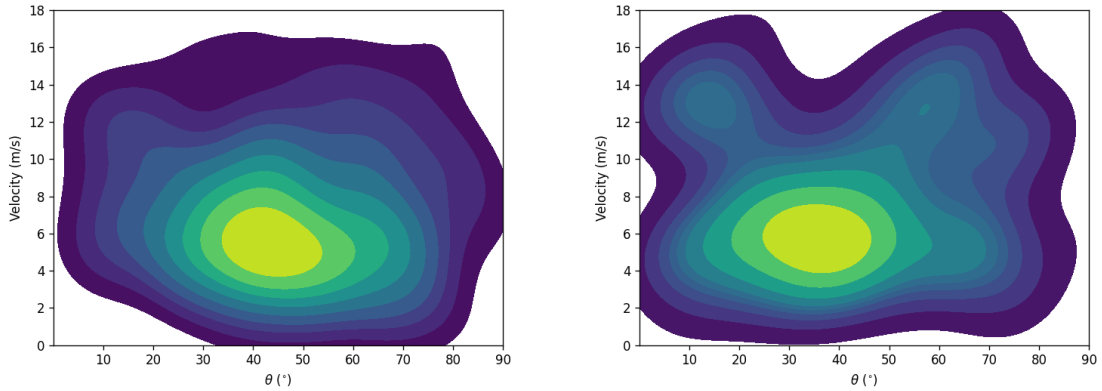

Figure 2.6 – Relative velocities as a function of the impact angle (θ) in collisions between a 20 m radius body and Aegaeon. The left panel depicts the simulation with a density of 0.5 g/cm^3, and the right panel with 0.9 g/cm^3. These graphs demonstrate that the typical relative velocity of these collisions is around 5 m/s, and the impact angle predominantly occurs between 30 and 50 degrees. The yellow color represents the area where more collisions occurred, and the colder the color, the fewer collisions occurred.

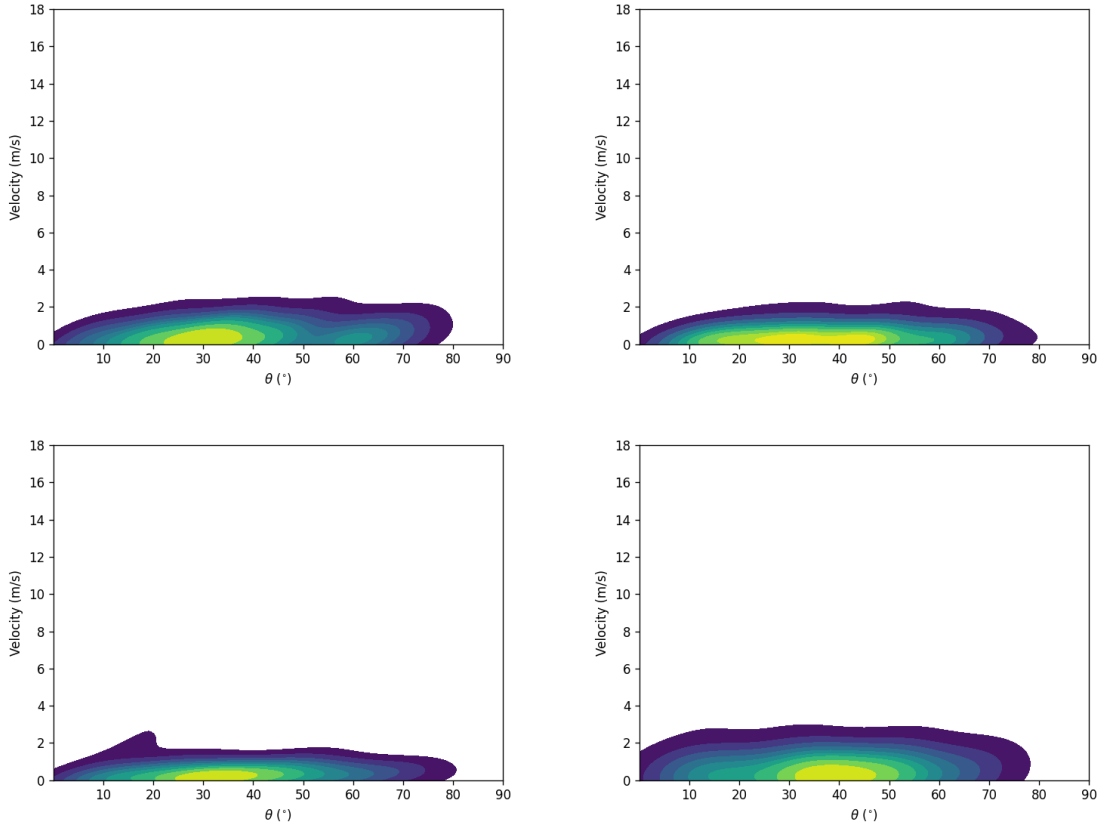

Figure 2.7 – Relative velocities as a function of the impact angle (θ) in collisions between two macroscopic bodies. The upper panel represent simulations using a density of 0.5 g/cm^3, while the bottom uses 0.9 g/cm^3. The left plots include Aegaeon in the simulations, whereas the right ones exclude the satellite. These plots illustrate Aegaeon's influence on the velocity and impact angle distribution in collisions among macroscopic bodies. The yellow color represents the area where more collisions occurred, and the colder the color, the fewer collisions occurred.

proximity. The acceleration caused by Aegaeon to a body approximately 500 m away is on the order of 10^{-4} m/s^2, in contrast to Saturn's acceleration of about 1 m/s^2 in the arc.

The primary objective of this work is to evaluate the impact of these hypothetical macroscopic bodies dust production in the G-ring arc. To this end, we conducted simulations of typical collisions between macroscopic bodies and their impacts with Aegaeon using SPH. This approach aims to evaluate whether these collisional mechanisms contribute to sustaining the dust in the arc, considering that solar radiation pressure removes small particles in less than 40 years. Subsequently, we will present the outcomes of these collisions and estimate the total dust production from each collision type.

3 ESTIMATING THE DUST EVOLUTION IN THE FUNCTION OF THE TIME

Here, we will introduce our method for estimating the dust produced by the collisions between macroscopic bodies and their impacts with Aegaeon in the G-ring arc. Subsequently, we will evaluate the total dust mass in the arc over time. In this section, we will also show that the collision between these two bodies is not efficient to produce dust, while the impact of these bodies with Aegaeon is more energetic and can produce a large amount of dust every impact. Because of that, our model focuses only on the dust resulting from impacts of these hypothetical bodies with Aegaeon and the decay of its lifetime due to solar radiation pressure calculated by Madeira et al. (2018).

3.1 SMOOTHED PARTICLE HYDRODYNAMICS

We present the numerical simulations using the hybrid hydrocode SPH (Smoothed Particle Hydrodynamics) in collaboration with Patricia Buzzatto. Details of the code and methods can be found in Buzzatto, Sfair and Schäfer (in prep.). We used the code miluphcuda developed by Dr. Schäfer and researchers from the Center for Computational Physics at the University of Tübingen. The program is in the public domain and is described in Schäfer et al. (2020). Here, the objective is to simulate the collisions obtained from the N-body simulations described in Sec. 2 with SPH to precisely determine the distribution of the fragments, their masses and velocities, and the dust production.

The main difference between the results obtained from SPH simulations and the traditional N-body simulation is that we can have higher resolutions on the distribution of the fragments and treat the material properties more realistically. We are mainly interested in determining the percentage of the mass that will be transformed into dust. However, we also have to accurately estimate the size and velocity of the fragments to verify if they will be trapped in the resonance and stable in the arc after the collision. To obtain these parameters, we will explore the shock propagation, material modification, and gravitational re-accumulation, and then finally estimate the dust generation rate of each collision.

3.1.1 Numerical simulations

Here, we will present how we incorporated the N-body outputs as inputs into the SPH simulations. The function *outcome_collisions* calculates the relative impact velocity v_i, their masses, and determines the geometry between the projectile and the target. The geometry is composed of the impact angle (θ), the radius r (projectile) and R (target), and the impact parameters B (distance of the closest approach between the two bodies) and l (the width at which the projectile overlaps the target).

However, the state vectors given by the N-body simulations are numerically large to work on the SPH. In this case, we chose to use the centroid of the target and the projectile as the reference frame. At the same time, the bodies were separated at a mutual distance of $d_{ini} = R + r + 2.5_{\text{sml}}$ to avoid numerical errors.

Figure 3.1 – Representation of the geometry of one collision on Rebound and SPH.

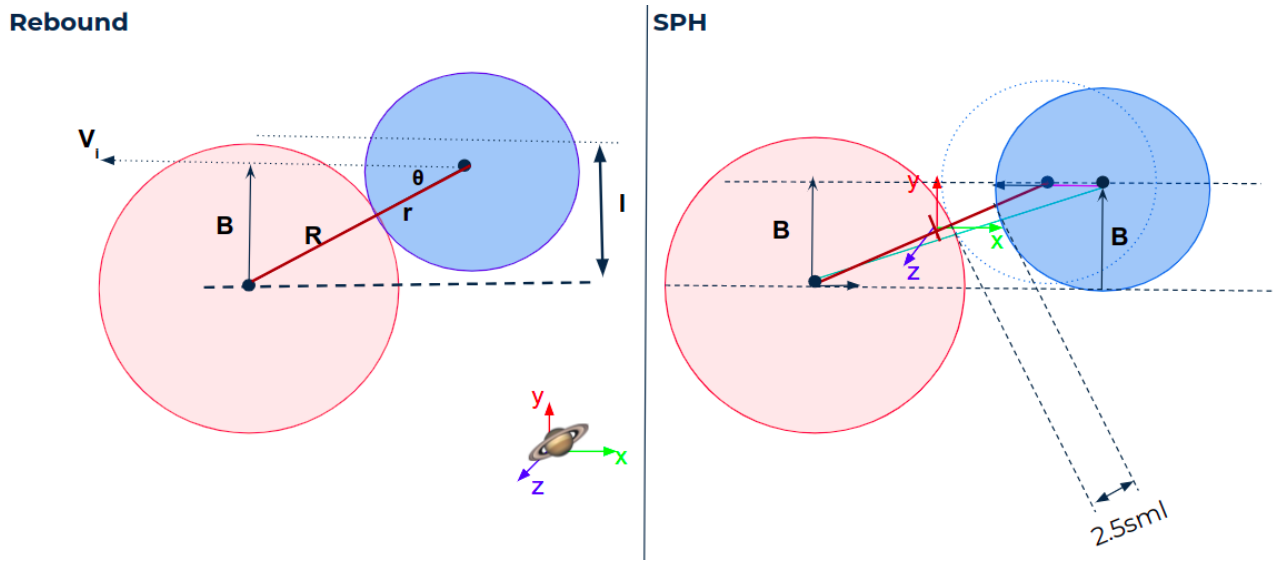

The code uses the parameter sml[1] to distinguish the two bodies at the beginning of the simulation. Figure 3.1 illustrates the geometry of the collision recorded by REBOUND and the geometry used as input into the SPH. The simulations were performed using 150,000 particles per object (target and projectile) to ensure sufficient resolution for different collision scenarios. The running time of the simulation mainly depends on the body size and impact velocity.

We identify the fragments following two main phases based on the code described by Burger, Maindl and Schäfer (2017):

1. Firstly, we identify all clumps[2] of SPH particles that are spatially connected, defining them as "fragments".

2. Then, we determine the gravitationally bound "aggregates"of these fragments. The seed aggregate consists of the most massive reminiscent body and all the mutually gravitationally leftovers bound to it.

The identification of the dust particles is based on the SPH resolution used in the simulation. In our case, it converges to be mostly fragments with less than 0.01% of total mass formed of single fully damaged [3] particles. Therefore, we considered any fragment with a mass lower than this percentage to be dust. Summing up all those cases, we can determine the total amount of dust produced for each collision scenario.

[1] sml means the smoothing length, which is the space used to determine the region of influence of the neighboring particles. The code fits a gaussian distribution and determine which particles are agglutinated forming a single body together.

[2] clumps refer to regions where particles cluster together due to various physical processes. These clumps can arise from gravitational attraction or fluid dynamics effects.

[3] the "damage"parameter measures the degradation or weakening of a material in response to applied forces or stresses. Its value increases as the material experiences more stress, resulting in changes in mechanical properties or even material failure.

Now, we will investigate the possibility of the collisions between two same meter-sized bodies produce dust exploring different relative velocities and sizes for the bodies. We chose to fix the impact angle at 30 ° to reduce the number of simulations using the typical one. Table 3.1 shows the dust production of these collisions for bodies of 1 m, 5 m, 10 m and 20 m in radius and relative velocities of 2 m/s 10 m/s and 20 m/s. Here we aim to explore the possibility of different scenarios as we do not have an accurate information of their sizes, only that they must be smaller than 50 m in radius because of the Cassini's resolution.

Table 3.1 – Dust generation from different collision setups using a fixed impact angle of 30°.

Radius	1 m	5 m	10 m	20 m
Velocity	Dust produced			
2 m/s	0.00%	0.00%	0.00%	0.00%
10 m/s	0.00%	0.14%	0.34%	0.00%
20 m/s	0.01%	0.62%	0.60%	0.59%

Table 3.1 indicates that dust production is affected by both the radius of the bodies and the collision velocity. Notably, there is no dust generation when the velocity is 2 m/s which suggest that there is almost no dust production when we consider a collision between two macroscopic bodies. This result shows that these bodies can not recompose the arc if we consider that the majority of the collision between themselves happens at low velocity around 1 m/s. On the other hand, more energetic collisions can destroy them and generate dust. We must also note that it is more difficult to break smaller bodies, suggesting a possible threshold velocity for dust generation relative to the body size.

Figure 3.2 illustrates the last snapshot of one collision between two 20 meter-sized objects and the distribution of mass fragments as a function of the velocity. In the left panel we can visibly distinguish the fragments and the dust using the damage. The right panel shows the distribution of the projectile leftovers in red, while the target ones in blue. The dashed line represents the limit for one particle being considered dust in our simulations.

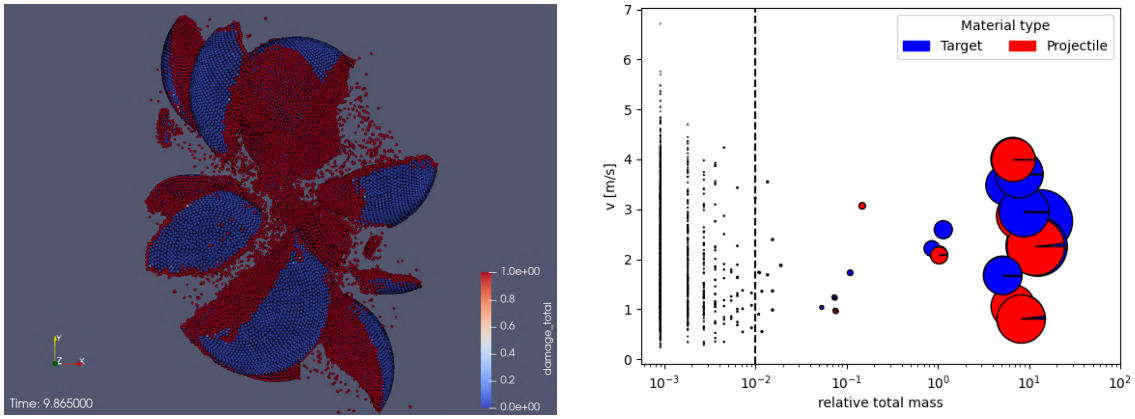

(a) Snapshot showing the damaged particles. The blue color represents the bounded particles, while the red the damaged particles.

(b) Fragments velocity in the function of the relative total mass of the fragments. The dashed line represents the limit where they are considered dust.

Figure 3.2 – Illustration of the fragments and the dust production from a impact at 10 m/s.

Here, we show that it is possible to produce dust through collisions among macroscopic bodies. However, these collisions happens at low velocities in the G-ring arc, leading to no considerable dust production regardless of the bodies' sizes. This result raises the necessity of invoking another mechanism to produce dust in the arc. To investigate alternate dust generation mechanisms, we focused on collisions with Aegaeon, which represents about 40% of total collisions in the arc verified in the N-bodies simulations.

For a simplified model, we adopted a standard collision scenario involving a relative velocity between 5 m/s and 10 m/s and an impact angle of 45°. This setup is comparable with typical collisions observed in our simulations. The projectile was simulated with 10,000 SPH particles, while Aegaeon was modeled using 1,000,000 SPH particles. Due to the resolution and the size of the bodies, only a portion of the satellite was included in the simulation.

Figure 3.3 illustrates the mass fragment distribution and corresponding velocities from an SPH simulation of a collision between a 240 m-sized target (Aegaeon) and a 20 m-sized projectile at 10 m/s, at an angle of $45°$. The results show significant disruption of the projectile, with 76.47% of its mass forming smaller fragments, and the remaining 23.53% becoming dust particles.

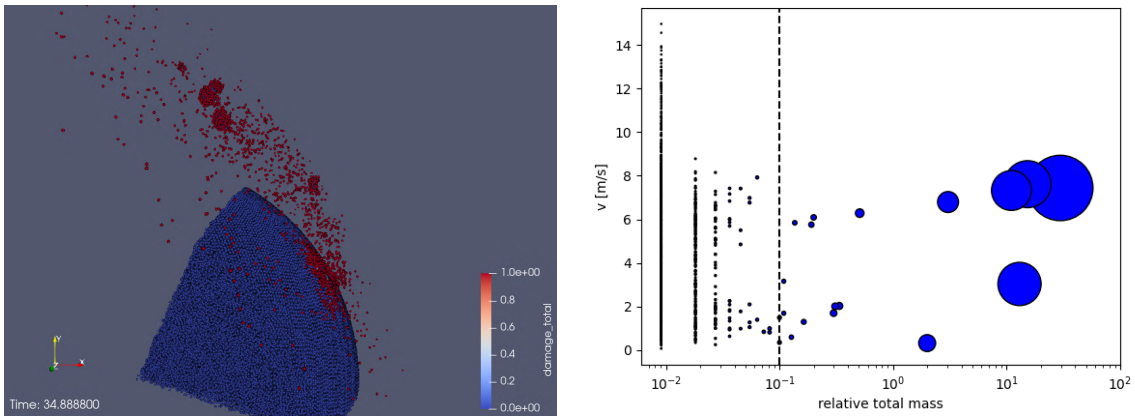

(a) Snapshot showing damaged particles from the projectile impacting Aegaeon.

(b) Velocity and mass distribution of fragments post-collision.

Figure 3.3 – Fragments and dust from a 10 m/s impact velocity.

Table 3.2 summarizes the dust production resulting from different collision scenarios between a projectile and Aegaeon. This table considers different projectile velocities and impact angles. From the table, it is evident that dust production varies significantly with changes in the projectile's velocity and impact angle. In typical collisions with Aegaeon, moderate velocities and impact angles tend to result in an average dust production of around 10%.

Table 3.2 – Dust production from a collision between a projectile with Aegaeon.

	Velocity	Dust produced	
Projectile:		r =10 m $\theta = 30°$	r = 20 m $\theta = 45°$
	5 m/s	9.38%	6.63%
	10 m/s	17.37%	23.53%

Table 3.2 suggests that the impact of these hypothetical macroscopic bodies with Aegaeon could generate enough dust material to recompose the arc. In the next section we will explore this hypothesis interpolating the dust production every time one impact happens with Aegaeon with the solar pressure radiation decay to investigate if there is any scenario where we can have a balance between the removal and dust production in the G-ring arc.

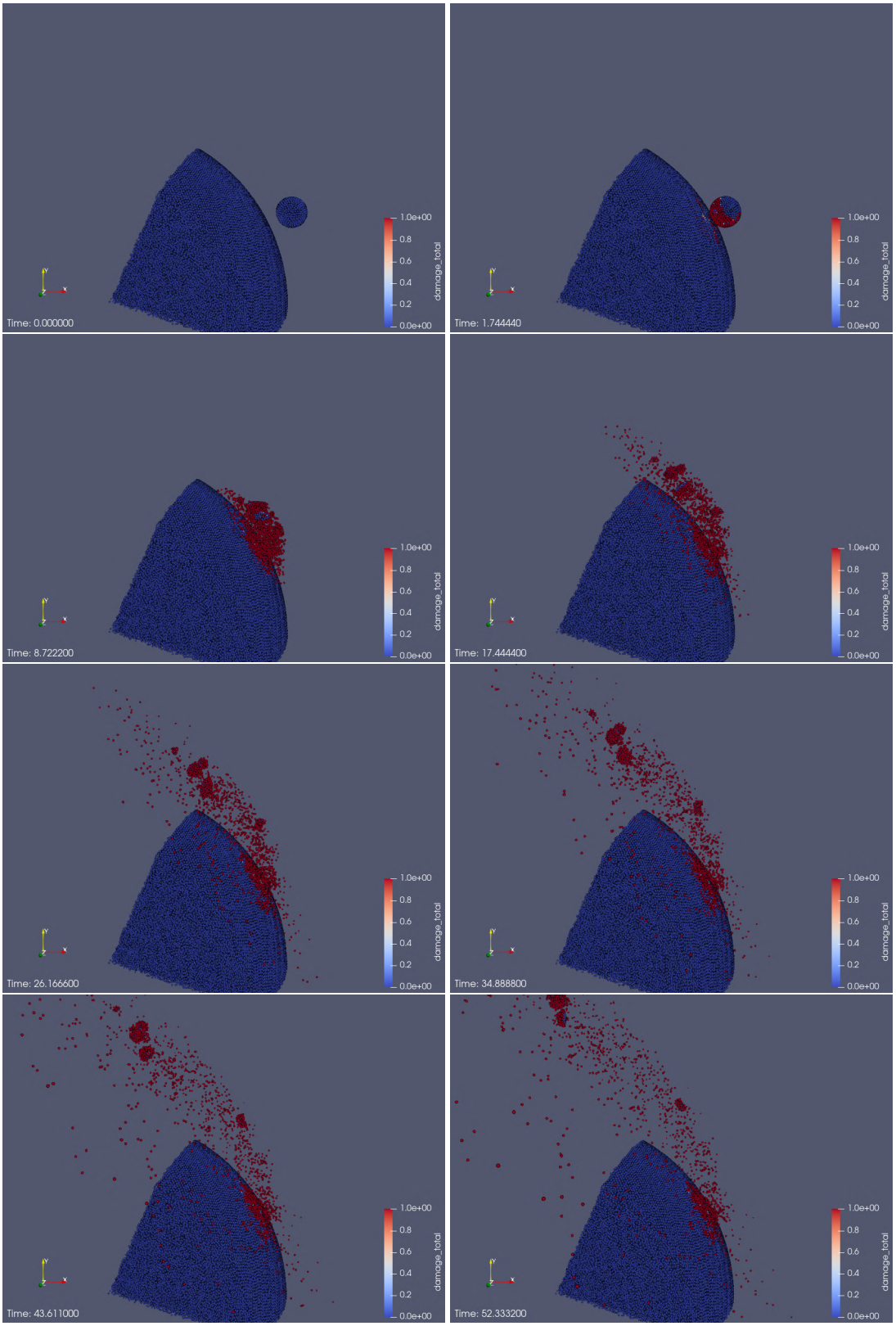

Figure 3.4 – Snapshots of Aegeon impacted by a 20 m-sized projectile at 10 m/s and an angle of $45°$.

3.2 DUST EVOLUTION PRODUCTION OVER TIME

Here, we will combine the results obtained by the N-body simulation and the SPH simulation. We start presenting the collision rate of the macroscopic bodies on Aegaeon. In sequence, we evaluate the total amount of dust in the function of time considering the dust production through impacts of the macroscopic bodies on Aegaeon and the life decay produced by the solar radiation pressure.

3.2.1 Distribution of the impact collisions with Aegaeon as a function of the time

In the last section, we show that the impacts of hypothetical macroscopic bodies with Aegaeon is an efficient mechanism to produce dust and can sufficiently resupply the dust material in the arc. Therefore, we must analyze the collision ratio of these impacts and determine if it is comparable to the ratio that the solar radiation pressure removes the particles from the arc. In this model, we neglect the dust generation from collisions among macroscopic bodies, as we assume they do not sufficiently generate material for resupplying the dust in the arc.

Figure 3.5 illustrates the cumulative number of impacts of macroscopic bodies on Aegaeon over time, based on N-body simulations. The full-dashed line represents simulations using bodies with a density of 0.5 g/cm^3, and the dashed line for those with 0.9 g/cm^3. In the simulation with porous bodies, there were a total of 142 impacts, while in the non-porous simulation, there were 83 impacts over 1000 years.

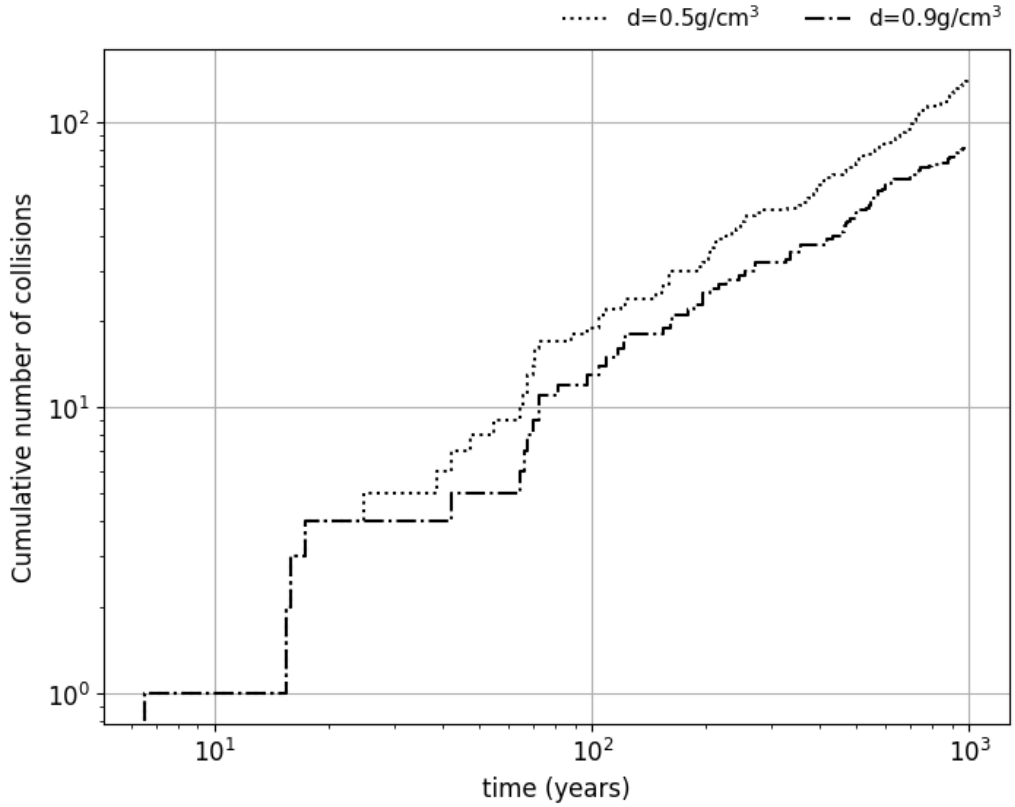

Figure 3.5 – Cumulative number of collisions with the satellite Aegaeon for bodies with densities of 0.5 g/cm^3 and 0.9 g/cm^3.

From this data, we can roughly estimate an impact frequency with Aegaeon at about one collision every 8 years for porous bodies and one every 13 years for non-porous bodies, based on a simple linear fit. This period is comparable to the time for the solar pressure force to remove the micrometric particles from the arc (MADEIRA et al., 2018). However, this ratio is only applicable over a short period, as the bodies gradually disintegrate over time. Additionally, the cumulative effect of producing fragments in each collision, which may subsequently collide with Aegaeon, generating more dust, is not considered in this calculation.

Assuming that only one impact is sufficient to resupply the arc, we can keep the dust material in the arc for entire simulation. Our SPH simulations suggest that every impact would transform at least 10% of projectile mass into dust, which suggest that even an impact of a 5 m body would produce enough dust to recompose the arc. Finally, if we assume that the arc of the G ring was formed due to a super catastrophic collision, and Aegaeon was the largest reminiscent body formed, the arc should be maintained by these impacts with Aegaeon.

Our results suggest that the existence of the arc can be related to the impacts of these macroscopic bodies with Aegaeon. This hypothesis is coherent with the fact of the existence of only one arc in the G-ring because only one satellite would not be sufficient to recompose the particles in the arc. Finally, this system will destroy itself in the function of time and could be in its final phase because there is a little amount of mass distributed in the macroscopic bodies. In sequence, we will evaluate the dust evolution over time interpolating the results from N-body and SPH simulations.

3.2.2 Evaluating the amount of dust in the function of the time

In this section, we will estimate the amount of mass-produced by the impacts of macroscopic bodies on Aegaeon. The dust generated by the collisions between the macroscopic bodies was not accounted because the dust production is not effective. For the impacts on Aegaeon, we use the results obtained from the SPH simulations (see Sec. 3.1). We use a conservative production that about 10% of the projectile mass is converted into dust, this efficiency depends on the collision setup.

To estimate the amount of dust immersed in the arc and explore if exists any scenario where we can have a stable amount of dust, we fitted an exponential decay for the particles according to the lifetime of the micrometric particles (see Tab. 4 in (MADEIRA et al., 2018)). We explored the same parameters distributed into four sizes: 1μ, 3μ, 5μ 10μ, and velocities equal to 1, 5, and 10 of the escape velocity. By combining the natural decay of dust particles with the new dust generated from collisions with Aegaeon, we can evaluate the dust population within the arc. Figure 3.6 shows the moving averaged amount of dust (normalized by the amount of dust proposed by (HEDMAN et al., 2010) $\approx 10^6$ kg) in the function of the time for each scenario at $v = 5v_{esc}$.

Our results show that it is possible to maintain the dust population in the arc for at least 1000 years if we consider the collision between the macroscopic bodies with satellite Aegaeon. However, it is hard to maintain the 1 μm particles in the arc because their life is too short. Therefore, we propose that collisions between macroscopic bodies and Aegaeon could be a source of dust material for the

arc, resulting from their fragmentation and dust generation. So, if there is a big population of these macroscopic bodies in the arc, they can recompose the dust material as they destroy themselves.

The hypothesis that the dust particles of the arc being supported by the impact of these macroscopic bodies with Aegaeon becomes more compelling when considering an underestimation of collision frequency with Aegaeon, as we only accounted for 20 m radius bodies. A more realistic scenario with bodies ranging from 1 to 50 m in radius could significantly increase collision rates and dust production. It is hard to estimate the total number of objects and how these bodies are distributed in radius, but the more bodies we have, the more the arc can survive. However, we believe that this system is temporary and can survive until the macroscopic bodies finish breaking up.

This scenario supports the theory that the G-ring arc may have originated from a super-catastrophic collision, fragmenting a larger body into Aegaeon (the largest fragment) and numerous smaller fragments, which continue to generate dust in the arc. Additionally, we might consider the possibility of a 'firefly' behaviour characterized by fluctuating brightness. In a situation with few bodies in the arc, the frequency of impacts with Aegaeon would reduce significantly, leading to brief periods of intensified brightness following each collision. This hypothesis highlights the dynamic nature of the arc's brightness based on the population and activity of macroscopic bodies within it.

We also analysed the evolution of the Aegaeon's mass through collisions with the macroscopic bodies immersed in the arc. Aegaeon survived every impact and did not suffered any catastrophic collision when we simulated the collisions using SPH. These results show that the macroscopic bodies that may exist in the arc will not strongly affect the Aegaeon's mass and can coexist with the satellite without any major change in its orbit or mass which is expected since the bodies are at least three orders of magnitude less massive than Aegaeon.

For completeness, we also simulated the arc with bodies of 50 and 100 meters in size, totaling 2000 bodies. We assumed that all collisions would perfectly merge to try to create a second body with mass comparable to Aegaeon. In these simulations, we observed that when Aegaeon was included, it increased in size and effectively "blocked"the growth of other bodies, becoming the only large satellite in the arc. Conversely, when we initiated the simulation without Aegaeon, one body rapidly grew and similarly "blocked"the growth of others by increasing its mass. These simulations suggest that it is unlikely for more than one satellite to exist in the arc.

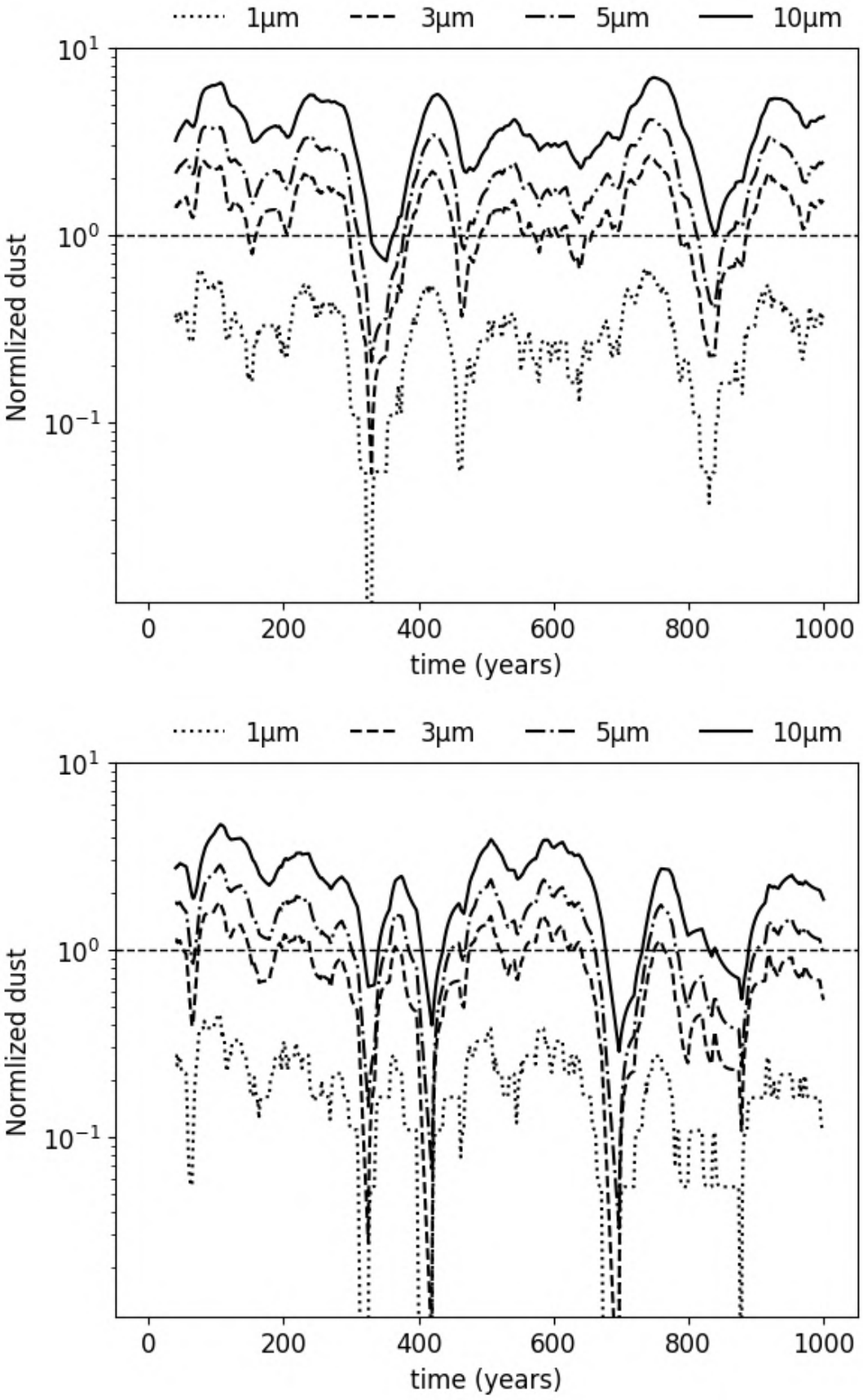

Figure 3.6 – Normalized dust quantity (by the current dust amount in the arc) over time. The plots represent dust produced by collisions between 20 m radius bodies and Aegaeon, interpolated with decay due to solar pressure radiation for particles of 1μm, 3μm, 5μm, and 10μm. The upper panel is for collisions with 0.5 g/cm^3 density bodies, and the bottom for 0.9 g/cm^3. The dashed line represents the current dust amount in the arc, approximately 10^6 kg.

4 FINAL CONSIDERATIONS AND FUTURE STEPS

The G-ring arc is composed mainly of micrometric particles. External forces extremely influence these particles. The solar radiation pressure removes the micrometric particles from the G ring arc in less than 40 years. However, its moonlet cannot replenish these particles by impacts of interplanetary particles, which needs at least 3000 years to generate the current amount of dust in the arc. Then, we must invoke another mechanism to recompose the dust in the arc. Otherwise, these particles would be lost in a few years.

Another mechanism can be invoked from the macroscopic body population that may exist in the arc. These bodies can collide with each other and with the satellite Aegaeon producing dust. In this work, we investigated this hypothesis by estimating the dust produced by these collisions combining N-body and SPH simulations. Our results show that the collisions between the macroscopic bodies are not energetic sufficient to destroy the bodies. On the other hand, the impacts on the satellite is very promising producing a large amount of dust every collision.

Our SPH simulations shows that the impacts on Aegaeon destroy the projectile transforming 10% to 60% of dust material depending on the impact configuration. This result reveal that only one impact with Aegaeon is sufficient to produce the dust material observed in the arc. These results show that the arc can survive for thousands of years due to impacts with Aegaeon. These impacts do not lead to significant mass loss for Aegaeon, which remains intact post-collision.

However, as these bodies gradually break apart, the material for generating new dust diminishes, and the impact frequency decreases. Thus, the arc's lifespan depends on the distribution and total number of the macroscopic bodies. The study did not account for the possibility that each collision could produce additional fragments that may collide again with Aegaeon, potentially extending the arc's lifespan.

In conclusion, the G-ring arc may be temporary and exhibits fluctuating dust levels, dependent on the number and size distribution of macroscopic bodies. Precisely estimating the arc's lifespan is challenging due to these variables. Nonetheless, the presence of these bodies, if confirmed, could be crucial for maintaining the arc through collisions with Aegaeon. A small number of bodies in the arc could lead to intermittent brightness spikes following impacts, whereas a larger population might result in a more stable and consistently bright system.

The work present on this part of the thesis was submitted to to the special issue of Philosophical Transactions A, associated with the Colloquium honoring Prof. Bruno Sicardy in Paris. Future work will involve additional SPH simulations to gain deeper insights into dust production and create maps of dust productions for different sizes of small bodies. Additionally, we will explore the trajectories and velocities of the fragments generated by these impacts. The findings from these studies will be detailed in another paper in preparation.

Part II

Delivering water to the inner solar system

1 INTRODUCTION

Planets in the Solar System exhibit a clear discrepancy with less massive planets located in its inner region and gas and ice giants distributed in its outer part. Consequently, understanding and describing the formation of these planets has been a challenge. To have a successful model we must obey the number of planets, the stability and properties of their orbits, the quantity of water on planet Earth and reproduce the proportion of isotopes of carbon and silicate constituted in the rocky planets and the asteroid belt (CHAMBERS; WETHERILL, 1998a; CHAMBERS; WETHERILL, 2001; IZIDORO et al., 2015).

In this section, we will discuss the main theories for the formation of rocky planets and the origin of the water on Earth, on which this project will be extended. Classical models for the formation of terrestrial planets in the solar system are characterized by evolution, dynamics, collisions, and mass accretion between planetary embryos and planetesimals that collide each other and form larger objects over time, without significant radial movement of mass between the inner and outer regions of the Solar System (CHAMBERS; WETHERILL, 1998a; CHAMBERS; WETHERILL, 2001).

The classical models consider that the terrestrial planets and the giant planets were formed independently. In this model, it is considered that the formation of the giant and the terrestrial planets can be treated separately. However, more recent models and analyses of meteorites show that it can not be treated separately (RAYMOND; MORBIDELLI, 2022). In general, simulations in this scenario present problems with the formation of the planet Mars and with the asteroid belt produced by each of these simulations (CHAMBERS; CASSEN, 2002; IZIDORO et al., 2013; IZIDORO et al., 2014).

More modern models use significant material transfers in the form of bodies of the order of centimeters, called pebbles, which migrate from the outer region to the inner parts of the disc due to hydrodynamic drag to form the “seeds” of planetary and planetesimal embryos (Bitsch; Lambrechts, Michiel; Johansen, Anders, 2015; JOHANSEN et al., 2021). This pebbles accretion model severely mitigates the problems previously described in the classical setting. However, they still cannot explain the ratio of isotopes of various elements such as O, Ti, Ni, Mo, and Nd, present in different amounts on Earth and on Mars, as well as the proportion of carbonaceous and silicate asteroids in the asteroid main belt (RAYMOND et al., 2009; RAYMOND; IZIDORO, 2017b).

The most recent model for the formation of rocky planets was proposed by Izidoro et al. (2022) which uses the concept of pebbles applied to a protoplanetary disk distributed in rings with different compositions of materials, whose disposition is regulated by the temperature and chemistry of the disc. The idea that the solid material is distributed into rings is supported by observations of protoplanetary disks using the high-resolution ALMA radio telescope that shows different systems with multiple structures of rings (HUANG et al., 2018). The trump card of Izidoro et al. (2022) model is to reproduce the distribution of carbon and silicate isotopes in terrestrial planets and meteorites to ring observations of dust straits in protoplanetary disks near the star-forming region.

There is a great debate in the literature about the origin of water on rocky planets, especially on Earth, as well as its abundant presence in C-type asteroids (main composition carbonaceous chondrites) that have about 5-20% of their composition in water (MORBIDELLI et al., 2000; BURBINE et al., 2002; RAYMOND; IZIDORO, 2017b). The most intriguing thing about the existence of these materials is the fact that the proportion of D/H and $^{15}N^{14}N$ isotopes present on planet Earth is equivalent to those presented in meteorites of carbonaceous chondrites related to C-type asteroids (BURBINE et al., 2002; MARTY et al., 2016).

The composition of Comet 67P Churyumov–Gerasimenko allowed to restrict the origin of volatile elements (water, carbon, nitrogen, noble gases) present in the atmospheres of the inner planets. Spectrometry analyses indicate that the contribution of volatile materials from comets on planet Earth was $\leq 1\%$ for water, carbon, and nitrogen. Consequently, these experiments rule out the transport of water to terrestrial planets by comets and Earth materials (MARTY et al., 2016).

Dismissing the delivery of water to Earth by comets, Raymond and Izidoro (2017b) presents a model in which the transport of water on Earth may be a consequence of the growth phase of the giant planets. C-type planetesimals are condensed to approximately between 4 and 9 au, and during this phase, the growth of Jupiter and Saturn disturbs the planetesimals and scatter them in all directions, with a fraction remaining trapped in the asteroid belt and others scattered to the region of terrestrial planets. This way, Izidoro et al. (2014) proposes that volatile elements, as well as water, were formed in the same region of the Solar System and later distributed to planet Earth and the main belt.

Another dichotomy of isotopes in the Solar System occurs in the ratio of carbonaceous isotopes among the planets Earth and Mars (WALSH et al., 2011). As presented in sequence, the classical models are not able to explain these differences. Unlike the others, the ring model proposed by Izidoro et al. (2022) enables the explanation of these isotope dichotomies, as well as the diversity of carbonaceous found in the Solar System. Based on this, in this work, we will study the water delivery model for planet Earth by Raymond and Izidoro (2017b) within the formation model proposed by Izidoro et al. (2022). To this end, we will run simulations of the last stage of accretion of terrestrial planets in the context of the model of rings, considering the scattering of planetesimals when Jupiter and Saturn grow in a gaseous disk (RAYMOND; IZIDORO, 2017b).

1.1 SOLAR SYSTEM FORMATION

The Solar System started its formation with Calcium- and Aluminum-rich Inclusions (CAIs), which are the oldest known chondritic meteorites dating 4.5 billion years. In sequence, the iron meteorites were formed in 1 million years (Myr), accreting the CAIs and reaching several hundred to a thousand kilometers (AMELIN et al., 2002; HALLIDAY; KLEINE, 2006).

These meteorites can be classified into two isotopically distinct groups: carbonaceous and non-carbonaceous. Despite their differences, the ages of these meteorites suggest that they formed simultaneously (AMELIN et al., 2002). However, there is a clear discrepancy in the distribution of neutron-rich isotopes present in each group such as $^{54}C_r$ and $^{50}T_i$ (KLEINE et al., 2020). It suggests

that NC and CC coexisted during the early stages of planet formation but remained physically separated. The separation of carbonaceous and non-carbonaceous meteorites indicates the existence of two spatial separated disks composed of different materials. This suggests that Jupiter's core grew rapidly and reached the critical mass to block the pebble flux within 1-1.5 Myr after CAIs (AMELIN et al., 2002; WARREN, 2011). The presence of both materials in the asteroid belt must be explained by an additional process during the evolution of the Solar System (IZIDORO et al., 2022).

The gas disk existed for about 5 million years (Myr), a timescale consistent with the dissipation of gaseous disks around other stars (MANARA; MORBIDELLI; GUILLOT, 2018). The oldest chondritic meteorites formed roughly 5 Myr after CAIs, possibly in the absence of gas. This suggests that 5 Myr is an upper limit on the lifetime of the gas disk in some regions, given that gas is believed to be necessary for planetesimal formation (JOHANSEN et al., 2014).

Hafnium-tungsten (Hf/W) measurements indicate that the Moon-forming impact occurred roughly 100 million years after CAIs (KLEINE et al., 2009). The presence of highly-siderophile elements in the mantle and crust indicates that they were delivered after the Moon-forming impact (JACOBSON et al., 2014). The total amount of highly-siderophile on Earth can suggest that this impact happened around 100 Myr after CAIs (JACOBSON et al., 2014).

The Solar System's giant planets are thought to have undergone an instability phase, possibly triggered by interactions with a reminiscent planetesimal disk or through self-driven mechanisms (RIBEIRO et al., 2020). The so-called Nice model showed that the giant planets' current orbital configuration (GOMES et al., 2005; TSIGANIS et al., 2005; MORBIDELLI et al., 2005; TSIGANIS et al., 2005; NESVORNÝ; MORBIDELLI, 2012) – as well as the orbital properties of Jupiter's Trojans, the irregular satellites, and the Kuiper belt – could be explained by a dynamical instability in the giant planets' orbits (MORBIDELLI et al., 2005; NESVORNÝ; VOKROUHLICKÝ; MORBIDELLI, 2013; NESVORNÝ, 2015).

Over the last decades, global models of Solar System formation have evolved, replacing classical models with new theories to satisfy the main constraints of the Solar System. According to Raymond and Morbidelli (2022), the main constraints are followed as:

1. **The masses and orbits of the terrestrial planets.** The key quantities include their number, absolute masses and mass ratios, and low-eccentricity, low-inclination orbits.

2. **The masses and orbits of the giant planets**. The number (two gas giants, two ice giants), masses and, orbits of the giant planets are the central constraints. The orbital spacing of the planets is also important, for instance, the fact that no pair of giant planets is located in mean motion resonance.

3. **The orbital and the composition structure of the asteroid belt.** The asteroid belt contains only $\approx 4.5 \times 10^{-4}$ Solar Mass in total mass. The asteroids have eccentric and inclined orbits, with eccentricities ranging from zero to 0.3 and inclinations from zero to just over 20 degrees. The inner main belt is mainly composed of S-type asteroids associated with dry (with water

contents less than 0.1% by mass), ordinary chondrites, while the outer main belt is dominated by C-type asteroids linked to water-rich carbonaceous chondrites (contain ≈ 10% water by mass).

4. **Isotopic compositions in the bodies of the Solar System.** The ratio of D/H and other isotopes restricts the distribution of the bodies and its distribution over the Solar Solar. This topic will be better discussed in the next section.

The first model to try to reproduce the main constraints of the Solar System was the so called Classical Model, which is based on the concept of local planet growth (WETHERILL, 1992; CHAMBERS; WETHERILL, 1998b; CHAMBERS, 2001; RAYMOND et al., 2009). More recent models invoke different mechanisms, such as the migration of giant planets introduced by the Grand Tack model (WALSH et al., 2011) and the so-called Nice Model (GOMES et al., 2005; TSIGANIS et al., 2005; MORBIDELLI et al., 2005), a discontinuous disk of solids as described by the Low-mass Asteroid Belt model (HANSEN, 2009; IZIDORO et al., 2015; RAYMOND; IZIDORO, 2017a), and early instability among the orbits of the giant planets (CLEMENT et al., 2018; CLEMENT et al., 2019). Fig. 1.1 an illustration of three different models: Grand Tack, Low-mass asteroid belt and Early Instability.

Figure 1.1 – Cartoon comparison between the global evolution of three main models for Solar System formation.

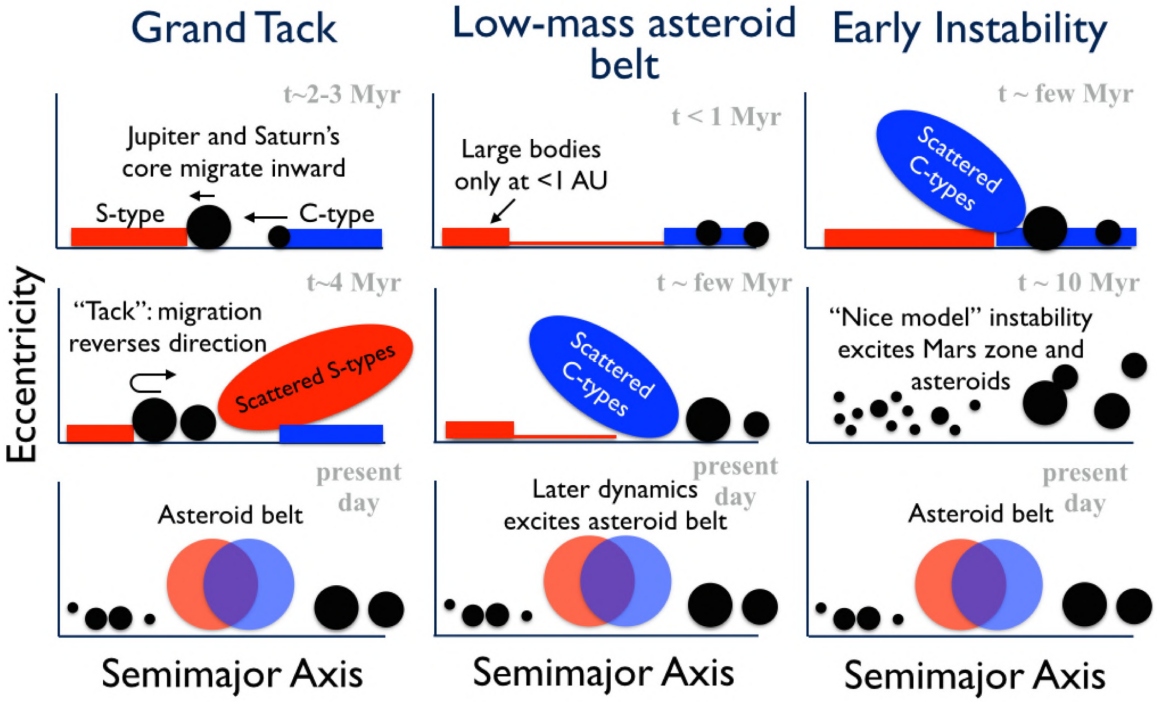

source: (RAYMOND; MORBIDELLI, 2022)

However, the analysis of isotopes from different types of meteorites and Earth samples has changed our understanding of planet formation (WARREN, 2011). The isotopic ratios of different elements have introduced new constraints for the Solar System, which introduced the concept of pebble accretion during the growth of terrestrial planets (LEVISON et al., 2015). Pebble accretion has been integrated into contemporary models, introducing new ideas for planet formation (KATAOKA et al., 2013). The

most complete model available at present is the Ring Model proposed by Izidoro et al. (2022), which will be the model used in this work. In sequence, we will briefly describe the concepts of each of the main theories for planet formation and then discuss the origin of water and volatile elements on Earth.

1.1.1 The Classical model

The classical model of terrestrial planet formation is based on two main hypotheses. The first one says that the planets formed approximately at their current positions and the second one says that the formation of the giant and the terrestrial planets can be treated separately. This model uses different continuous planetary disk embryos that are evaluated over millions of years to form simultaneously the terrestrial and giant planets (RAYMOND; MORBIDELLI, 2022).

However, the main problem of this model is the so-called small Mars problem (WETHERILL, 1992). This name was introduced because the tendency of the Classic Model to produce Mars analogs that are more massive than the real Mars. As a consequence, it is difficult to match the observed 9:1 Earth/Mars mass ratio observed in the Solar System (RAYMOND et al., 2009; RAYMOND; QUINN; LUNINE, 2006). Additionally, this model also faces challenges in explaining the characteristics of the main asteroid belt, systematically producing large embryos, and not matching the distribution of eccentricity and inclination of the asteroids.

This 'small Mars' problem, first identified by (WETHERILL, 1992) and later highlighted (RAYMOND et al., 2009), represents a significant limitation of the classical model. This problem raised the necessity of alternative models for the formation of the inner Solar System to explain the Earth/Mass mass ratio and the other characteristics of the Solar System.

1.1.2 The Grand Tack model

The Grand Tack model, proposed by Walsh et al. (2011), suggests that Jupiter and Saturn migrated during the gas phase of the Solar System Formation. In this scenario, Jupiter formed first and migrated inward, while Saturn accreted gas lately. After Saturn reached its current mass, it also migrated inward and captured Jupiter into resonance. Then, the planets became trapped in the resonance and started migrating outward up to their current positions. The velocity of the migration depends on the disk properties and also the gas dissipation time (RAYMOND; MORBIDELLI, 2022).

This migration scenario is based on hydrodynamic simulations of orbital migration. In these simulations, the giant planets grow accreting gas and as a consequence create gaps in the protoplanetary disk (LIN; PAPALOIZOU, 1986; WARD, 1997). The Grand Tack model successfully solved the *small Mars' problem* and also matches the characteristics of the terrestrial planets (WALSH et al., 2011; JACOBSON; MORBIDELLI, 2014). However, as Jupiter and Saturn migrated inward and outward, they severely depleted the asteroid belt, and at the same time mixed the inner and outer distribution of S and C type asteroids in the asteroid belt.

Raymond and Morbidelli (2022) mention that the potential Achilles heel of the Grand Tack model of the mechanism of outward migration itself. This mechanism requires a limited range of

mass ratios between Jupiter and Saturn certain mass ratios, typically between 2:1 and 4:1 (MASSET; SNELLGROVE, 2001). This dependence is difficult to account for because the mass ratio of a gas giant should be constantly changing during its gas accretion phase. Additionally, there may be geochemical constraints related to accretion rates within the Grand Tack (RAYMOND; MORBIDELLI, 2022).

1.1.3 The Low-mass Asteroid belt model

The Low-Mass Asteroid Belt model proposes that Mars' small mass is a consequence of a previous discontinuous disk of planetesimals based on the concept of an edge in the initial distribution of planetary embryos or planetesimals (HANSEN, 2009). These discontinuous disks have a material depletion beyond the Earth orbits. The idea of this discontinuous distribution of planetesimals came from simulations of Kataoka et al. (2013) that showed that the dust immersed in the gas disks tends to accumulate in certain regions generating planetesimal rings among the gas disk.

Hansen (2009) showed that this material depletion can explain the distribution of the terrestrial planets resulting in a large Earth/Mars mass and a small Mercury/Venus mass ratio arising from depletion inside Venus's orbit. This model suggests that there were no planetesimals initially formed between Earth and Jupiter. However, even with no material initially distributed in the region of the asteroid belt, it can be filled from planetesimal scattered during the growth of the terrestrial and the giant planets that gravitationally scatter the near planetesimals to all directions (IZIDORO et al., 2015; RAYMOND; IZIDORO, 2017b).

Raymond and Morbidelli (2022) mention that the main uncertainty of the Low-Mass Asteroid Belt model is the initial conditions of the Solar System. They mention that the main challenge of this model is to satisfy multiple factors like disk observations and interpretation (including studies of ALMA-detected disks), meteorite constraints, and the distribution of non carbonaceous chondrite ages.

1.1.4 The Early Instability model

The Early Instability model, developed by Clement et al. (2018), Clement et al. (2019), proposes that the giant planets' instability occurred approximately 10 million years after the gaseous disk dissipated. This model is similar to the classical model but it invokes a dynamical instability around 10 million years into the simulation. This instability mainly perturbs the orbits of inner Solar System objects. Consequently, the asteroid belt is significantly depleted and difficult the Mars growth (it happens because of the well-known ν_6 resonance). The growth of Earth and Venus remains relatively unaffected and aligns with the classical model's predictions (RAYMOND; MORBIDELLI, 2022).

The strongest characteristic of the Early Instability model is its stochastic nature. As a consequence, numerous numerical simulations must have a confident statistical result. Simulations of the Early Instability model reveal that systems providing the best match to the outer Solar System characteristics also tend to offer an accurate representation of the terrestrial planets' properties (CLEMENT et al., 2018; CLEMENT et al., 2019). Raymond and Morbidelli (2022) mention that the main problem of the Early Instability model is to determine the exact time of the instability. This time must be faster enough to perturb the inner Solar System, but at the same time must agree with the cometary bombardment

that happened in the late stage of the terrestrial planet's growth. Even if this bombardment delivers a relatively small mass to Earth, it could significantly contribute to Earth's noble gases.

1.1.5 The Ring Model

The Ring Model, proposed by Izidoro et al. (2022), is composed of three rings of planetesimals resulting from pressure bumps within the protoplanetary disk. In this model, they propose the existence of pressure bumps near three key condensation regions[1]: the silicate sublimation line (around T $\approx$ 1400 K), the water snowline (at T $\approx$ 170 K), and the CO snowline (at T $\approx$ 30 K). In short, if pressure bumps exist in a gaseous disk, planetesimals form in rings instead of a continuous disk. This ring architecture is consistent with the structure of young disks around other stars.

Fig. 1.2 illustrates the evolution of the planet-forming disk during the gaseous disk phase. As a consequence, the authors showed that pebbles accumulate at these pressure bumps, leading to the creation of three planetesimal rings: a thin ring located close to 1 au, a wide ring around 3-4 au to 10-20 au, and a last ring located around 20 au to 45 au.

The trump card of the Ring Model was to match the isotopic 'dichotomy' of the Solar System, where the pebble remained unmixed during the early stages of planet formation. As previously stated, the parent bodies of NC and CC meteorites most likely formed separately from disparate dust and pebble reservoirs that remained disconnected for 2-4 million years. The Ring model also explains the ratio of various isotopic elements on Earth, Mars, and the origin of different types of meteorites. The authors mention that the central ring contains sufficient material to explain the rapid growth of the cores of the giant planets, while the last ring aligns with dynamical models that suggest the existence of a primordial planetesimal disk in the early Solar System beyond the current orbit of Uranus.

The simulations using a distribution of three rings of planetesimals also match the radial distribution of the terrestrial planets, their masses, and orbits. The Ring Model also reproduces the ratio of Earth/Mars mass resulting from the thin disk of solids present in the terrestrial planets region.. Fig. 1.3 illustrates the migration of the three pressure bumps during the evolution of the Solar System formation. Finally, this model also explains the dichotomy of the asteroid belt presenting two different mechanisms for populating the NC and CC asteroids. The NC asteroids were scattered from the inner ring during the growth of the terrestrial planets, while the CC asteroids came from the middle ring during the growth of the giant planets, as illustrated in Fig. 1.3.

Finally, the success of the Ring Model come from matching not only the orbits and mass distribution but also the chemical and isotopic constraints of the Solar System. This new model suggests a new proposal for Solar System formation where the pressure bumps are responsible for the formation of the disk of planetesimals which are distributed into three main rings composed by different chemical elements rather than a continuous disk for the formation of the rock planets.

[1] region in the protoplanetary disk where the temperature and pressure conditions allow the transition between gaseous and solid phases.

Figure 1.2 – Evolution of the Sun's planet-forming disk, assuming the existence of three pressure bumps: near the silicate sublimation line, at the water snowline, and the CO snowline.

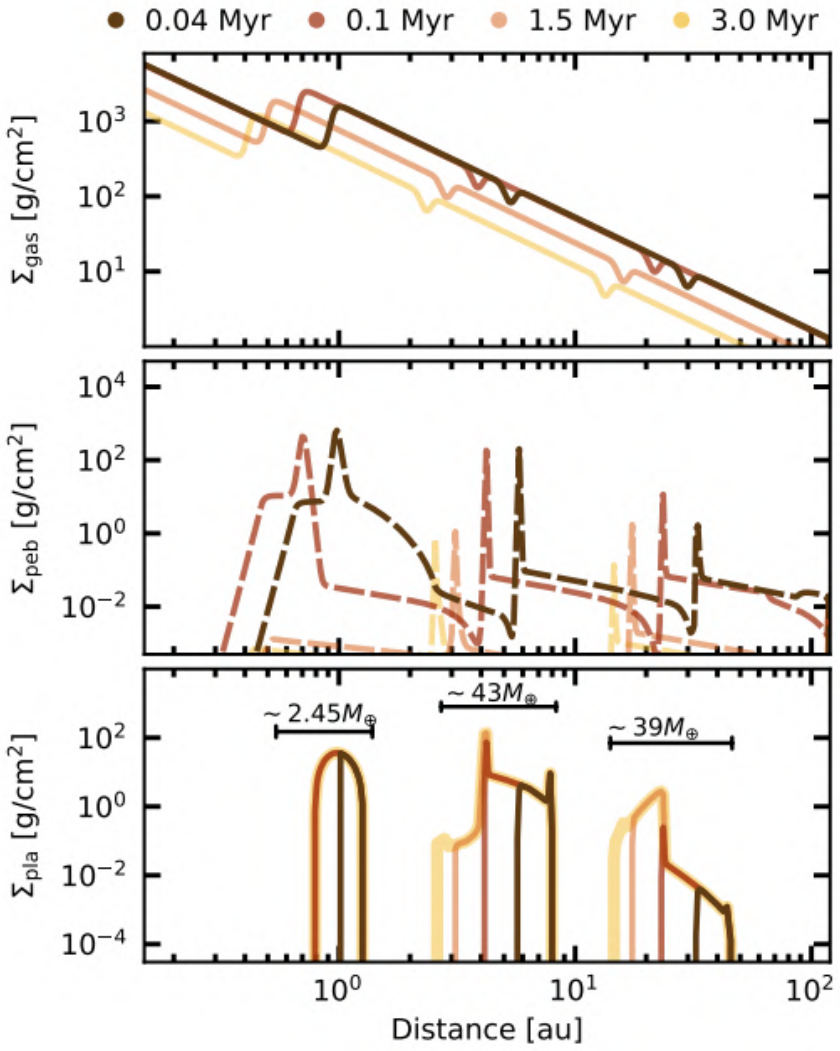

source: Izidoro et al. (2022)

Figure 1.3 – A schematic showing the evolution of the Solar System assuming a Sun's natal disk distributed into three main rings associated with the CO snowline, H_2O snowline, and silicate sublimation line.

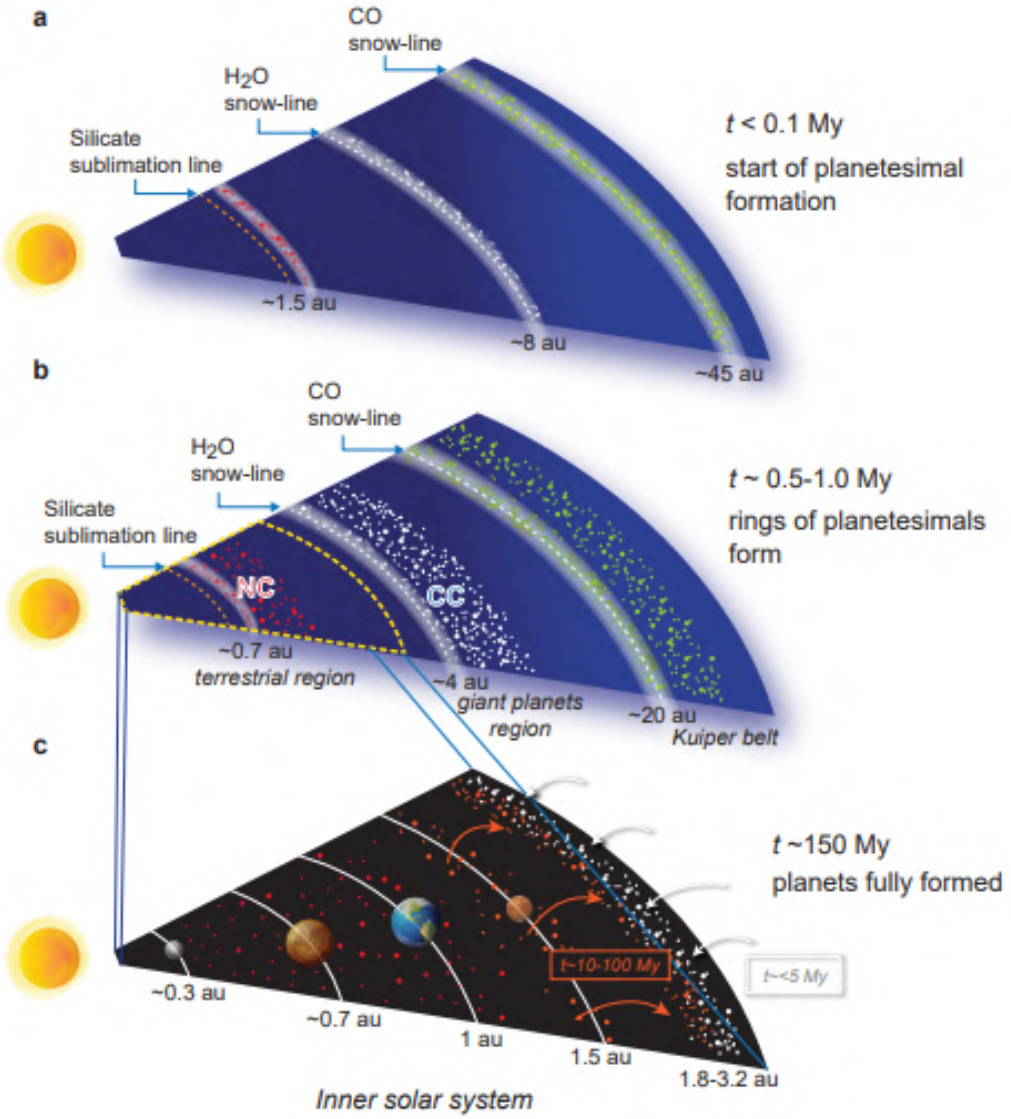

source: (IZIDORO et al., 2022)

1.2 ORIGIN OF WATER ON EARTH

There is a great debate about the origin and existence of water on Earth and the other terrestrial planets. The most accepted theory is that the water and volatiles elements came from bodies from different regions during the formation of the Solar System due to the position of the water snow line (IZIDORO et al., 2022). Even though the planet Earth is covered by 70% liquid water, it represents only 0.025% of the Earth's total mass. However, most of Earth's water is present in its interior. The key to determine the main sources of water on a planet is the D/H ratio of the water's H isotopic composition (PIANI et al., 2021; IZIDORO; PIANI, 2022).

Since comets are water-rich bodies, it was historically considered to be the source of water for Earth and the other terrestrial planets. However, the material captured by the Rosetta mission showed that the ratio D/H and $^{15}N/^{14}N$ is much higher in the comets than that one found on the Earth's oceans making their contribution very limited (MARTY et al., 2016; IZIDORO; PIANI, 2022). Fig. 1.4 shows the ratios D/H and $^{15}N/^{14}N$ present on different bodies around the Solar System. It is clear from this Figure that the comets were not the main source of these materials present on Earth. On the other hand, the ratios present on Earth and Moon are compatible, suggesting that both bodies were formed together as proposed by Hartmann and Davis (1975).

Figure 1.4 – Distribution of $^{15}N/^{14}N$ isotope ratios vs. D/H ratios of Solar System objects.

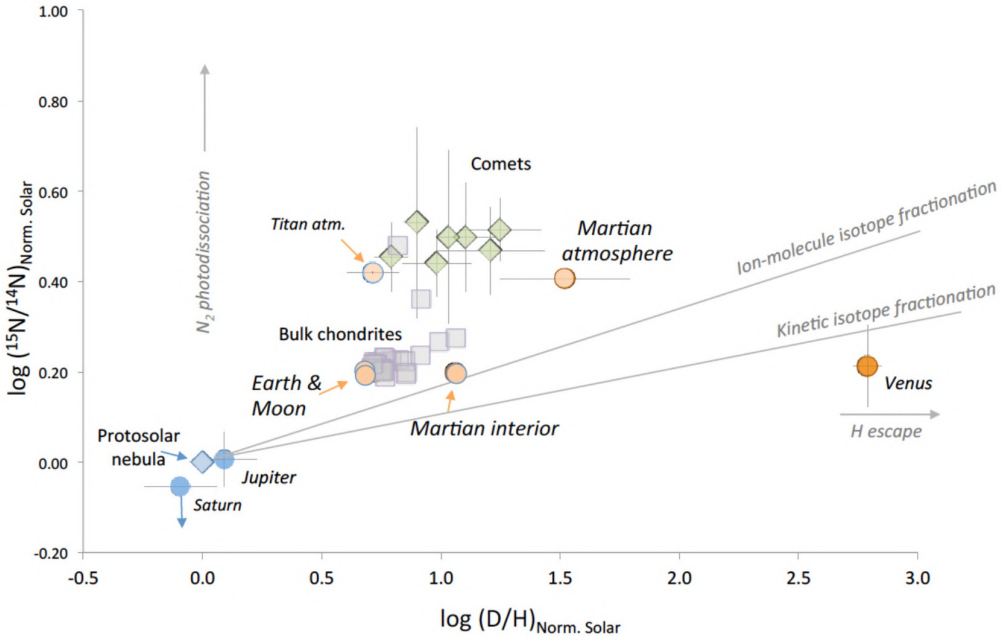

source: Marty et al. (2016)

Not only on Moon, but also the material from meteorites analyses also shows a similar ratio of D/H and $^{15}N/^{14}N$ that one found on Earth's oceans. The meteorites are represented as bulk chondrites in Fig. 1.4. It suggests that the asteroids could be the main source of water to the terrestrial planets (MARTY et al., 2016; IZIDORO; PIANI, 2022; PIANI et al., 2021). Fig 1.5A illustrates the quantity of water present on Earth, asteroids and comets. The non carbonaceous chondrites (NCs) (represented by the ordinary and enstatite chondrite groups, OCs and ECs, respectively) are considered to be water-poor

objects carrying heavy elements, while the carbonaceous chondrites (CCs) are water-rich elements and abundant with volatiles elements. Thus, the main possible source of water to Earth are the CC that were formed in the second ring as proposed by the Ring Model (IZIDORO et al., 2022).

Figure 1.5 – Measured $^{15}N/^{14}N$ isotope ratios vs. D/H ratios of Solar System objects.

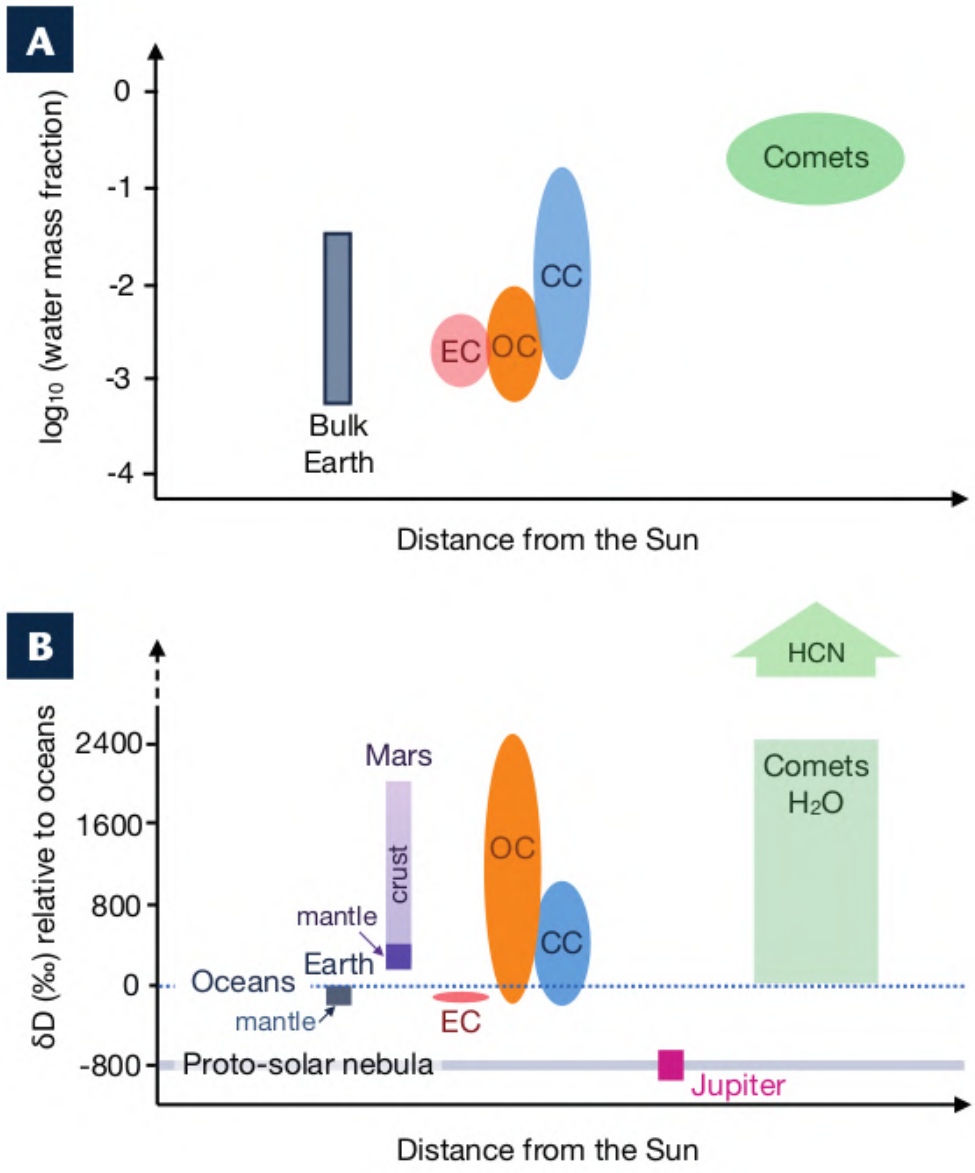

source: Izidoro et al. (2022)

Fig. 1.5B illustrates the ratio of D/H (represented as ΔD) for the objects of the Solar System in the function of the distance from the Sun. The Proto-solar nebula and Jupiter have very low D/H ratios of $\approx 21 \times 10^{-6}$ (or $\delta D \approx -800‰$). The water on Earth has a D/H ratio is $\approx 156 \times 10^{-6}$ (or $\delta D \approx -800‰$), which is a factor of seven higher than that of Jupiter/Sun. Outer Solar System objects generally show much higher D/H ratio which makes it difficult to say that these bodies are responsible for the water on Earth. The CC and OC have a very large range of D/H ratio, while the EC shows a similar ratio to the Earth's ocean (BOCKELÉE-MORVAN et al., 2015; IZIDORO; PIANI, 2022; PIANI et al., 2021).

In this work, we aim to estimate the total amount of water that was delivered from the outer region

to the terrestrial planets during the growth of Jupiter and Saturn in the Solar System formation. In the next section we will explain this hypothesis for the delivery of water to Earth.

1.2.1 Delivering water to the terrestrial planets

The growth of the giant planets, their orbital migration and dynamical evolution played a key role in delivering water to the terrestrial planets during the early stage of the Solar System formation (RAYMOND; MORBIDELLI, 2022; IZIDORO et al., 2022). In this period, Jupiter and Saturn increased their mass from approximately three to hundreds of Earth masses within about 10^5 years, this phenomenon is called as "rapid gas accretion"during the early stages of giant planet formation. The rapid growth of Jupiter and Saturn perturbed the orbit of near planetesimals, scattering them in all directions, some of them are scattered inward in the direction of the asteroid belt and eventually crossing the terrestrial planets region, while others are scattered in the direction of orbits of the trans-neptunian (RAYMOND; IZIDORO, 2017b).

According to the Ring model, there is a clear separation on the distribution of elements during the early stage of the Solar System (IZIDORO et al., 2022). The material was distributed into three main rings associated with the silicate sublimation line (located between 1.5 to 2.5 ua), the H_20 snowline (located between 4.0 to 20 ua), and the CO snowline (located beyond 40 ua). To mix the compositions of these materials and deliver water to the terrestrial protoplanets we must invoke the rapid growth of the giant planets.

Fig. 1.6 illustrates the effect of the growth of Jupiter and Saturn scattering the planetesimals in all directions. This mechanism was proposed by Raymond and Izidoro (2017b) where they investigated the efficiency of Jupiter and Saturn scatter C-type planetesimals to the asteroid belt and estimated the amount of material that cross the terrestrial planets formation zone. The relative number of planetesimals that became trapped in the main asteroid belt versus those that were scattered further inward toward the terrestrial planets, where they could deliver water, depended on the strength of gas drag. Strong gas drag, often associated with a massive inner gas disk or smaller planetesimals, led to planetesimals primarily being trapped in the outer regions of the main asteroid belt. On the other hand, weak gas drag, resulting from a low-density inner disk or larger planetesimals, allowed planetesimals to be scattered farther inward, potentially delivering water to the terrestrial planet-forming region and delivering water.

Finally, the dynamical evolution of the giant planets could also contributed to the delivery of water to Earth. The effectiveness of the delivery of these water-rich planetesimals depends on the gas dissipation time as well as the use of migration or non-migration for the formation of the giant planets. When the gas dissipates fast, the planetesimals maintain high eccentricities increasing the chance of crossing the orbits of terrestrial planets. Likewise, migration disturb their orbits, increasing the chance of crossing the terrestrial region.

In this work we will investigate the effect of these parameters on the delivery of water to the terrestrial planets. In the same way, we will analyze their effect on the distribution of material placed

in the asteroid belt as well as the distribution of C and S types of asteroids for each different numerical setup. In the next section, we will describe the numerical setup of the simulations.

Figure 1.6 – Dynamical evolution of the Solar System and water delivery to the terrestrial planets. The plot shows the evolution of Jupiter and Saturn masses and how they can scatter the nearby planetesimals towards the inner and outer Solar System

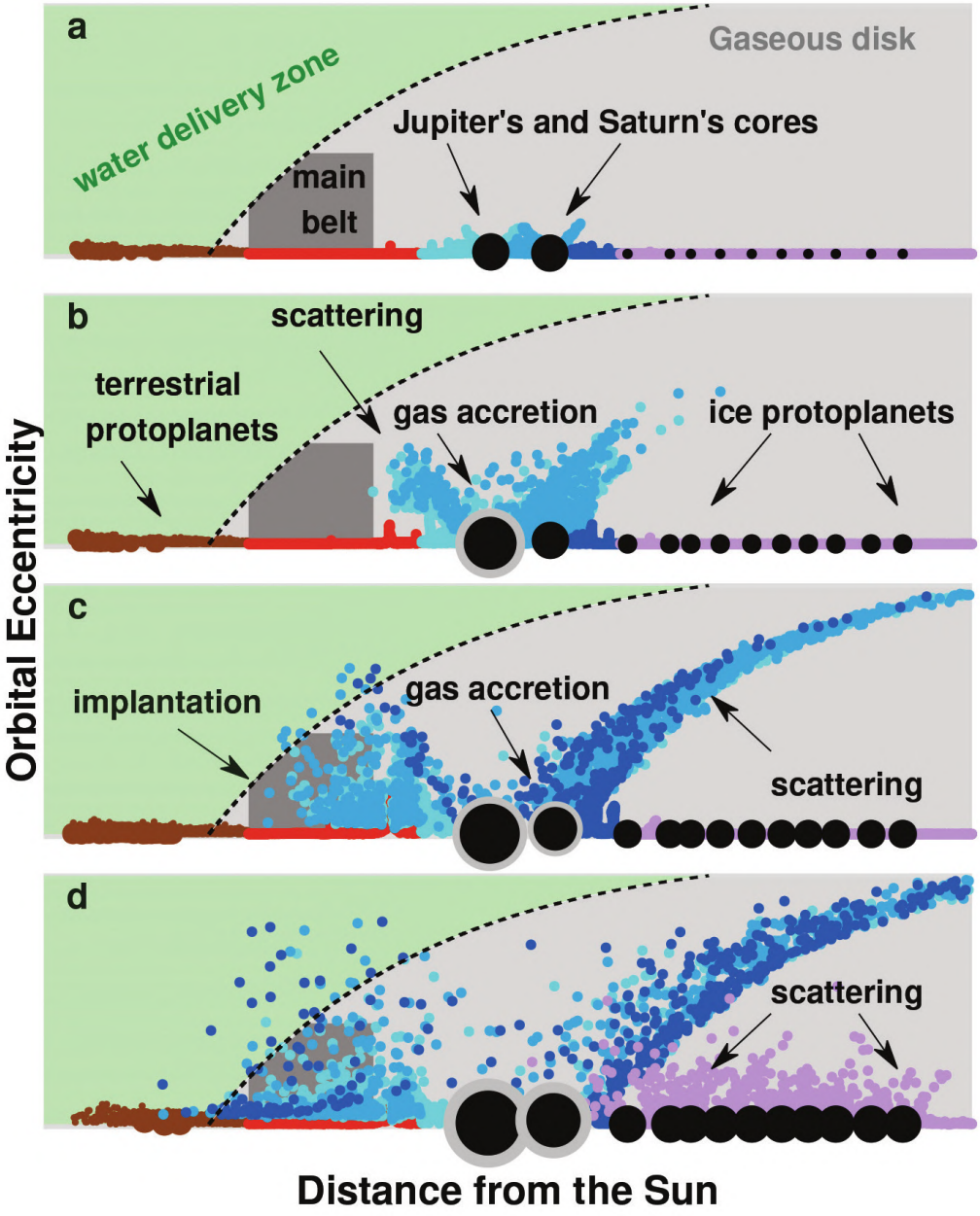

source: Izidoro et al. (2022)

2 NUMERICAL SETUP

We numerically simulated the formation of the terrestrial planets using N-body simulation with the integrator Symba from the package swift. The package, originally developed by Levison and Duncan (1994) and later updated by Duncan, Levison and Lee (1998). We chose to use the Symba package because it is parallelized and faster than other integrators. For each of simulation we performed we used 4 cores. In this work, we performed a total of 160 simulations using a 640 cores.

The numerical setup of our implementations is based on the code used in Raymond and Izidoro (2017b) where they have included the surface gas disk, the growth of Jupiter and Saturn, and the aerodynamic gas drag including the dumping of eccentricity and inclination in the Symba integrator. We divided our simulations into three main phases, the formation of the planetary disk, the gas phase, and after the gas is dissipated.

In the first one, we use the semi-analytical code developed by Izidoro, Bitsch and Dasgupta (2021) to create the disk of planetesimals and planetary embryos after 3 million years. The second one is composed by the gas phase when Jupiter and Saturn start to accrete the gas and increase their mass up to their current masses. The gas dissipates after 500 thousand years. In this phase, we also explored two different types of scenarios for the formation of giant planets:

- in the first one, we grow Jupiter and Saturn in situ trapped into the 3:2 resonance,
- in the second one, we migrate Jupiter and Saturn inward from outer orbits up to the 3:2 resonance.

We simulated the gas phase using the code based on (RAYMOND; IZIDORO, 2017b). In the last one, the gas is dissipated and we numerically integrate the systems only using the gravitational force up to 100 million years. In the last phase, we explore the effect of having an early and late instability.

Our initial conditions include Jupiter and Saturn's cores, each starting at 3 Earth mass, plus the embroys and 1000 effectively massless planetesimals distributed from 0.5 to 1.5 UA for the inner ring (silicate ring) and 1000 massless planetesimals distributed from 3.0 to 5.0 au for the H_20 ring. The mass of the embryos was calculated using the semi-analytical code proposed by (IZIDORO; BITSCH; DASGUPTA, 2021) with a 2-3 Hill radius gap around each one. The cores and embryos interact gravitationally with all other bodies, while the planetesimals feel the bodies but do not affect them. Simulations were integrated for 0.3-100 Myr with a timestep of 0.1 year. Particles were removed from the simulation if they were closer than 0.35 au from the Sun or farther than 200 au.

In sequence, we are going to summarize how we performed each of the three phases and how the forces were implemented and applied in the code.

2.1 DISK OF SOLIDS

To distribute our initial conditions we followed the ring Model proposed by Izidoro et al. (2022) where we distributed the planetesimals into two main rings (located in the silicate and water zones). The inner ring has planetesimals and planetary embryos distributed from 0.5 to 1.5 UA. The composition of the inner ring is mainly silicates and its total mass is equal to 2.5 Earth Mass. On the other side, we uniformly distributed the C-type planetesimals in the outer ring from 5.0 to 20 UA. The total mass of the second ring is a free parameter of our simulations because the main goal of this project is to determine the best sets of parameters that fit the constraints of the Solar System discussed in Section 1.1.

To evaluate the growth and distribution of the embryos in the inner disk we followed the semi-analytical model introduced by Izidoro, Bitsch and Dasgupta (2021). This code considers several processes that the planetesimals suffer when they are growing up to become embryos, such as gas-drag damping, gravitational interaction with other planetesimals, viscous stirring, dynamical friction due to interactions with protoplanetary embryos, and collisional damping (KOKUBO; IDA, 2000; CHAMBERS, 2006). These different interaction processes usually leads to a state of equilibrium, in which the random velocity of the planetesimal is in the dispersion-dominated regime ($e_{\rm pla},\, i_{\rm pla} \gtrsim r_{\rm mH}/(2^{1/2} a_{\rm Emb})$)

$$r_{\rm mh} \approx a_{\rm Emb} \left(\frac{2 m_{\rm Emb}}{3 M_{\rm Sun}} \right)^{(1/3)} \tag{2.1}$$

where $e_{\rm pla}$, $i_{\rm pla}$ are the eccentricity and inclination of the planetesimals close to the embryo, $r_{\rm mh}$ is the mutual Hill radius, $m_{\rm Emb}$ is the mass of the embryos, and $a_{\rm Emb}$ is the semi-major axis.

$$e_{\rm pla} = 2 i_{\rm pla} = 2.7 \left(\frac{R_{\rm pla} \rho_{\rm pla}}{\Delta C_d a_{Emb} \rho_x} \right)^{1/5} \frac{r_{mH}}{2^{1/3} a_{\rm Emb}} \tag{2.2}$$

The growth of a protoplanetary embryo via accretion of planetesimals in the dispersion-dominated regime is well described by the particle-in-a-box approach. The growth rate of an embryo depends on embryo size, local planetesimal surface density, and the relative velocities of the embryo and planetesimals during close approaches. The accretion rate of an embryo is given by (e.g., (SAFRONOV, 1972); (GREENBERG et al., 1978))

$$\frac{d M_{\rm Emb}}{dt} \approx F \frac{\sum^{*}}{\sin{(i_{\rm pla})} a \sqrt{2}} \pi R_{\rm Emb}^2 \left(1 + \frac{v_{\rm esp^2}}{v_{\rm rel^2}} \right) v_{\rm rel} \tag{2.3}$$

where $v_{\rm esc}$ is the escape velocity, $v_{\rm rel}$ is the relative velocity between the planetesimals, $\sum^{*}_{\rm pla}$ is the updated density of planetesimals and F is the factor to compensate for the underestimation of the accretion ratio.

$$v_{rel} = v_k \sqrt{\frac{5}{8} e_{\text{pla}}^2 + \frac{1}{2} \sin^2 i_{\text{pla}}} \tag{2.4}$$

We then calculate the growth of the embryos in the inner ring using the equation 2.3. In this step, we separate the embryos between 5 to 10 Hill's radius using the same separation proposed by Kokubo and Ida (2000). The typical mass of the planetary embryos after 3 million years is about one Moon mass (IZIDORO; BITSCH; DASGUPTA, 2021). Here, we chose to use this model to evaluate also the effect of the orbit period. The orbit period decrease the number of encounters with other planetesimals as the semi-major axis increases (KOKUBO; IDA, 2000; CHAMBERS, 2006).

Fig. 2.1 illustrates the mass evolution of one planetesimal at 1 au comparing the mass obtained from numerical simulations and using the model proposed by Izidoro et al. (2022). Fig. 2.2 shows an example of one disk of embryos using the Isolation Mass proposed by Kokubo and Ida (2000) and using Safranov regime described in Izidoro et al. (2022). This Figure shows that mass decreases when the semi-major increase. Finally, after evaluating the mass and location of all the embryos we distributed the mass of the planetesimals following a power-law disk mass distribution $\sum r^{-}1$ to complete the 2.5 Earth Mass of the inner ring.

Figure 2.1 – Comparison of planetesimal accretion methods for a stationary embryo at 1 au within an MMSN protoplanetary disk. The black line represents growth using the Izidoro et al. (2022), green line denotes Chambers (2006) analytical method, and blue/yellow lines depict results from high-resolution N-body simulations.

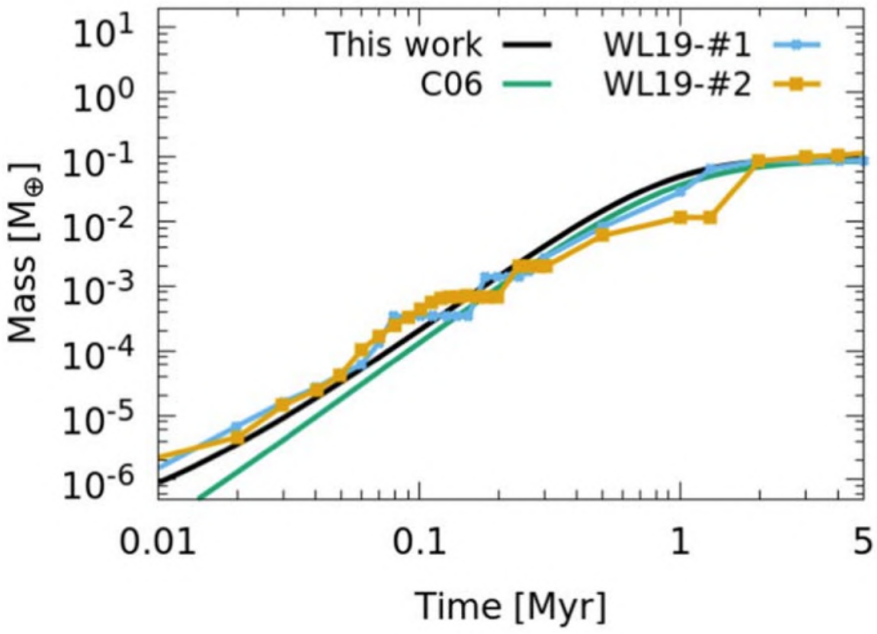

source: Izidoro et al. (2022).

2.2 DISK OF GAS

After determining the mass of the embryos over 3 million years and distribute the planetesimals into the two rings, we start the gas phase with Jupiter and Saturn cores at 3 Earth masses. In this phase, we explored two different scenarios for the formation of the giants planets, Jupiter and Saturn growing

Figure 2.2 – Disk of solids produced using the Isolation Mass and the Safranov Regime. The left graphs illustrates a distribution using $\Sigma \propto r^{-1}$, while the right using $\Sigma \propto r^{5.5}$.

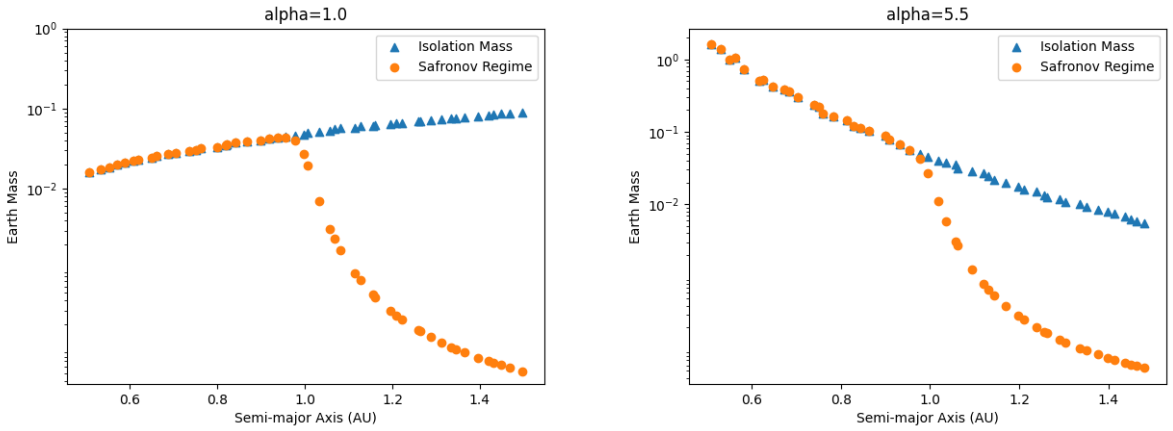

in situ and migrating following the Nice Model. These scenarios are similar to the ones explored in Raymond and Izidoro (2017b).

The surface density of the gas is initially is described by

$$\Sigma = 4000 \left(\frac{r}{1\text{au}}\right)^{-1} g/cm^2. \tag{2.5}$$

This profile is few times more massive than the 'minimum-mass solar nebula' model (Weidenschilling, 1977; Hayashi, 1981) and consistent with profiles inferred from observations of the outer parts of protoplanetary disks (RAYMOND; IZIDORO, 2017b). The disk has a uniform scale height of H/r = 0.05. The mass of the giant planets increases linearly following the timescale τ_{grow}. Here we explored the timescale to be between 10^2 and 10^5 years.

However, as Jupiter and Saturn start to accrete the gas and increase their mass they modify the structure of the disk creating an annular gap (CRIDA; MORBIDELLI; MASSET, 2006). The code interpolates the disk's surface density with the density profile taken from hydrodynamical simulations by Morbidelli and Crida (2007). This process is made in sequence interpolating the gaps created by Jupiter and Saturn. The gaps are created at the the same timescale as the planet's growth. Fig. 2.3 illustrates the structure of the disk at the start of the simulation and after Jupiter and Saturn grow. The disk dissipates exponentially at a timescale of $\tau_{gas} = 5 \times 10^5$ years.

2.2.1 Growing Jupiter and Saturn

In this work, we explored two different scenarios for the formation of Jupiter and Saturn. In the first scenario we grow both planets in situ trapped into the 3:2 mean motion resonance. In the second scenario Jupiter and Saturn migrate inward from 10 UA and 15 UA, respectively, up to the 3:2 mean motion resonance.

For the second scenario we chose to start Jupiter and Saturn at these positions because of the constraint of a low mass into the main belt. Deienno et al. (2022) explored different initial positions for

Figure 2.3 – Gas disk surface density in the function of the semi-major axis during the mass evolution of Jupiter and Saturn. The black line represents the initial gas disk surface density, the green line after Jupiter grow, while the blue line when Jupiter and Saturn reached their current mass.

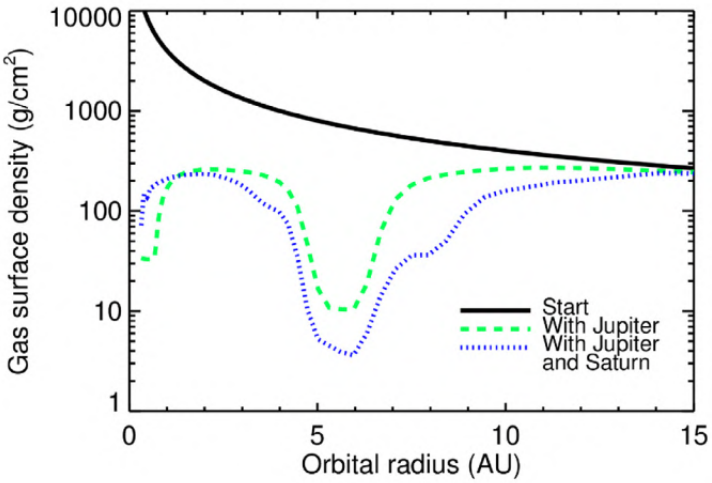

source: Raymond and Izidoro (2017b)

Jupiter and Saturn migrating inward and investigate the effect of these parameters on the implantation ratio of C-type planetesimals. Fig. 2.4 illustrates the initial conditions of their simulations (left panel) and the total amount of C-type material implanted into the main asteroid belt (right panel).

Figure 2.4 – Different initial conditions for the migration of Jupiter and Saturn (left) and the total amount of material put into the asteroid belt.

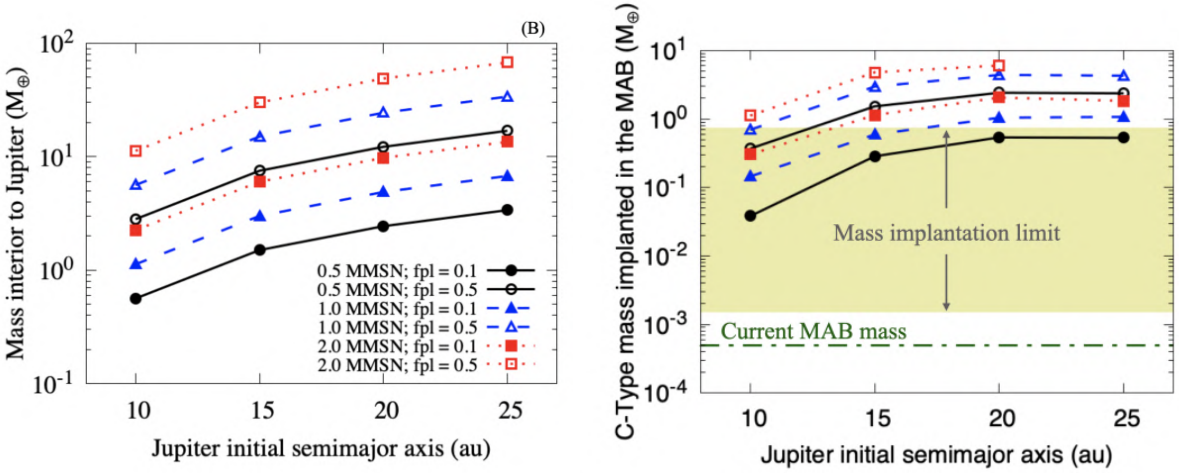

source: Deienno et al. (2022)

The results from Deienno et al. (2022) shows that it is more likely that Jupiter formed between 10 and 15 au to reproduce the current low mass of the main asteroid belt. Otherwise, if Jupiter started from outer orbits it would put a large amount of mass into the main asteroid belt. This is because when Jupiter and Saturn migrate from outer orbits they perturb the orbits of more objects implanting them into the asteroid belt. A very large scale migration of Jupiter would not be a problem if almost no planetesimals were available inside Jupiter's orbit.

Fig. 2.4 shows that, for example, Jupiter could have migrated from 15 au if the interior disk mass was ≈ 3 Earth Masses (1.0 MMSN, fpl = 0.1, aJup= init 15 au, adisk = 5–13 au) or 10 au if M_{disk}=5.64 Earth Masses (1.0 MMSN, fpl = 0.5, aJup= init 10 au, adisk = 5–8 au). This is plausible within models where Jupiter would form from a ring of planetesimals around the water-ice line that extends up to 10–15 au (IZIDORO; PIANI, 2022).

Finally, Fig. 2.5 shows an example of the evolution of the mass, semi-major axis and eccentricity of Jupiter and Saturn over the two different scenarios we explored. The left graphs show the evolution for the case when Jupiter and Saturn grow in situ, while the right panels show the evolution for the migration case. These graphs shows that the migration increases the eccentricity of the planets as they start accreting mass.

Figure 2.5 – Evolution of mass, semi-major axis and eccentricity during the growth of Jupiter and Saturn. The left plots show the case when they grow in-situ, while the right ones when they migrate inward.

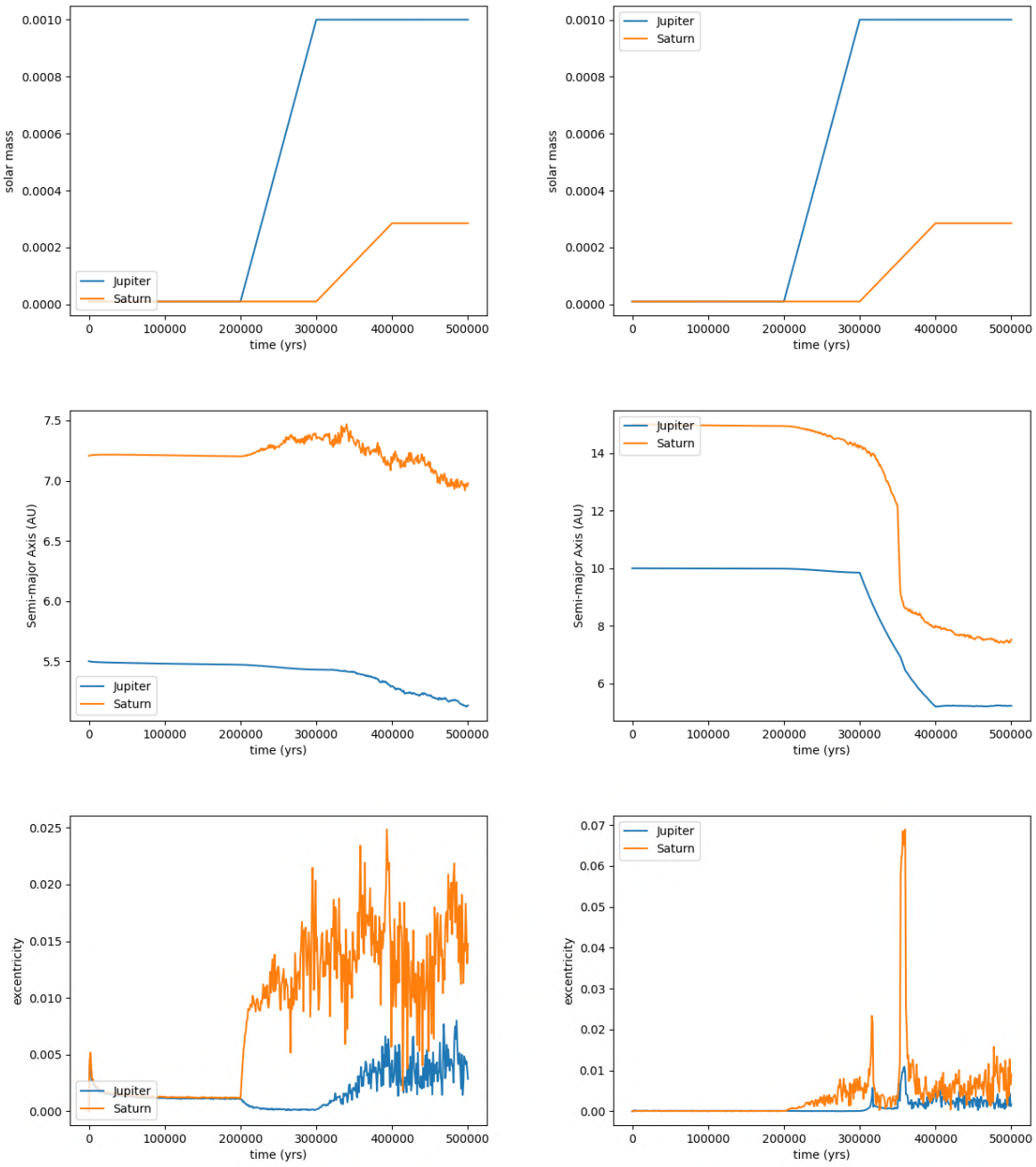

2.2.2 Gas Effects

In this section we will discuss the main effects of the gas on the embryos and planetesimals. The aerodynamic gas drag implemented in our simulations follows the formalism proposed by Adachi, Hayashi and Nakazawa (1976) that was implemented into the integrator Swift by Raymond and Izidoro (2017b). Planetary embryos and planetesimals interact differently with the gaseous protoplanetary disk. While small planetesimals only feel the headwind of the gas, the embryos also excite density waves in the disk .

Planetesimals feel aerodynamic gas drag from the disk causing them to lose angular momentum (ADACHI; HAYASHI; NAKAZAWA, 1976). We compute the gas drag acceleration on planetesimals using the following equation:

$$\vec{a}_{drag} = \frac{3C_d\rho_g \mathrm{v}_{rel}}{4\rho_p D}\vec{\mathrm{v}}_{rel}. \tag{2.6}$$

where C_d is the drag coefficient, ρ_p and D are the planetesimal's bulk density and diameter. The $\vec{\mathrm{v}}_{rel}$ vector is the relative velocity of the object with respect to the surrounding gas and ρ_g is the gas density at the planetesimal's immediate location (such that planetesimals on eccentric orbits feel changing gas drag over the course of an orbit). The gas drag coefficient C_d is implemented in a size-dependent fashion (BRASSER et al., 2017).

Larger bodies, such as planetary embryos, not only experience gas drag but also have a significant gravitational influence on the surrounding gas. They can gravitationally excite density waves in the disk. The density waves exert torques on the embryo which transfer angular momentum to the disk and force the embryo to migrate inward. These gravitational interactions damp their eccentricities and inclinations (GOLDREICH; TREMAINE, 1980; TANAKA; TAKEUCHI; WARD, 2002; WARD, 1997). The damp of the eccentricity and inclination follows the formalism of Tanaka, Takeuchi and Ward (2002) and Tanaka and Ward (2004), modified by Cresswell and Nelson (2008). The eccentricity damping timescale t_e and the inclination damping timescale t_i are described by:

$$t_e = \frac{t_{wave}}{0.78}\left[1 - 0.14\left(\frac{e}{H/r}\right)^2 + 0.06\left(\frac{e}{H/r}\right)^3 + 0.18\frac{e}{H/r}\left(\frac{i}{H/r}\right)^2\right] \tag{2.7}$$

$$t_i = \frac{t_{wave}}{0.544}\left[1 - 0.30\left(\frac{i}{H/r}\right)^2 + 0.24\left(\frac{i}{H/r}\right)^3 + 0.14\left(\frac{e}{H/r}\right)^2\frac{i}{H/r}\right] \tag{2.8}$$

where

$$t_{wave} = \frac{1}{\Omega_p}\frac{M_*}{m_p}\frac{M_*}{\sum_p a_p^2}\left(\frac{H}{r}\right)^4 \tag{2.9}$$

where H/r is the the local disk aspect ratio, Ω_p is the orbital angular velocity, M_*, a_p, i, e are the solar mass and the embryo's semi-major axis, inclination and eccentricity, respectively. α is the gas disk surface density profile and $\sum_p$ is the local disk surface density. In the code we implement the dumping using accelerations as defined in Cresswell and Nelson (2008)

$$\vec{a}_e = -2\frac{(\vec{v}\cdot\vec{r})\vec{r}}{r^2 t_e} \tag{2.10}$$

$$\vec{a}_i = -2\frac{v_z}{t_i}\vec{k}, \tag{2.11}$$

where k is the unit vector in the z-direction and $\vec{v}$ is the vector velocity.

2.3 GAS DISSIPATED PHASE

Finally, after Jupiter and Saturn accrete the gas and reach their currently mass we dissipate the gas. Then, we start two new set of simulations assuming two possible scenarios: early and late instability. In the early instability, we assume that it happens at 3.5 million years and for the late instability at 100 million years. Fig. 2.6 summarizes all the three steps into one diagram to better show all the parameters and scenarios we explored in this work. In the next sections, we will summarize the main results of this work.

Figure 2.6 – Fluxogram to visualize the numerical setup and the parameters explored in this work.

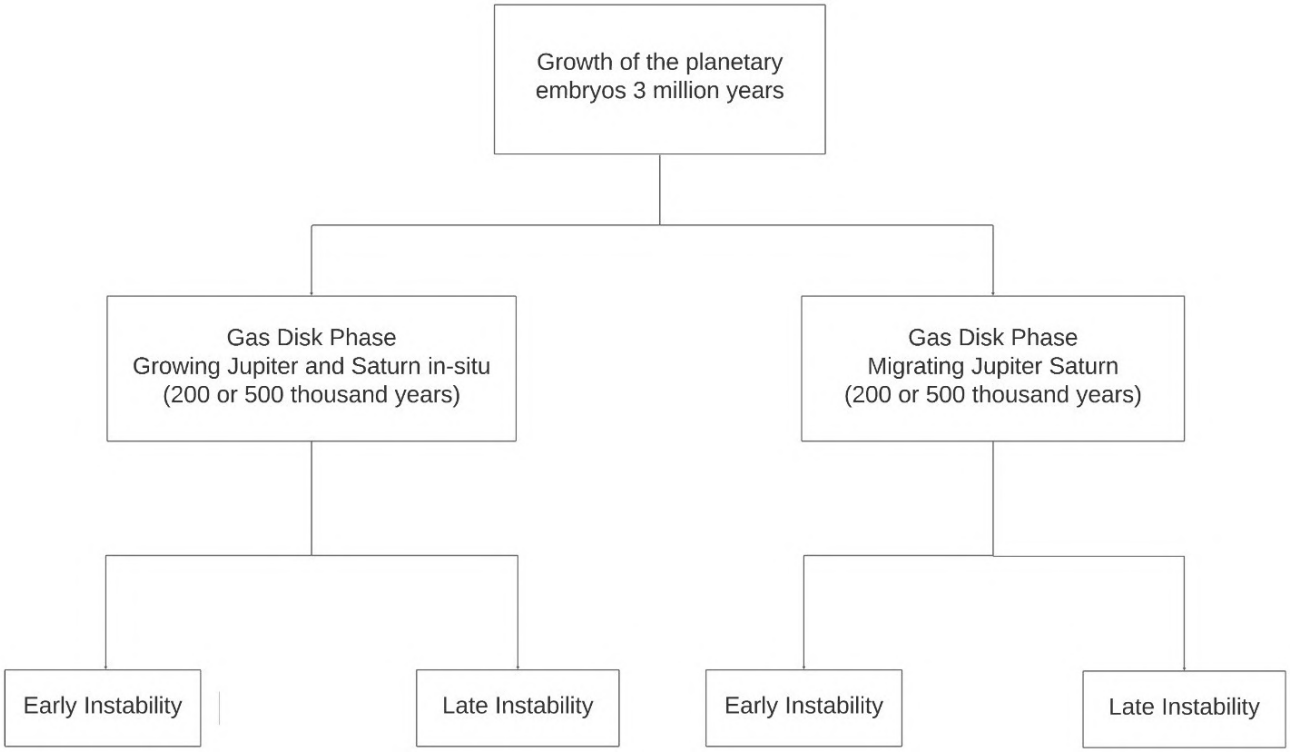

3 NUMERICAL SIMULATIONS

In this chapter, we present the results of our numerical simulations. The first section illustrates how Jupiter and Saturn scatter C-type planetesimals toward the asteroid belt and the forming terrestrial planets, which grow both in situ and migrate inward. Subsequently, we present the systems formed using different setups for Solar System formation.

For each different setup, we performed 20 numerical simulations using a different distribution of embryos in each one. This distribution follows the Safranov regime with a separation of 5-10 r_{Hill}. Our inner ring has 2.5 Earth Mass distributed among approximately 20 embryos and 1500 planetesimals between 0.5 and 1.5 AU. The outer ring consists of 1000 planetesinals distributed from 5 to 20 AU. In this context, we consider the inner ring to be primarily composed of silicate, while the outer ring contains 20% of water in its composition.

3.1 SCATTERING THE C-TYPE PLANETESIMALS

Here, we illustrate how the growth of Jupiter and Saturn can scatter C-type planetesimals from the water zone line in the direction of the asteroid belt and the forming terrestrial planets. We illustrate two different simulations: one involving the growth of Jupiter and Saturn in situ, trapped in the 3:2 MMR, and the other involving the migration of Jupiter from 10 AU and Saturn from 15 AU up to the 3:2 MMR. In both cases, we linearly grow Jupiter over 200 thousand years.

Figures 3.1 and 3.2 illustrate phase 2 of your simulations when Jupiter and Saturn accrete gas from the gaseous disk. Figure 3.1 shows the scenario where the giant planets grow in situ, while Figure 3.2 illustrates the migrating scenario. Blue dots represent C-type planetesimals, red dots represent S-type planetesimals, and black dots represent embryos and giant planets. Embryos and giant planets are considered massive, while planetesimals are considered massless. Both cores starts at 3 Earth masses and linearly grow up to their current mass. Jupiter starts accreting gas at 200 thousand years, continuing up to 400 thousand years. Saturn starts accreting gas after Jupiter reaches its total mass. The gas is dissipated after 500,000 years.

Figures 3.1 and 3.2 show that both mechanisms for growing Jupiter and Saturn are highly effective in scattering C-type planetesimals toward the asteroid belt. Some of these planetesimals may exhibit higher eccentricities and cross the terrestrial planet region. In the final snapshot of each scenario, we observe some of this C-type material crossing the terrestrial region. The ratio of planetesimals scattered in the direction of the asteroid belt and the planet-forming ring will be discussed in Chapters 4 and 5. Following this chapter, we will discuss the radial mass distribution of the planets formed in each different simulation setup.

Figure 3.1 – Snapshots illustrating the planetesimals scattered by the giants planets growing in-situ. Jupiter and Saturn are trapped in the 3:2 MMR. Blue dots represent C-type planetesimals, red dots represent S-type planetesimals, and black dots represent embryos and giant planets. The box-size is a zoom of the internal disk. The snapshots have a total of 500,000 thousand years of numerical simulation.

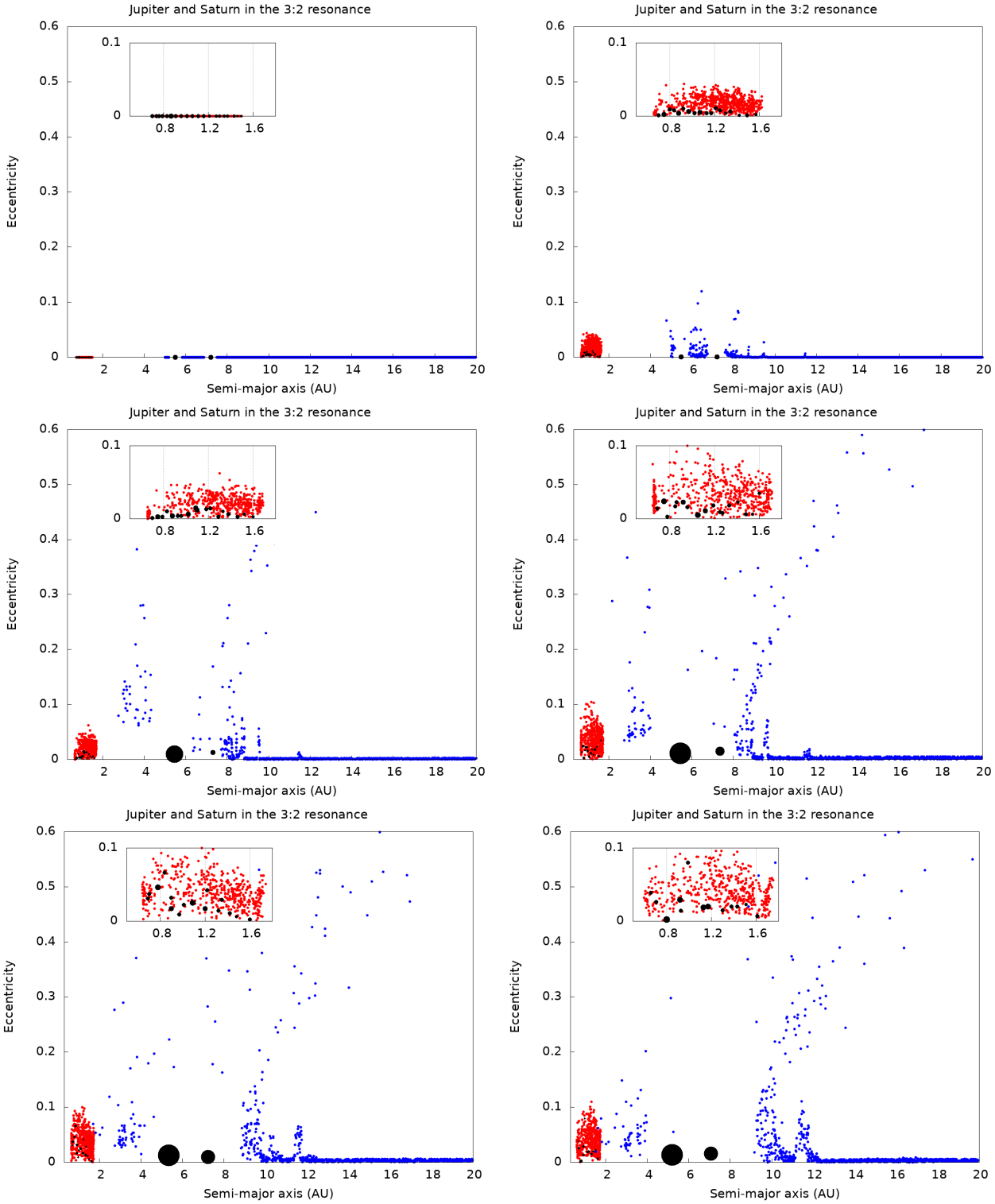

Figure 3.2 – Snapshots illustrating the planetesimals scattered by the migrating giants planets. Jupiter and Saturn migrate inward from 10 and 15 AU up to the 3:2 MMR. Blue dots represent C-type planetesimals, red dots represent S-type planetesimals, and black dots represent embryos and giant planets. The box-size is a zoom of the internal disk. The snapshots have a total of 500,000 thousand years of numerical simulation.

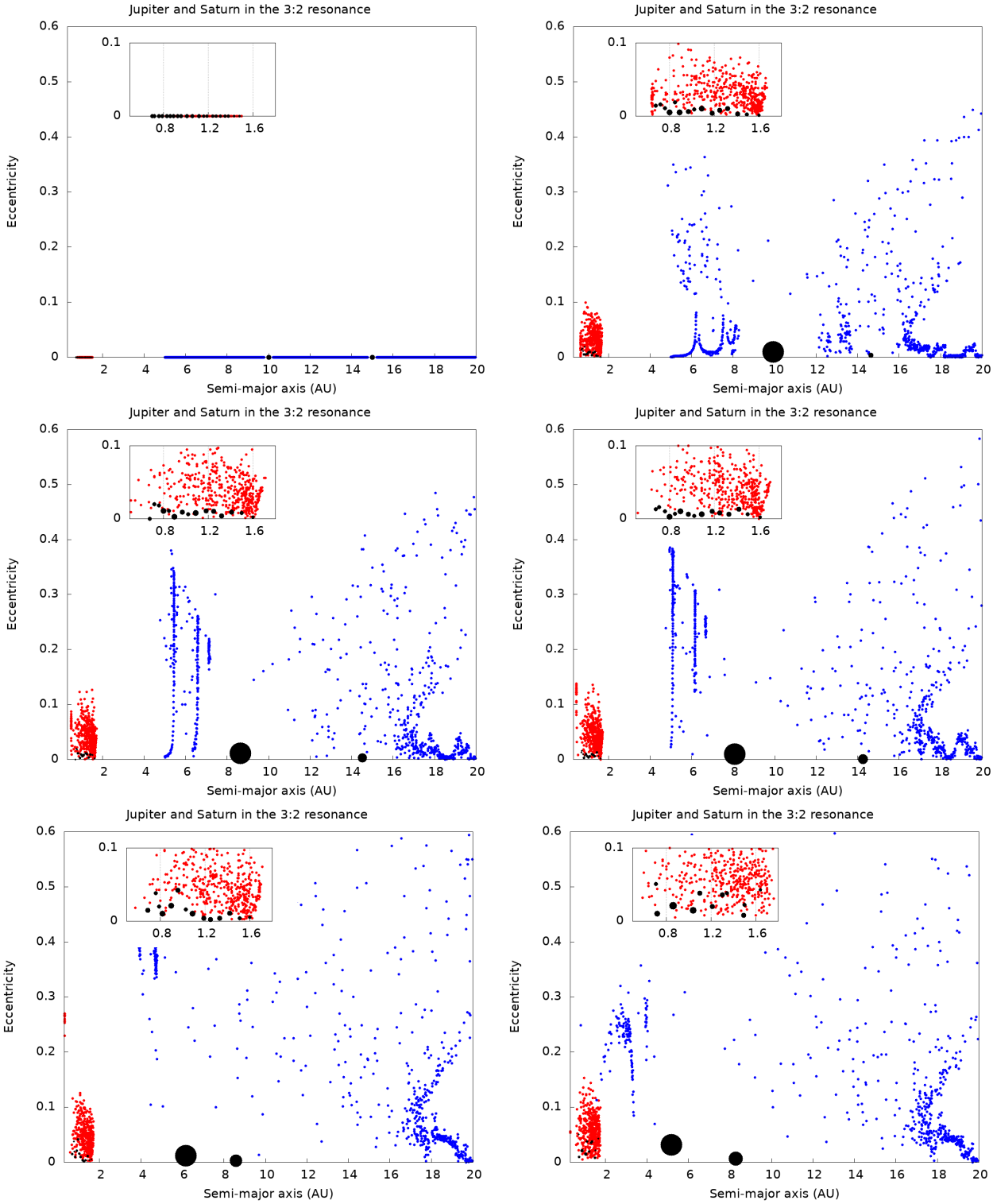

3.2 DISTRIBUTION OF MASS AND SEMI-MAJOR AXIS OF THE SYSTEMS FORMED

Here, we present the semi-major axis and mass distribution obtained from each different numerical setup for the Solar System formation. We illustrate the distribution of the planets formed in the 20 different numerical simulations for each numerical setup. Additionally, we show the total amount of water delivered for each planet. In these analyses, we consider that approximately 10 Earth mass was available in the H_2O zone ring.

Figures 3.3 and 3.4 illustrate the radial mass distribution and the position of the planets formed in each different setup. Figure 3.3 presents the simulations invoking early instability, while Figure 3.4 presents the simulations without invoking early instability. The plots cover four combinations involving the time and the type of the giant planet growth. The upper graphs present the simulations with Jupiter and Saturn growing in situ (fixed in the 3:2 MMR), while the lower graphs present the simulations migrating Jupiter and Saturn from outer orbits to the 3:2 MMR. The left plots show results from simulations where Jupiter and Saturn grow over 200 thousand years, while the right ones show growth over 500 thousand years.

The results show that the mass increases from 0.4 up to 0.8 AU, with a peak of mass around 0.8 AU. Then, the mass starts to decrease again around 1.0 AU. However, in some systems, we still have a Mars analog much more massive than the current mass of Mars in our Solar System. Our initial disk mass distribution follows a radial distribution of mass r^{-1} and extends from 0.5 to 1.5 AU. A possibility to decrease the mass around these positions is to have a more compact disk or using a different slope for the disk, for example, $r^{-3/2}$. We decided not to use a different radial mass distribution to avoid introducing more free parameters and increasing the number of simulations.

Figures 3.3 and 3.4 show that either Jupiter and Saturn growing in situ or migrating inward are very effective at scattering the C-type planetesimals to the terrestrial forming planets. The plots of every system formed in each simulation are presented in B.1. Our results show that we can have a water-rich planet in every position of the terrestrial region, suggesting that every terrestrial planet may have received water-rich planetesimals during its formation and that there is no preferential region for water delivery.

Here, we can conclude that the mechanism of delivering water from the H_2O zone ring during the growth of the giant planets could be the origin of water on Earth. This mechanism is the most plausible explanation for the origin of water on Earth based on isotopic constraints of the Solar System discussed in Section 1.2. In the next chapter, we will discuss about the percentage of planetesimals from the initial distribution that was scattered to the asteroid belt and to the terrestrial planets.

Figure 3.3 – Distribution of mass and semi-major axis of the systems formed invoking the early instability. The analysis covers four combinations involving the time and the type of the giant planet growth. The upper graphs depict scenarios with Jupiter and Saturn growing in situ (fixed in the 3:2 MMR), while the lower graphs represent migrations of Jupiter and Saturn from outer orbits to the 3:2 MMR. The left plots show results from simulations where Jupiter and Saturn grow over 200 thousand years, while the right ones show growth over 500 thousand years.

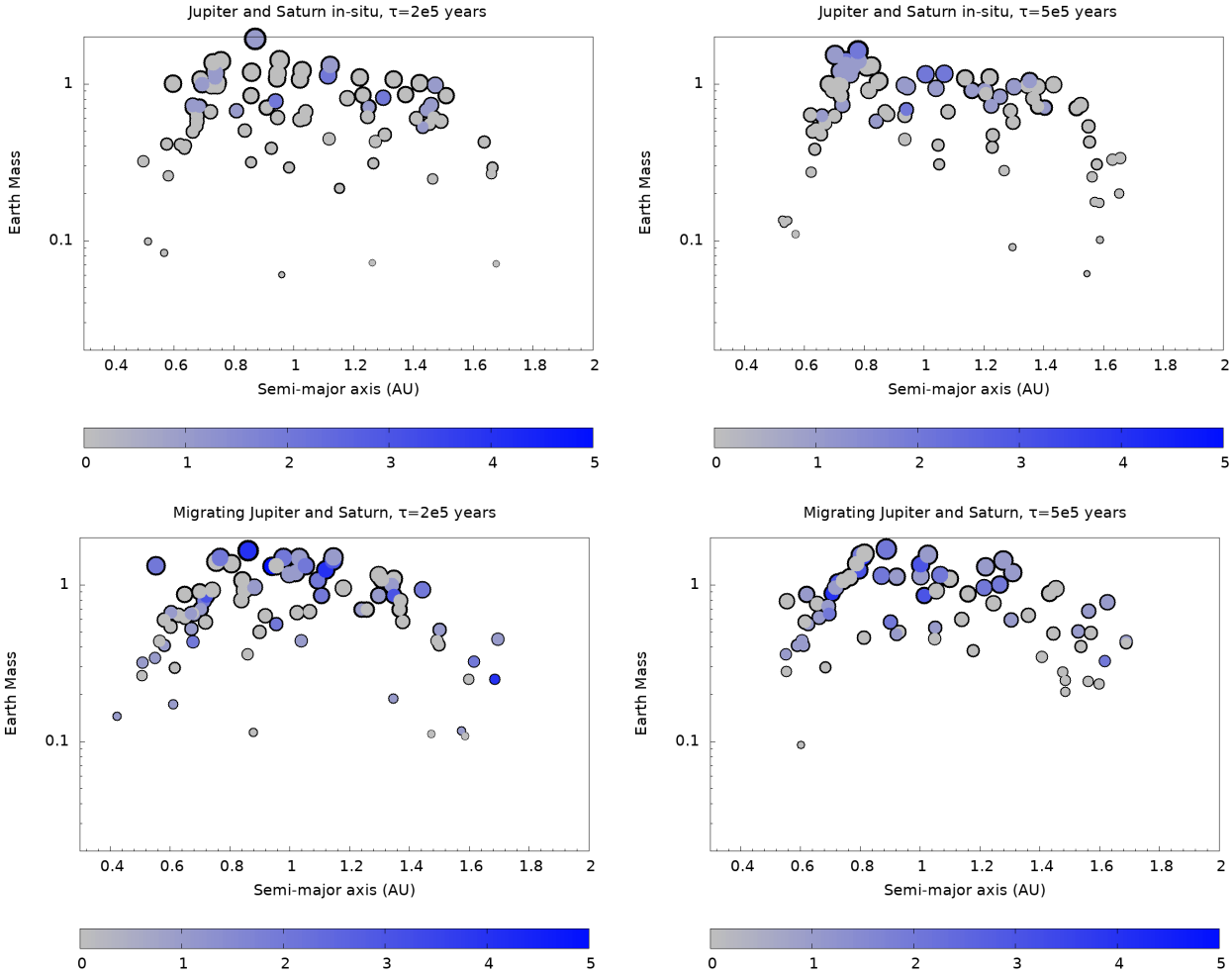

Figure 3.4 – Distribution of mass and semi-major axis of the systems formed without invoking the early instability. The analysis covers four combinations involving the time and the type of the giant planet growth. The upper graphs depict scenarios with Jupiter and Saturn growing in situ (fixed in the 3:2 MMR), while the lower graphs represent migrations of Jupiter and Saturn from outer orbits to the 3:2 MMR. The left plots show results from simulations where Jupiter and Saturn grow over 200 thousand years, while the right ones show growth over 500 thousand years.

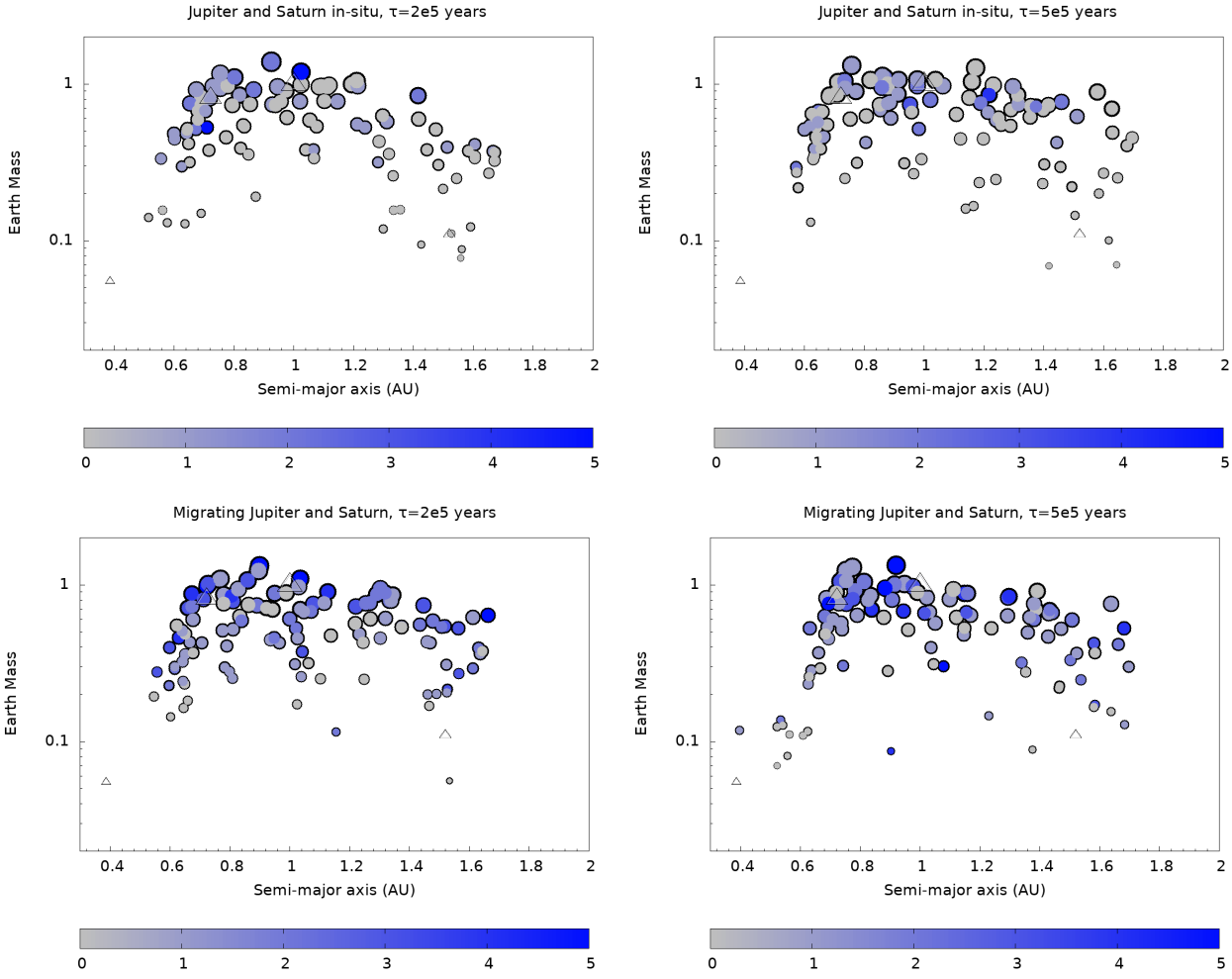

4 ASTEROID BELT

In this chapter, we illustrate the distribution of C and S-type planetesimals scattered to the asteroid belt after 100 million years for each type of setup in the numerical simulations. We compute the planetesimals scattered to the asteroid belt from 20 different simulations for each parameter explored. The goal is to gain a statistical understanding of how each parameter affects the quantity and distribution of C and S-type material in the asteroid belt.

We focus on comparing the amount and distribution of material in the asteroid belt. Here, we are going to analyze the effect of the time for the giant planets grow and the main difference between growing Jupiter and Saturn in situ fixed in the 3:2 MMR and migrating the giant planets from outer orbits up to the resonance. Besides this, we are going to explore the effect of the time for the instability to happen. In the case of early instability, we move the giant planets to their current orbits after 3 million years of simulation, while in the case of late instability, we do not have the instability.

In our work, we have two different mechanisms to scatter the S and C type planetesimals in the direction of the asteroid belt. The S-type material comes from the silicate ring during the growth of the embryos, while the C-type material comes from the water zone ring ring during the growth and evolution of Jupiter and Saturn. During the growth of the planets, they perturb the planetesimal's orbit, generating torque in their orbits and scattering them to other regions of the Solar System. The close encounters with the forming planets give energy to the planetesimals, increasing their eccentricity and inclination.

Here, we must draw attention that the delivery of each type of material occurs at different stages of the Solar System. The delivery of C-type planetesimals happens during the growth of the giant planet, considered to be 200 and 500 thousand years after the embryos' growth. The delivery of S-type materials occurs more slowly as the planetary embryos start to attain enough mass to perturb the inner planetesimals. In this work, we do not account the effect of other forces such as the Yarkovsky effect.

Figs. 4.1 and 4.2 illustrate the distribution of S-type and C-type asteroids delivered to the asteroid belt for different setups of simulations, invoking the early instability and not invoking the early instability, respectively. The y-axis represents the eccentricity, while the x-axis represents the semi-major axis. We limit the inclination of the planetesimals to a maximum of 30 degrees. The gray dots represent the S-type planetesimals, while the blue triangles represent the C-type planetesimals. Here, we consider the S-type as water-poor planetesimals, while the C-type as water-rich planetesimals. In both plots, we are interested in comparing the distribution of these materials within the current distribution of S-type and C-type material in the asteroid belt, which is roughly 50-50.

Figure 4.1 – Distribution of C and S type planetesimals delivered to the asteroid belt under conditions invoking early instability. The analysis covers four combinations involving the time and the type of the giant planet growth. The upper graphs depict scenarios with Jupiter and Saturn growing in situ (fixed in the 3:2 MMR), while the lower graphs represent migrations of Jupiter and Saturn from outer orbits to the 3:2 MMR. The left plots display results from simulations where Jupiter and Saturn grow over 200 thousand years, while the right ones show growth over 500 thousand years.

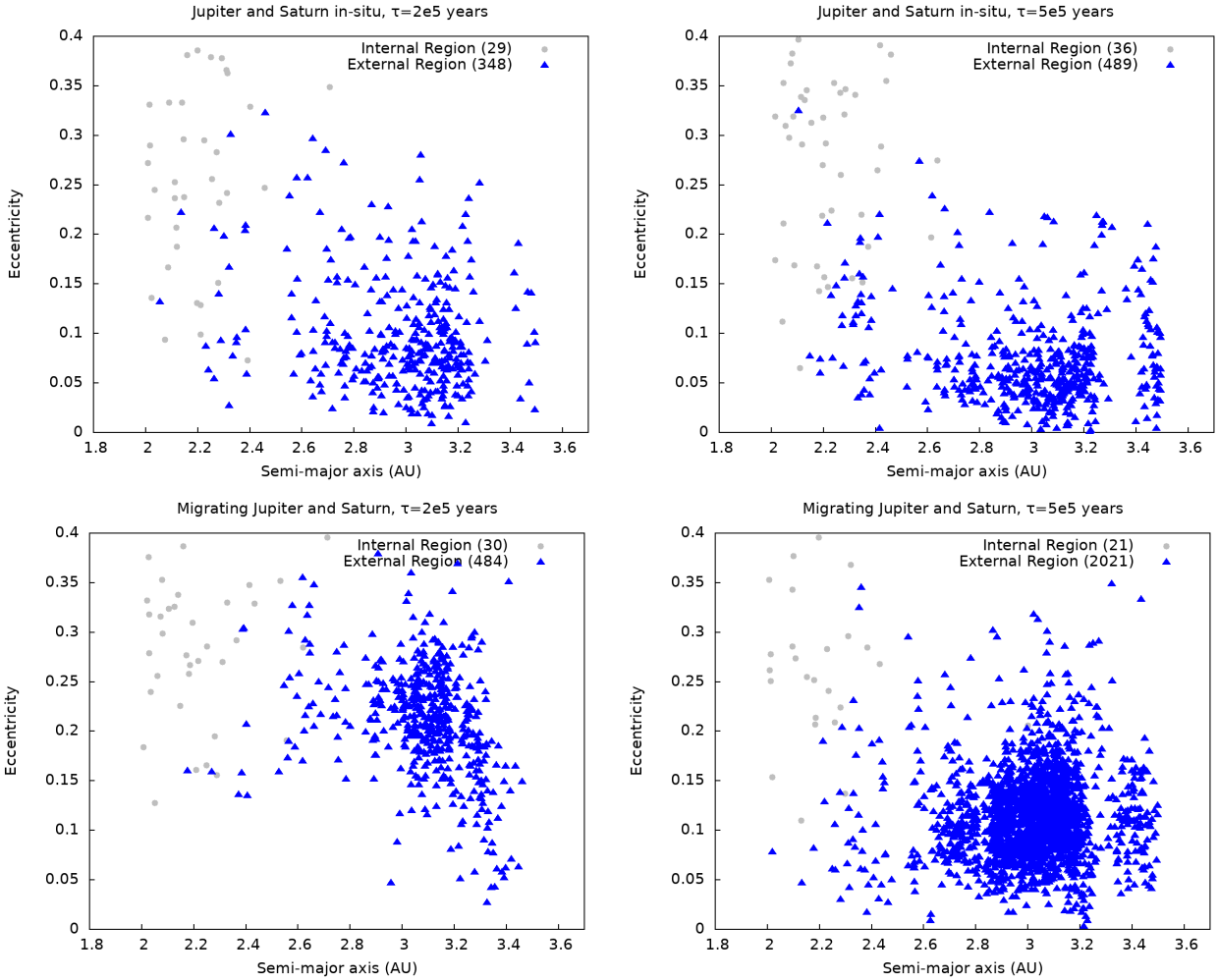

Figure 4.2 – Distribution of C and S type planetesimals delivered to the asteroid belt under conditions without invoking early instability. The analysis covers four combinations involving the time and the type of the giant planet growth. The upper graphs depict scenarios with Jupiter and Saturn growing in situ (fixed in the 3:2 MMR), while the lower graphs represent migrations of Jupiter and Saturn from outer orbits to the 3:2 MMR. The left plots display results from simulations where Jupiter and Saturn grow over 200 thousand years, while the right ones show growth over 500 thousand years.

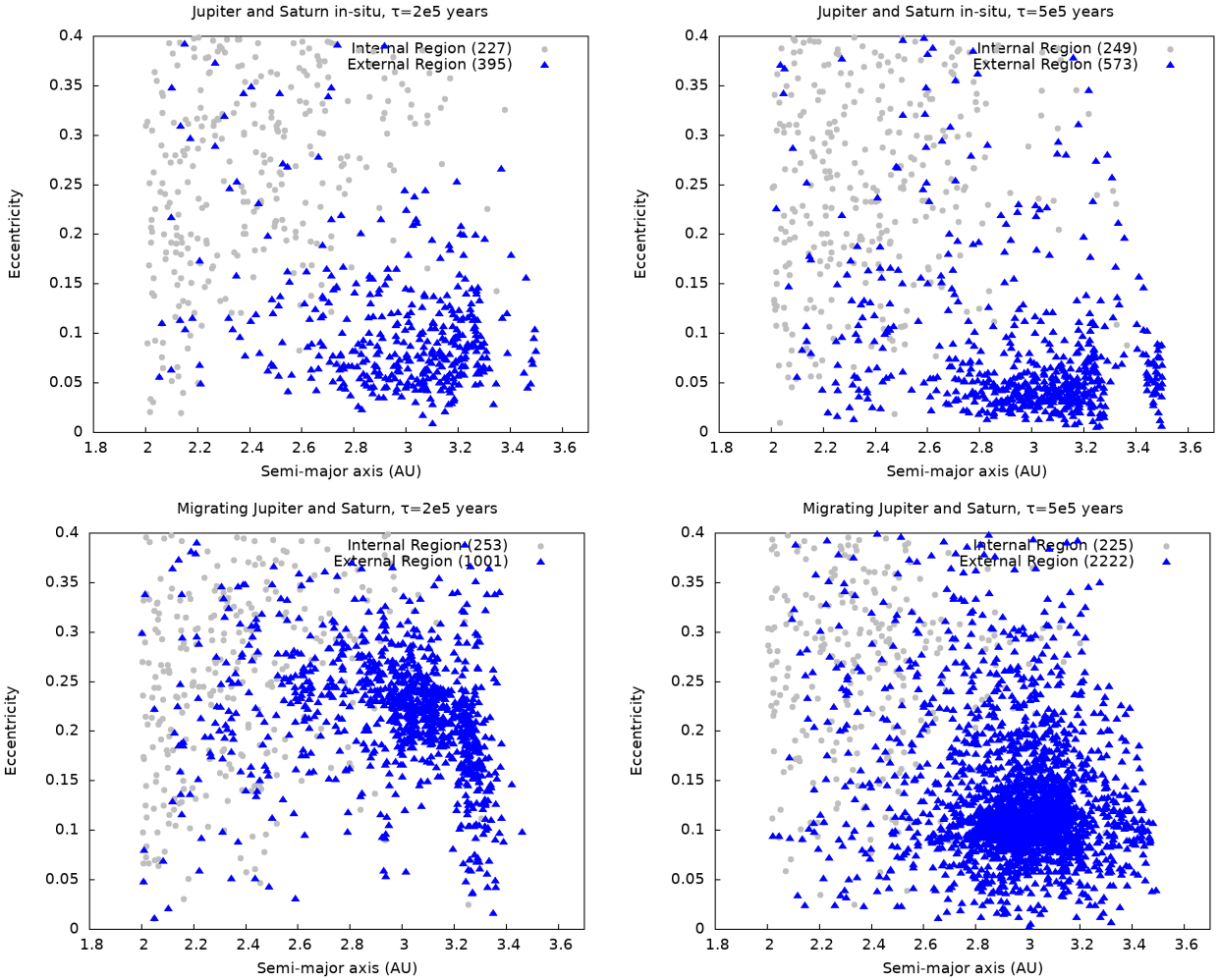

Firstly, we compare the effect of invoking early instability during the formation of the Solar System. Two main points must be observed: the total amount of material and the proportion of C-type and S-type planetesimals scattered to this region. When early instability is invoked, the total amount of S-type material scattered to the asteroid belt is about ten times smaller than when early instability is not considered. We believe that this occurs because early instability perturbs the embryos located in the inner ring, causing them to collide with the planetesimals much faster than when early instability is not invoked. On the other hand, the amount of C-type planetesimals does not undergo a significant difference when early instability is invoked.

As a consequence, it becomes challenging to match the 50-50 proportion of C-type and S-type material in the asteroid belt when early instability is invoked. These results indicate that when using the planet formation with ring distribution, there is a preference of using late instability rather than invoking early instability to match the current distribution of the asteroid belt. A possible solution for the case of invoking early instability is using a much less massive H_2O zone ring than the silicate ring. Another possible solution is the mass ablation that was not taking into account in this work. The mass ablation shrink in size the water rich asteroids, but do not affect the silicate and enstatite asteroids (SOUSA et al., 2024).

Now, we will analyze the effect of time and the type of growth of the giant planets. We explored the time for Jupiter and Saturn to grow to 200 or 500 thousand years, considering Jupiter and Saturn growing in situ or migrating inward from outer orbits. Figures 4.1 and 4.2 show that when Jupiter and Saturn grow faster, the eccentricity of the C-type planetesimals is typically higher than when it occurs at 500 thousand years. On the other hand, when the giant planets grow slowly, they deliver more C-type material to the asteroid belt.

When Jupiter and Saturn migrate inward, they perturb the H_2O zone ring more, delivering up to 5 times more C-type material than Jupiter and Saturn growing in situ, depending on the simulation setup. The delivery of S-type material is not strongly affected by either the time for growing the giant planets or the type of formation, whether forming in situ or migrating. This is because the delivery of S-type materials depends only on the formation of terrestrial planets.

In the next section, we will discuss the delivery of water to the terrestrial planets. Some of these scattered C-type planetesimals can cross the terrestrial planets' region and may collide with the forming planets. Subsequently, we will quantify the total amount of this material that crosses the terrestrial planets. We will also illustrates snapshots of one simulation using the formation Jupiter and Saturn in-situ and migrating the giant planets.

5 WATER DELIVERY TO THE TERRESTRIAL PLANETS

Here, we will summarize the percentage of C-type material that was scattered and impacted with the forming terrestrial planets, while also discussing the percentage of C and S-type material from the initial disk distribution that was scattered to the asteroid belt.

Figure 5.1 illustrates the average percentage of C-type material that collided with each of the analog planets formed in our simulations. We averaged the delivery to each analog over 20 simulations with the same initial numerical setup for the formation of giant planets. We divide the analyses into simulations invoking early instability and those without invoking it. Consistently, when Jupiter and Saturn grow faster, they scatter more planetesimals that cross the Mars's orbit, colliding with the forming terrestrial planets. It happens because the gas dissipates faster and does not decrease the eccentricity and inclination of these planetesimals.

Figure 5.1 also shows that when early instability is invoked, about 0.2% of the initial H_2O zone ring material collided with Venus and Earth analogs at about the same proportion. On the other hand, when early instability is not invoked, Earth analogs received consistently more C-type material than Venus analogs. Mars received C-type material only when migration was invoked. The plots show that no water was delivered to a Mercury's analog. This is because we do not have enough resolution to produce Mercury in our simulations.

Figure 5.2 illustrates the average percentage of C-type and S-type planetesimals that were scattered in the direction of the asteroid belt during the growth of the terrestrial and giant planets. We averaged the C and S-type material scattered in 20 simulations with the same initial numerical setup for the formation of giant planets. The plots show the minimum, the average, and the maximum percentage of material that was scattered to the asteroid belt for each different setup.

Figure 5.2 shows that when early instability is invoked, it is challenging to maintain the same proportion of S and C-type material in the asteroid belt independently of the numerical setup for the formation of the giant planets. In the case of late instability, we observe an overlap of the distribution when Jupiter and Saturn grow faster over 200 thousand years. When Jupiter and Saturn grow in 500 thousand years, the gas dissipates later, scattering more C-type material to the asteroid belt.

Here, we find that on average, 1-10% of the H_2O zone ring distribution was scattered to the asteroid belt depending on the initial conditions. Our H_2O zone ring extends from 5-20 AU, but in fact, only the material from 5-10 AU is scattered in the direction of the asteroid belt and the forming terrestrial planets. The outer C-type material is scattered to orbits beyond Jupiter and Saturn. The main point of this work is to determine the amount of C-type material that may exist in the H_2O zone ring to deliver the necessary amount of water to Earth, while also avoiding placing a significant amount of C-type material in the asteroid belt. We must achieve a balance between these two deliveries. In the next chapter, we will summarize our main results and discuss our future steps.

Figure 5.1 – The average percentage of C-type material that collided with each of the analog planets formed in our simulations. We averaged the delivery to each analog over 20 simulations with the same initial numerical setup for the formation of giant planets.

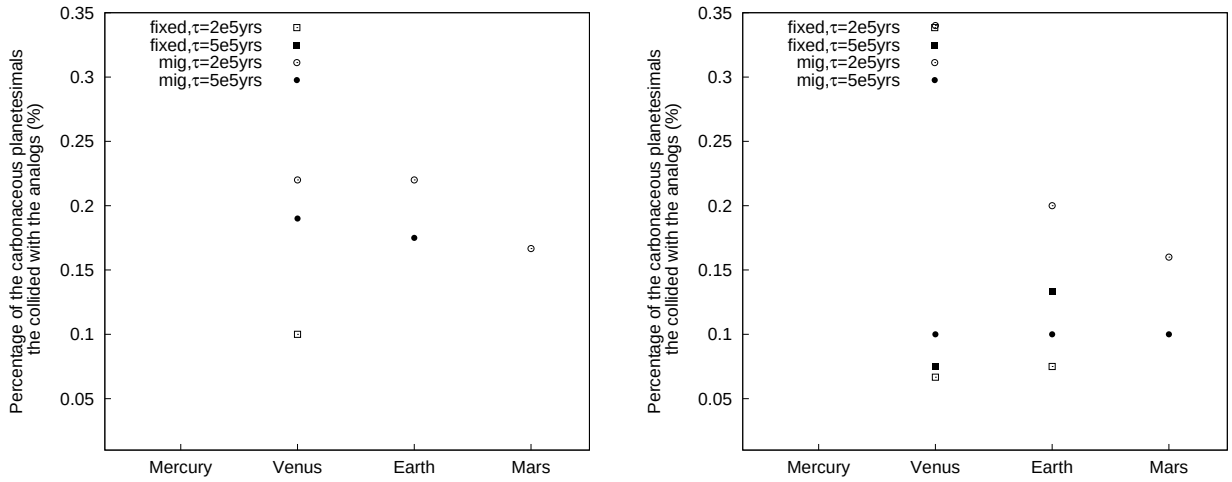

Figure 5.2 – The average percentage of C-type and S-type planetesimals that were scattered in the direction of the asteroid belt during the growth of the terrestrial and giant planets. We averaged the C and S-type material scattered in 20 simulations with the same initial numerical setup for the formation of giant planets.

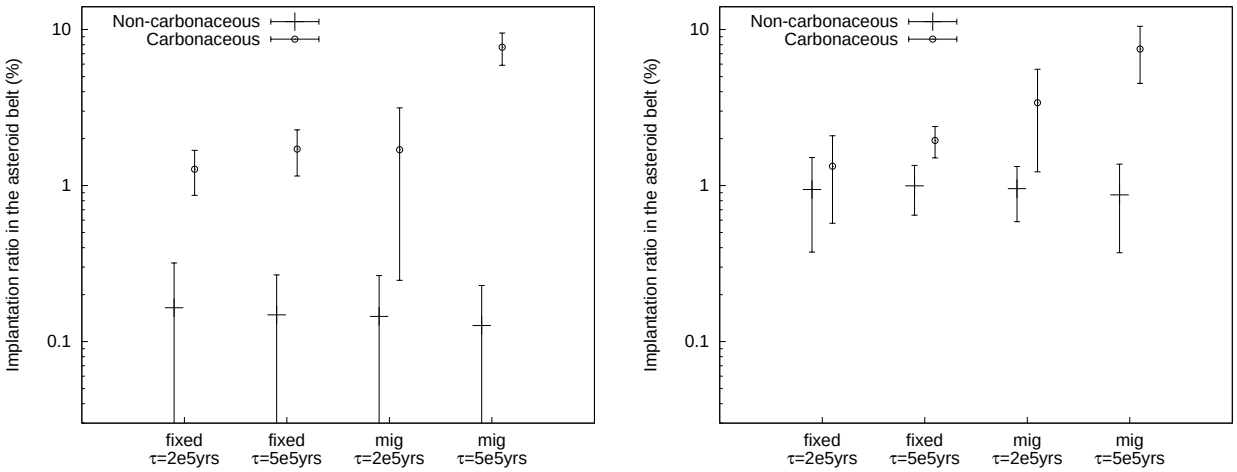

6 FINAL CONSIDERATIONS AND FUTURE STEPS

There is an ongoing debate about the origin of water in the terrestrial planets. Evidence from Earth's water D/H ratio suggests that one of the main sources of Earth's water may have been carbonaceous chondrites' parent bodies. Our simulations simultaneously model the growth and/or migration of Jupiter and Saturn and the accretion of terrestrial planets.

Two scenarios for the growth of Jupiter and Saturn were explored. In the first one, we assume that Jupiter and Saturn formed nearly in situ. In the second one, we take that Jupiter and Saturn migrated inwards as they were growing during the gas disk phase. Planetesimals were distributed into two rings. The so-called "inner ring" was assumed to contain water-poor planetesimals distributed from 0.5 to 1.5 AU. The so-called outer ring contained water-rich planetesimals distributed from 5 to 20 AU.

We mimic the runaway gas accretion phase of the giant planets Jupiter and Saturn starting from cores of 3 Earth masses. Planetary embryos in the inner ring start with their masses between those of the Moon and Mars. Our simulations were integrated using a modified version of the Symba integrator for 100 million years. Our results indicate that the growth and migration of Jupiter and Saturn can deliver about 0.1-1% of water-rich material originally from the outer ring into the terrestrial region, depending on model-assumed parameters.

Our simulations where Jupiter and Saturn formed nearly in situ can naturally deliver water to Earth and explain the currently observed fractions between C and S-type asteroids in the belt. On the other hand, the simulations, where Jupiter and Saturn migrated from distant regions, deliver all of Earth's water but tend to implant relatively larger fractions of water-rich planetesimals into the belt than the observed ones, making this scenario potentially inconsistent with the current asteroid belt. This contrast become more evident when we invoke early instability which decreases the amount of S-type planetesimals in the asteroid belt.

Our results suggest that Jupiter and Saturn experienced very limited radial migration during the sun's natal disk phase, or the total mass in water-rich planetesimals in the giant planet region was significantly lower than considered in our work. This later scenario may require that Earth's water have more sources to be consistent with the amount of water observed on Earth.

The paper of the part II of this thesis is in final preparation and should be submitted to Icarus review. As a future work we aim to include the mass ablation to better estimate the mass of the C-type planetesimals in the asteroid belt. Another possibility is to expand this work to Solar Systems analogs and exoplanets to understand if this mechanism still works when we have other configurations of terrestrial planets and giant planets.

REFERENCES

ADACHI, I.; HAYASHI, C.; NAKAZAWA, K. The gas drag effect on the elliptic motion of a solid body in the primordial solar nebula. **Progress of Theoretical Physics**, Oxford University Press, v. 56, n. 6, p. 1756–1771, 1976.

AMELIN, Y. et al. Lead isotopic ages of chondrules and calcium-aluminum-rich inclusions. **Science**, American Association for the Advancement of Science, v. 297, n. 5587, p. 1678–1683, 2002.

ARAUJO, N. C. S.; NETO, E. V.; FORYTA, D. W. Formation of the g-ring arc. **Monthly Notices of the Royal Astronomical Society**, v. 461, p. 1868–1874, 2016.

Bitsch; Lambrechts, Michiel; Johansen, Anders. The growth of planets by pebble accretion in evolving protoplanetary discs. **A&A**, v. 582, p. A112, 2015. Available from Internet:<https://doi.org/10.1051/0004-6361/201526463>.

BOCKELÉE-MORVAN, D. et al. Cometary isotopic measurements. **Space science reviews**, Springer, v. 197, p. 47–83, 2015.

BRASSER, R. et al. The cool and distant formation of mars. **Earth and Planetary Science Letters**, Elsevier, v. 468, p. 85–93, 2017.

BURBINE, T. H. et al. Meteoritic parent bodies: Their number and identification. **Asteroids III**, University of Arizona Press, 2002.

BURGER, C.; MAINDL, T. I.; SCHäFER, C. M. Transfer, loss and physical processing of water in hit-and-run collisions of planetary embryos. **Celestial Mechanics and Dynamical Astronomy**, Springer Science and Business Media LLC, v. 130, n. 1, dec 2017.

BUZZATTO, P.; SFAIR, R.; SCHäFER, C. M. **SPH analysis of collisions between macroscopic bodies immersed in planetary rings**. Thesis (Ph.D. thesis) — São Paulo State University, in prep.

Callegari Jr, N.; RODRÍGUEZ, A. The orbit of aegaeon and the 7:6 mimas-aegaeon resonance. **Celestial Mechanics and Dynamical Astronomy**, Springer, v. 135, n. 2, p. 21, 2023.

CHAMBERS, J. A semi-analytic model for oligarchic growth. **Icarus**, Elsevier, v. 180, n. 2, p. 496–513, 2006.

CHAMBERS, J.; CASSEN, P. The effects of nebula surface density profile and giant-planet eccentricities on planetary accretion in the inner solar system. **Meteoritics & Planetary Science**, Wiley Online Library, v. 37, n. 11, p. 1523–1540, 2002.

CHAMBERS, J.; WETHERILL, G. Making the terrestrial planets: N-body integrations of planetary embryos in three dimensions. **Icarus**, v. 136, n. 2, p. 304–327, 1998. ISSN 0019-1035. Available from Internet:<https://www.sciencedirect.com/science/article/pii/S0019103598960079>.

CHAMBERS, J.; WETHERILL, G. Making the terrestrial planets: N-body integrations of planetary embryos in three dimensions. **Icarus**, Elsevier, v. 136, n. 2, p. 304–327, 1998.

CHAMBERS, J.; WETHERILL, G. Planets in the asteroid belt. **Meteoritics & Planetary Science**, Wiley Online Library, v. 36, n. 3, p. 381–399, 2001.

CHAMBERS, J. E. Making more terrestrial planets. **Icarus**, Elsevier, v. 152, n. 2, p. 205–224, 2001.

CLEMENT, M. S. et al. Mars' growth stunted by an early giant planet instability. **Icarus**, Elsevier, v. 311, p. 340–356, 2018.

CLEMENT, M. S. et al. The early instability scenario: Terrestrial planet formation during the giant planet instability, and the effect of collisional fragmentation. **Icarus**, Elsevier, v. 321, p. 778–790, 2019.

CRESSWELL, P.; NELSON, R. P. Three-dimensional simulations of multiple protoplanets embedded in a protostellar disc. **Astronomy & Astrophysics**, EDP Sciences, v. 482, n. 2, p. 677–690, 2008.

CRIDA, A.; MORBIDELLI, A.; MASSET, F. On the width and shape of gaps in protoplanetary disks. **Icarus**, Elsevier, v. 181, n. 2, p. 587–604, 2006.

DEIENNO, R. et al. Implications of jupiter inward gas-driven migration for the inner solar system. **The Astrophysical Journal Letters**, IOP Publishing, v. 936, n. 2, p. L24, 2022.

DUNCAN, M. J.; LEVISON, H. F.; LEE, M. H. A multiple time step symplectic algorithm for integrating close encounters. **The Astronomical Journal**, IOP Publishing, v. 116, n. 4, p. 2067, 1998.

GOLDREICH, P.; TREMAINE, S. Disk-satellite interactions. **Astrophysical Journal**, American Astronomical Society, v. 241, n. 1, p. 425–441, 1980.

GOMES, R. et al. Origin of the cataclysmic late heavy bombardment period of the terrestrial planets. **Nature**, Nature Publishing Group UK London, v. 435, n. 7041, p. 466–469, 2005.

GREENBERG, R. et al. Planetesimals to planets: Numerical simulation of collisional evolution. **Icarus**, Elsevier, v. 35, n. 1, p. 1–26, 1978.

HALLIDAY, A. N.; KLEINE, T. Meteorites and the timing, mechanisms, and conditions of terrestrial planet accretion and early differentiation. **Meteorites and the early solar system II**, p. 775, 2006.

HANSEN, B. M. Formation of the terrestrial planets from a narrow annulus. **The Astrophysical Journal**, IOP Publishing, v. 703, n. 1, p. 1131, 2009.

HARTMANN, W. K.; DAVIS, D. R. Satellite-sized planetesimals and lunar origin. **Icarus**, Elsevier, v. 24, n. 4, p. 504–515, 1975.

HEDMAN, M. et al. The source of saturn's g ring. **Science**, v. 317, n. 5838, p. 653–656, 2007.

HEDMAN, M. et al. Aegaeon (saturn liii), a g-ring object. **Icarus**, v. 207, p. 433–447, 2010.

HUANG, J. et al. Co and dust properties in the tw hya disk from high-resolution alma observations. **The Astrophysical Journal**, IOP Publishing, v. 852, n. 2, p. 122, 2018.

IZIDORO, A.; BITSCH, B.; DASGUPTA, R. The effect of a strong pressure bump in the sun's natal disk: terrestrial planet formation via planetesimal accretion rather than pebble accretion. **The Astrophysical Journal**, IOP Publishing, v. 915, n. 1, p. 62, 2021.

IZIDORO, A. et al. Planetesimal rings as the cause of the solar system's planetary architecture. **Nature Astronomy**, Nature Publishing Group, v. 6, n. 3, p. 357–366, 2022.

IZIDORO, A. et al. Terrestrial planet formation in a protoplanetary disk with a local mass depletion: A successful scenario for the formation of mars. **The Astrophysical Journal**, American Astronomical Society, v. 782, n. 1, p. 31, jan 2014.

IZIDORO, A.; PIANI, L. Origin of water in the terrestrial planets: insights from meteorite data and planet formation models. **Elements: An International Magazine of Mineralogy, Geochemistry, and Petrology**, Mineralogical Society of America, v. 18, n. 3, p. 181–186, 2022.

IZIDORO, A. et al. Terrestrial planet formation constrained by mars and the structure of the asteroid belt. **Monthly Notices of the Royal Astronomical Society**, Oxford University Press, v. 453, n. 4, p. 3619–3634, 2015.

IZIDORO, A. et al. A compound model for the origin of earth's water. **The Astrophysical Journal**, IOP Publishing, v. 767, n. 1, p. 54, 2013.

JACOBSON, S. A.; MORBIDELLI, A. Lunar and terrestrial planet formation in the grand tack scenario. **Philosophical Transactions of the Royal Society A: Mathematical, Physical and Engineering Sciences**, The Royal Society Publishing, v. 372, n. 2024, p. 20130174, 2014.

JACOBSON, S. A. et al. Highly siderophile elements in earth's mantle as a clock for the moon-forming impact. **Nature**, Nature Publishing Group UK London, v. 508, n. 7494, p. 84–87, 2014.

JOHANSEN, A. et al. The multifaceted planetesimal formation process. **arXiv preprint arXiv:1402.1344**, 2014.

JOHANSEN, A. et al. A pebble accretion model for the formation of the terrestrial planets in the solar system. **Science Advances**, v. 7, n. 8, p. eabc0444, 2021. Available from Internet:<https://www.science.org/doi/abs/10.1126/sciadv.abc0444>.

KATAOKA, A. et al. Fluffy dust forms icy planetesimals by static compression. **Astronomy & Astrophysics**, EDP Sciences, v. 557, p. L4, 2013.

KLEINE, T. et al. The non-carbonaceous–carbonaceous meteorite dichotomy. **Space Science Reviews**, Springer, v. 216, p. 1–27, 2020.

KLEINE, T. et al. Hf–w chronology of the accretion and early evolution of asteroids and terrestrial planets. **Geochimica et Cosmochimica Acta**, Elsevier, v. 73, n. 17, p. 5150–5188, 2009.

KOKUBO, E.; IDA, S. Formation of protoplanets from planetesimals in the solar nebula. **Icarus**, Elsevier, v. 143, n. 1, p. 15–27, 2000.

LATTARI, V. C. Formação de pequenos satélites e anéis de poeira. Universidade Estadual Paulista (Unesp), 2019.

LEVISON, H. F.; DUNCAN, M. J. The long-term dynamical behavior of short-period comets. **Icarus**, Elsevier, v. 108, n. 1, p. 18–36, 1994.

LEVISON, H. F. et al. Growing the terrestrial planets from the gradual accumulation of submeter-sized objects. **Proceedings of the National Academy of Sciences**, National Acad Sciences, v. 112, n. 46, p. 14180–14185, 2015.

LIN, D. N.; PAPALOIZOU, J. On the tidal interaction between protoplanets and the protoplanetary disk. iii-orbital migration of protoplanets. **Astrophysical Journal, Part 1 (ISSN 0004-637X), vol. 309, Oct. 15, 1986, p. 846-857.**, v. 309, p. 846–857, 1986.

MADEIRA, G. et al. Production and fate of the g ring arc particles due to aegaeon (saturn liii). **Monthly Notices of the Royal Astronomical Society**, v. 475, p. 5474–5479, 2018.

MANARA, C. F.; MORBIDELLI, A.; GUILLOT, T. Why do protoplanetary disks appear not massive enough to form the known exoplanet population? **Astronomy & Astrophysics**, EDP Sciences, v. 618, p. L3, 2018.

MARTY, B. et al. Origins of volatile elements (h, c, n, noble gases) on earth and mars in light of recent results from the rosetta cometary mission. **Earth and Planetary Science Letters**, v. 441, p. 91–102, 2016. ISSN 0012-821X. Available from Internet:<https://www.sciencedirect.com/science/article/pii/S0012821X16300486>.

MASSET, F.; SNELLGROVE, M. Reversing type ii migration: resonance trapping of a lighter giant protoplanet. **Monthly Notices of the Royal Astronomical Society**, Blackwell Science Ltd Oxford, UK, v. 320, n. 4, p. L55–L59, 2001.

MORBIDELLI, A. et al. Source regions and timescales for the delivery of water to the earth. **Meteoritics & Planetary Science**, Wiley Online Library, v. 35, n. 6, p. 1309–1320, 2000.

MORBIDELLI, A.; CRIDA, A. The dynamics of jupiter and saturn in the gaseous protoplanetary disk. **icarus**, Elsevier, v. 191, n. 1, p. 158–171, 2007.

MORBIDELLI, A. et al. Chaotic capture of jupiter's trojan asteroids in the early solar system. **Nature**, Nature Publishing Group UK London, v. 435, n. 7041, p. 462–465, 2005.

NAMOUNI, F.; PORCO, C. The confinement of neptune's ring arcs by the moon galatea. **Nature**, v. 417, p. 45–7, 2002.

NESVORNÝ, D. Evidence for slow migration of neptune from the inclination distribution of kuiper belt objects. **The Astronomical Journal**, IOP Publishing, v. 150, n. 3, p. 73, 2015.

NESVORNÝ, D.; MORBIDELLI, A. Statistical study of the early solar system's instability with four, five, and six giant planets. **The Astronomical Journal**, IOP Publishing, v. 144, n. 4, p. 117, 2012.

NESVORNÝ, D.; VOKROUHLICKÝ, D.; MORBIDELLI, A. Capture of trojans by jumping jupiter. **The Astrophysical Journal**, IOP Publishing, v. 768, n. 1, p. 45, 2013.

PIANI, L. et al. Origin of hydrogen isotopic variations in chondritic water and organics. **Earth and Planetary Science Letters**, Elsevier, v. 567, p. 117008, 2021.

PORCO, C. An explanation for neptune's ring arcs. **Science**, v. 253, n. 5023, p. 995–1001, 1991.

PORCO, C. on behalf of the cassini imaging team 2009. s/2008 s1. **IAU Circ**, v. 9023, 2009.

RAYMOND, S. N.; IZIDORO, A. The empty primordial asteroid belt. **Science advances**, American Association for the Advancement of Science, v. 3, n. 9, p. e1701138, 2017.

RAYMOND, S. N.; IZIDORO, A. Origin of water in the inner solar system: Planetesimals scattered inward during jupiter and saturn's rapid gas accretion. **Icarus**, Elsevier, v. 297, p. 134–148, 2017.

RAYMOND, S. N.; MORBIDELLI, A. Planet formation: key mechanisms and global models. **Demographics of Exoplanetary Systems: Lecture Notes of the 3rd Advanced School on Exoplanetary Science**, Springer, p. 3–82, 2022.

RAYMOND, S. N. et al. Building the terrestrial planets: Constrained accretion in the inner solar system. **Icarus**, Elsevier, v. 203, n. 2, p. 644–662, 2009.

RAYMOND, S. N.; QUINN, T.; LUNINE, J. I. High-resolution simulations of the final assembly of earth-like planets i. terrestrial accretion and dynamics. **Icarus**, Elsevier, v. 183, n. 2, p. 265–282, 2006.

REIN, H.; SPIEGEL, D. S. Ias15: a fast, adaptive, high-order integrator for gravitational dynamics, accurate to machine precision over a billion orbits. **Monthly Notices of the Royal Astronomical Society**, v. 446, p. 1424–1437, 2015.

RIBEIRO, R. de S. et al. Dynamical evidence for an early giant planet instability. **Icarus**, Elsevier, v. 339, p. 113605, 2020.

SAFRONOV, V. S. **Evolution of the Protoplanetary Cloud and Formation of the Earth and the Planets**. [S.l.]: Israel Program for Scientific Translations, 1972.

SCHÄFER, C. M. et al. A versatile smoothed particle hydrodynamics code for graphic cards. **Astronomy and Computing**, Elsevier, v. 33, p. 100410, 2020.

SOUSA, R. R. de et al. Asteroids were born bigger: An implication of surface mass ablation during gas-assisted implantation into the asteroid belt. **Icarus**, Elsevier, v. 410, p. 115910, 2024.

TANAKA, H.; TAKEUCHI, T.; WARD, W. R. Three-dimensional interaction between a planet and an isothermal gaseous disk. i. corotation and lindblad torques and planet migration. **The Astrophysical Journal**, IOP Publishing, v. 565, n. 2, p. 1257, 2002.

TANAKA, H.; WARD, W. R. Three-dimensional interaction between a planet and an isothermal gaseous disk. ii. eccentricity waves and bending waves. **The Astrophysical Journal**, IOP Publishing, v. 602, n. 1, p. 388, 2004.

TSIGANIS, K. et al. Origin of the orbital architecture of the giant planets of the solar system. **Nature**, Nature Publishing Group UK London, v. 435, n. 7041, p. 459–461, 2005.

WALSH, K. J. et al. A low mass for mars from jupiter's early gas-driven migration. **Nature**, Nature Publishing Group, v. 475, n. 7355, p. 206–209, 2011.

WARD, W. R. Protoplanet migration by nebula tides. **Icarus**, Elsevier, v. 126, n. 2, p. 261–281, 1997.

WARREN, P. H. Stable-isotopic anomalies and the accretionary assemblage of the earth and mars: A subordinate role for carbonaceous chondrites. **Earth and Planetary Science Letters**, Elsevier, v. 311, n. 1-2, p. 93–100, 2011.

WETHERILL, G. W. An alternative model for the formation of the asteroids. **Icarus**, Elsevier, v. 100, n. 2, p. 307–325, 1992.

APPENDIX A – DUST PRODUCTION IN THE G-RING ARC PAPER

PHILOSOPHICAL TRANSACTIONS A

royalsocietypublishing.org/journal/rsta

Research

Check for updates

Article submitted to journal

Subject Areas:
astronomy, planetary rings

Keywords:
G-ring, Aegaeon, dust, numerical simulation

Author for correspondence:
V. Lattari
e-mail: victor.lattari@unesp.br

Dust production in the G-ring arc

V. Lattari[1], R. Sfair[1, 2], P. B. Siqueira[1], and C. M. Schäfer[2]

[1]victor.lattari@unesp.br
[2]rafael.sfair@unesp.br
[3]patricia.buzzatto@unesp.br
[4]ch.schaefer@uni-tuebingen.de

The G-ring arc of Saturn, confined by the 7:6 corotation eccentric resonance with Mimas, is primarily composed of micrometric particles. These particles, significantly influenced by solar radiation pressure, are subject to rapid depletion. This study investigates a mechanism for dust replenishment in the arc, specifically analyzing collisions between macroscopic bodies and the satellite Aegaeon. Utilizing N-body and SPH simulations, we assess the dust generation from these impacts, with a focus on the most likely collision parameters derived from the N-body simulations. Our findings indicate that while collisions among macroscopic bodies are inefficient for dust production, impacts involving Aegaeon are substantially more effective. This mechanism, in conjunction with the natural decay processes and continuous dust generation from impacts, potentially keeps the arc population over thousands of years with a possible variation in brightness.

1. Introduction

In early 2004, the Cassini spacecraft identified two tenuous rings in eccentric resonances with Saturn's satellite, Mimas. These rings' existence is intricately linked to their respective moons, Anthe and Methone. These moons exert perturbations on the ring particles, thereby influencing the ring structure. Notably, this results in the formation of two arcs, which are captured within the 10:11 and 14:15 corotation eccentric resonances (CER) with Mimas [1].

THE ROYAL SOCIETY PUBLISHING

Cassini images also revealed a denser region at the edge of the G ring, analogous to the Anthe and Methone arcs. This G ring arc possesses a radius of approximately 167,500 km and spans a length of 60° [1]. At the center of this arc's resonance lies the small satellite Aegaeon, which measures about 240 meters in radius and has a mass of 3×10^{10} kg, assuming a density of 0.5 kg/cm^3. In a manner similar to the other two arcs, the G-ring arc is azimuthally confined due to the 7:6 corotation eccentric resonance (CER) with Mimas [2–4]. For this resonance, the librating angle φ is expressed as

$$\varphi = 7\lambda_{Mimas} - 6\lambda_{Aegaeon} - \varpi_{Aegaeon}. \tag{1.1}$$

where λ_{Mimas} and $\lambda_{Aegaeon}$ denote the mean longitudes of Mimas and Aegaeon, respectively, and $\varpi_{Aegaeon}$ is the longitude of the pericentre of Aegaeon.

The G ring arc's total dust mass is approximately 10^6 kg. Notably, the strong background scattering observed in the G ring arcs suggests that micrometric particles constitute the primary population. Aegaeon imparts significant perturbations on the orbital paths of these particles, leading to frequent collisions with nearby particles and the small satellite itself [5]. Furthermore, given their size, these particles are susceptible to various disturbing forces. Solar radiation pressure, along with electromagnetic and plasma drag, can considerably perturb their orbits and consequently reduce the lifespan of these particles [1,6].

Solar pressure increases the eccentricity of the dust particles within the G ring arc, consequently diminishing their lifespan. The lifetime of these particles is capped at a maximum of 30 years for the 10 μm particles and merely three years for 1 μm grains. This duration is significantly shorter, over a hundred times, than the time taken for the satellite Aegaeon to repopulate the arc through collisions with interplanetary particles. This scenario contrasts with that of the Anthe and Methone arcs. For these arcs, both satellites generate sufficient dust from collisions between interplanetary particles and the moons, effectively replenishing the arc before solar pressure can deplete the dust. It is thus concluded that the satellites replenish the dust population of their respective arcs more rapidly than solar pressure can eliminate them [2,7,8].

The process that generates dust grains in Aegaeon's arc is markedly different from that in Anthe's and Methone's arcs. It takes the satellite approximately 30,000 years to produce a similar amount of dust in the arc, a period that three orders of magnitude longer than the time it takes for radiation pressure to remove particles from the arc [8]. This significant difference highlights the need for an alternative mechanism to keep the particles population in Aegaeon's arc in a steady state. This mechanism is likely associated with the combined effects of the ring's mean radius, its brightness, and the presence of macroscopic bodies within the G-ring arc [2].

The equivalent normal areas of the arcs associated with Aegaeon, Anthe, and Methone are approximately 50, 1.0, and 0.3 km^2, respectively. The G-ring exhibits a luminosity that is orders of magnitude greater than the other arcs. A comparison of the equivalent normal areas of these satellites and their respective rings reveals more striking differences. The equivalent areas of Aegaeon, Anthe, and Methone are 0.07, 0.84, and 2.21 km^2, respectively. This data suggests that Anthe's satellite and its ring exhibit comparable brightness levels, whereas Methone's satellite is brighter than its corresponding arc. In these instances, the mass of other bodies within these rings is negligible. However, the G-ring arc's equivalent normal area is nearly a thousand times larger than that of Aegaeon, indicating the presence of additional macroscopic bodies in the arc to account for the observed brightness [1,2].

To estimate the total mass of these macroscopic bodies, the Cassini spacecraft's Low Energy Magnetospheric Imaging Instrument (LEMMS) was utilized. LEMMS measured the electron flux within the ring, and specifically in the G ring's arc, it detected an energy reduction ranging from 1 to 10 MeV, suggesting that other bodies are absorbing these electrons. This energy drop corresponds to a total mass estimate of approximately 10^8 to 10^{10} kg, assuming a hypothetical ice composition with a density of 0.92 g/cm^3 [1,2]. It is also relevant to note that due to backward scattering, Cassini's cameras would only detect objects with a minimum radius of one hundred meters, implying that the mass observed by LEMMS is likely distributed among smaller bodies [2]

The presence of bodies, ranging from 1 to 100 meters in radius, within the G-ring arc, influences its dynamics and increases the chance of a collision with the Aegaeon. In densely populated and confined arcs, collisions can increase the libration amplitude and displace particles from the resonance. However, given Aegaeon's larger size compared to these other bodies, collisions may reduce its eccentricity and libration without displacing it from the resonance [2]. When massive bodies are trapped in corotation resonance, they exchange angular momentum and energy during close encounters. Yet, movement of one body towards corotation does not necessarily result in the other body moving away from exact corotation, allowing post-encounter trajectories in various directions [9].

According to [2], the presence of Aegaeon and other bodies in the G-ring arc could be attributed to a super-catastrophic collisions, with Aegaeon being the larger of the colliding bodies. An alternative hypothesis suggests that Aegaeon may have been captured during Mimas' migration from the A ring [10,11]. Further investigation is required to determine the precise origins of Aegaeon and other bodies within the G-ring arc. These insights contribute to our understanding of Saturn's ring system's dynamics and the various forces shaping its structure.

This study focuses on examining collisions among macroscopic bodies in the G ring's arc and their interactions with the satellite Aegaeon, to estimate dust production through these events. The objective is to determine whether these bodies can replenish the arc's dust and explore scenarios where dust production balances the rate at which solar pressure removes particles from the arc. The article proceeds with the numerical setup for n-body simulations, analysis of collision distributions, evaluation of dust production through smoothed particle hydrodynamic simulations, discussion on dust evolution in the arc, examination of Aegaeon's mass evolution, and concludes with final remarks.

2. Numerical setup

In this section, we present the setup of the numerical simulations employed to calculate the collision parameters within the arc. This is necessary for determining the typical collision parameters, including velocity and impact parameter, prevalent in the arc. These parameters will subsequently serve as initial conditions for the Smoothed Particle Hydrodynamics (SPH) simulations as discussed in Section 4.

We used the freely accessible modular N-body integrator REBOUND [12]. We chose the non-symplectic high-precision integrator with an adaptive time-step IAS15 integrator [13], and implemented additional terms correspondint to the acceleration due to the non-sphericity of Saturn.

To determine the initial conditions for our simulations we used physical parameters and gravity coefficients for Saturn shown in Table 1, while Table 2 presents the elements for the satellites. In this work, we performed two different sets of simulations, the first one including the satellite Aegaeon and the second without it, to understand the effect of the satellite on particles embedded in the arc. In all simulations, we included the J_2, J_4, and J_6 coefficients to determine the arc positions corresponding to the 7:6 resonances with Mimas.

Table 1: Saturn's physical parameters as used by [2].

Mass	5.683×10^26
Radius (km)	60330
J_2	0.016290543820
J_4	-0.000936700366
J_6	0.000086623065

To distribute the macroscopic bodies into the 7:6 CER, we utilized the algorithm described by [14]. This procedure compensates for the forced eccentricity $e_0 \sim (3/2)J_2(R/r)^2$ induced by

Table 2: Osculating orbital elements of the satellites Mimas and Aegaeon correspondint to the epoch 08/22/2008 UT 00:00:00, as used by [8].

Orbital Elements	Aegaeon	Mimas
a ($\times 10^5$ km)	1.6803398728	1.8600466879
e ($\times 10^{-2}$)	0.3133178063	1.7245224226
I ($^\circ$)	0.0017328550	1.5641747812
ϖ ($^\circ$)	142.49114788	163.18023984
Ω ($^\circ$)	236.30175623	259.15258436
M ($^\circ$)	5.3481201068	197.73278953

Saturn's oblateness [15]. We distributed 10,000 random particles inititally in circular orbits around the resonance balance point and calculated the resonance angle to identify those trapped in the resonance. Approximately 65% of the particles were found to be resonance-trapped and were randomly incorporated into our simulations.

In the simulations, the bodies are assumed to be 20 m in radius and having densities of either 0.5 or 0.9 g/cm^3. This choice reflects densities similar to icy bodies observed in other Saturnian rings [1], with those having 0.5 g/cm^3 being considered as porous. The radius was chosen as it falls below the detection threshold of Cassini's cameras, ensuring that the bodies simulated align with observational data [1]. With these parameters, the arc population contains approximately 1,200 macroscopic bodies with a density of 0.9 g/cm^3, or about 2,000 bodies at 0.5 g/cm^3, to account for the total estimated mass of 7×10^9 kg. This mass is equivalent to the upper limit derived the LEMMS instrument, as discussed in Section 1.

3. Outcome of the collisions

This section examines the velocity distribution and impact angles in collisions from our simulations. These simulations were divided into two groups, preserving identical initial conditions for the bodies, but differing in the inclusion of the Aegaeon satellite. We aim to analyze collisions among the bodies themselves as well as between the bodies and Aegaeon. By doing so, we seek to quantify typical velocities and impact angles, thereby estimating the dust production resulting from impacts involving these macroscopic bodies, both in the presence and absence of Aegaeon.

Figure 1 presents a heatmap of the relative velocity as a function of impact angle in collisions between a 20 m radius body and Aegaeon. The left graph depicts simulations with a 0.5 g/cm^3 body density, while the right with 0.9 g/cm^3. We can verify that typical collision velocities are around 5 m/s, ranging from 1 to 15 m/s, with impact angles predominantly between 30 and 50 degrees. No notable variance is observed between simulations with different body densities, as density variations only affect the number of bodies in the simulations.

Figure 2 illustrates a heatmap of relative velocity against impact angle for collisions between two 20 m radius bodies. The upper panels represent simulations with 0.5 g/cm^3 density, and the lower with 0.9 g/cm^3. The left plots include Aegaeon, while the right exclude it. These results indicate typical relative velocities of approximately 0.5 m/s, with velocities extending up to 10 m/s depending on the location of the bodies. The impact angles are predominantly below 60°, typically around 30°. Notably, Aegaeon's presence significantly influences the distribution of velocities and impact angles.

The distribution appears more uniform in simulations excluding Aegaeon, suggesting its significant effect on the velocities of bodies within the arc, particularly during close encounters. Comparing the typical collision velocity of 0.5 m/s between two macroscopic bodies with the 5 m/s impact velocity involving Aegaeon, it is evident that Aegaeon contributes to the acceleration of these bodies upon proximity. The acceleration caused by Aegaeon to a body approximately 500

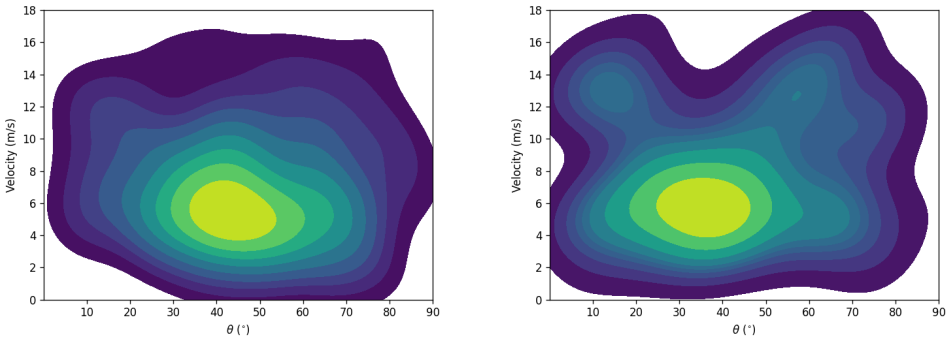

Figure 1: Relative velocities as a function of the impact angle (θ) in collisions between a 20 m radius body and Aegaeon. The left panel depicts the simulation with a density of 0.5 g/cm^3, and the right panel with 0.9 g/cm^3. These graphs demonstrate that the typical relative velocity of these collisions is around 5 m/s, and the impact angle predominantly occurs between 30 and 50 degrees.

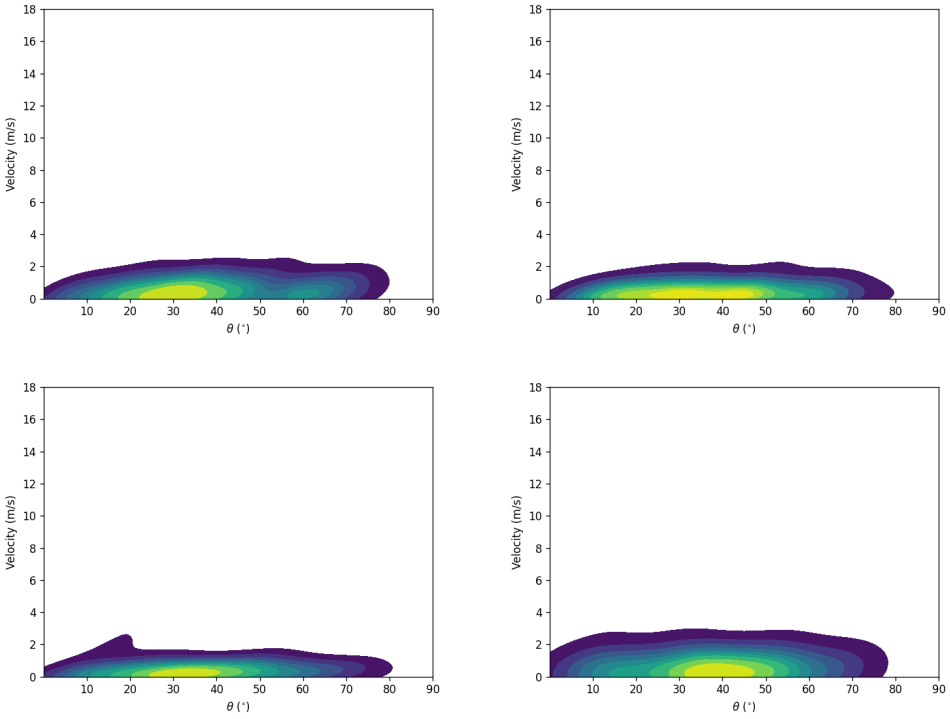

Figure 2: Relative velocities as a function of the impact angle (θ) in collisions between two macroscopic bodies. The upper panel represent simulations using a density of 0.5 g/cm^3, while the bottom uses 0.9 g/cm^3. The left plots include Aegaeon in the simulations, whereas the right ones exclude the satellite. These plots illustrate Aegaeon's influence on the velocity and impact angle distribution in collisions among macroscopic bodies.

m away is on the order of 10^{-4} m/s^2, in contrast to Saturn's acceleration of about 1 m/s^2 in the arc.

The primary objective of this article is to assess the impact of these hypothetical macroscopic bodies on dust production in the G-ring arc. To this end, we conducted simulations of typical collisions between macroscopic bodies and their impacts with Aegaeon using SPH. This approach aims to evaluate whether these collisional mechanisms contribute to sustaining the dust in the arc, considering that solar radiation pressure removes small particles in less than 40 years. Subsequently, we will present the outcomes of these collisions and estimate the total dust production from each collision type

4. Smoothed Particle Hydrodynamics

In realistic collision scenarios, the resultant fragment distribution is nonuniform, with significant variation in both size and velocity. To accurately understand the physical processes at play, it is essential to account for these variations. While the literature offers semi-analytical models for estimating collision outcomes and dust production, such as those proposed in [16], these models primarily focus on colisions between bodies in the gravitational regime. Our study, however, deals with collisions involving smaller bodies, falling outside the gravitational regime. Consequently, these semi-analytical models are unsuitable for our purposes, necessitating the simulation of collisions to comprehend the dynamics beyond the usual regime.

In this context, we will utilize parameters derived from N-body simulations as inputs for SPH simulations. This approach allows us to compute the mass, velocity, and dust production resulting from the collisions. Our methodology involves employing a hybrid hydrocode for simulating the initial disruption of small bodies at the collision point. Subsequent SPH simulations will be conducted to investigate shock propagation, material modification, and gravitational reaccumulation processes.

(a) Physical model

For modeling the collisional process and accurately predicting its outcome and dust production, we utilized a GPU-accelerated SPH code MILUPHCUDA [**?**]. This code implements a hydrodynamic approach combined with fracture modeling.

The code solves the standard conservation equations of mass, momentum, and energy, which are pivotal in depicting the behavior of elastic solids. This functionality enables precise modeling of the deformation and fragmentation of colliding bodies. We incorporated a plasticity model, utilizing an extended Von Mises-Drucker-Prager yield criterion [17], which modifies stresses beyond the elastic limit. This aspect is crucial for reflecting the material strength of the bodies and ensuring realistic simulation outcomes.

For brittle failure and fragmentation, we applied the approach by [18] in along with the [19] model. In this model, the material flaws, distributed according to a Weibull distribution, act as points of weakness that can become active and grow under tensile stress. The parameters for this distribution, specifically for ice, were derived by fitting data to rate-dependent fracture stress measurements in [20].

Under higher strain rates, materials experience gradual separation due to crack development and flaw activation, with cracks growing at a constant velocity. The effect of fractures is quantified through a scalar state variable, the damage, which represents the local stress reduction resulting from crack propagation. This variable serves as an indicator of the material's reduced strength under tensile loading. Upon reaching a fully damaged state, the material transforms into a cohesionless fluid, thus losing its capacity to withstand

We employed the Tillotson equation of state (EOS) [21] to simulate bodies under extreme conditions. This EOS is computationally efficient and adaptable, suitable for simulations involving a large number of particles or complex geometries. It effectively represents various physical states, including high temperatures, pressures, and densities, making it versatile for astrophysical simulations.

(b) SPH simulations

In the SPH simulations, we focused on the generation of dust from collisions between macroscopic bodies under various conditions. We examined how changes in the radii of these bodies influence their fragility and contribute to the emergence of the meter-size barrier. Additionally, we explored a range of velocities spanning from commonly observed high-impact velocities to lower thresholds where minimal damage occurred, distinguishing between cohesive collisions and mere adhesion.

In a typical collision setup, two bodies of equal size collide at a fixed impact angle of $\theta = 30^\circ$. In this setup, the target is impacted by a projectile moving at velocity V_i. The impact angle θ is determined at the initial contact between the bodies, formed by the line connecting their centers and the trajectory of the projectile's impact. The radii of the target and projectile, denoted as R and r, respectively, influence the dynamics of the collision. The impact parameter, $b = \sin\theta = B/(R + r)$, is calculated based on the geometry of the impact, where B is the distance from the center of the target to the point of first contact. The length l represents the overlap of the projectile with the target.

In the SPH simulations, the target and projectile were positioned at a mutual distance of $r_{ini} = R + r + 2.5h$, with h denoting the smoothing length, which defines the region of influence for neighboring particles.

Fragment identification, dynamics analysis, composition study, and dust production from a collision are intricate processes. We divided these analyses into two primary steps: Firstly, a 'friends-of-friends' algorithm is used to identify spatially connected SPH particle clusters as "fragments". This is followed by determining gravitationally bound "aggregates" of these fragments. The largest aggregate is initially identified using the most massive fragment and all gravitationally bound fragments to it. An iterative approach is then applied to refine this aggregate. The process is repeated to identify the second-largest aggregate, starting with the most massive fragment not yet included in the largest one [22].

The SPH simulations were conducted with 150,000 particles for each body, both target and projectile, ensuring enough resolution for various collision scenarios. The runtime of the simulations was primarily dependent on the body's size and the impact velocity, which in turn determined the overall simulated time.

We determine dust production based on the SPH particle resolution in the simulation. In our case, dust predominantly consists of fragments representing less than 0.01% of the total mass, composed of single fully damaged particles. Thus, any fragment smaller than this threshold is classified as dust. By aggregating these fragments, we can quantify the dust generated post-collision.

Table 3 provides a comprehensive summary of dust production from collisions between two same-size bodies, considering their radii and impact velocities, with a uniform impact angle of 30 degrees for all scenarios. The final snapshot of these simulations, demonstrating the outcomes, is illustrated in Figure 7 in the appendix.

Table 3: Dust generation from different collision setups using a fixed impact angle of 30°.

Radius		1 m	5 m	10 m	20 m
	Velocity		Dust produced		
	2 m/s	0.00%	0.00%	0.00%	0.00%
	10 m/s	0.00%	0.14%	0.34%	0.00%
	20 m/s	0.01%	0.62%	0.60%	0.59%

Table 3 indicates that dust production is affected by both the radius of the bodies and the collision velocity. At 2 m/s, no dust is generated regardless of body size. However, as the velocity increases, there is a notable rise in dust generation, especially for larger bodies. For example, at 10

m/s, a small amount of dust is produced for bodies with radii of 5m and 10m, but not for smaller or larger ones, suggesting a possible threshold velocity for dust generation relative to body size.

Figure 3 visually distinguishes between damaged particles (shown in the left panel) and the mass fragments' distribution along with their velocities. This visualization clearly identifies the fragments resulting from the simulation.

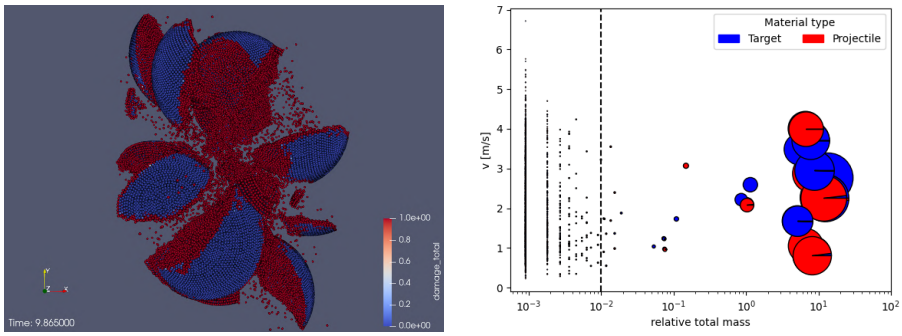

(a) Snapshot showing the damaged particles

(b) Relative mass of fragments and their velocity.

Figure 3: Fragments and dust from a impact at 10 m/s

Collisions among macroscopic bodies generally occur at low velocities, leading to minimal dust production regardless of the bodies' sizes. To investigate alternate dust generation mechanisms, we focused on collisions with Aegaeon, which constitutes about 40% of total collisions in the arc verified in the N-bodies simulations.

For a simplified model, we adopted a standard collision scenario involving a relative velocity between 5 m/s and 10 m/s and an impact angle of 45°. This setup is comparable with typical collisions observed in our simulations. In Figure 4, we illustrate the mass fragment distribution and corresponding velocities from an SPH simulation of a collision between a 240 m-sized target (Aegaeon) and a 20 m-sized projectile at 10 m/s, at an angle of 45°. The projectile was simulated with 10,000 SPH particles, while Aegaeon was modeled using 1,000,000 SPH particles. Due to resolution and the size of the bodies, only a portion of the satellite was included in the simulation. The results show significant disruption of the projectile, with 76.47% of its mass forming smaller fragments, and the remaining 23.53% becoming dust particles.

Table 4 details dust production resulting from various collision scenarios between a projectile and Aegaeon. This table considers different projectile velocities and impact angles. From the table, it is evident that dust production varies significantly with changes in the projectile's velocity and impact radius. In typical collisions with Aegaeon, moderate velocities and impact angles tend to result in an average dust production of around 10%.

Table 4: Dust production from a collision between a projectile with Aegaeon.

	Velocity	Dust produced	
Projectile:		r =10 m $\theta = 30^\circ$	r = 20 m $\theta = 45^\circ$
	5 m/s	9.38%	6.63%
	10 m/s	17.37%	23.53%

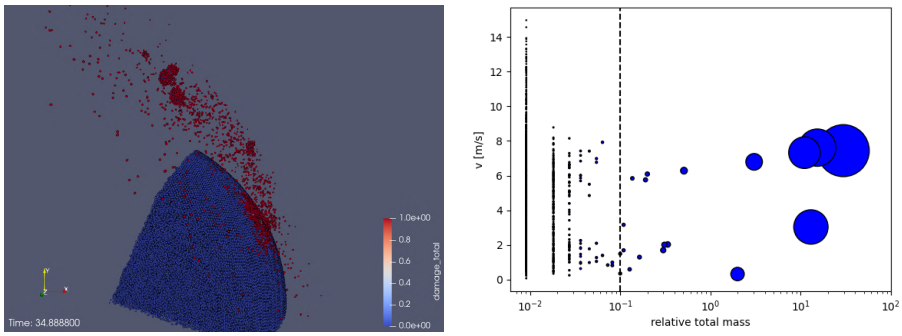

(a) Snapshot showing damaged particles from the projectile impacting Aegaeon.

(b) Velocity and mass distribution of fragments post-collision.

Figure 4: Fragments and dust from a 10 m/s impact velocity.

A more comprehensive discussion of the results from all SPH simulations will be addressed in a forthcoming paper. This paper will delve into the distribution of fragments resulting from the collisions and estimate the proportion of these fragments that remain embedded in the arc post-collision.

5. Dust Production Through Aegaeon Impacts

This section focuses on estimating the mass produced by impacts between macroscopic bodies and the satellite Aegaeon. Notably, the dust generation from collisions among macroscopic bodies is not considered here, since only a subset of these collisions produce dust, and they do so at a lower rate compared to collisions with Aegaeon. In simulations of various impact setups with Aegaeon, it was observed that approximately 10-70% of the impactor's mass converts into dust and smaller fragments.

Figure 5 shows the total number of impacts of macroscopic bodies on Aegaeon over time, based on N-body simulations. The full-dashed line represents simulations using bodies with a density of 0.5 g/cm^3, and the dashed line for those with 0.9 g/cm^3. In the simulation with porous bodies, there were 142 impacts, while in the non-porous simulation, there were 83 impacts over 1000 years. From this data, we can roughly estimate an impact frequency with Aegaeon at about one collision every 8 years for porous bodies and one every 13 years for non-porous bodies, based on a simple linear fit. However, this ratio is only applicable over a short period, as the bodies gradually disintegrate over time. Additionally, the cumulative effect of producing fragments in each collision, which may subsequently collide with Aegaeon, generating more dust, is not considered in this calculation.

To estimate assess the evolution of dust in the arc and examine scenarios that could keep the dust population in a steady state, we applied an exponential decay model based on the dust particles' lifetime [8]. Our analysis spans various particle sizes, from 1μm to 10μm. Additionally, every time a collision with Aegaeon was detected in our simulations, we added the corresponding amount of dust generated by that collision into the system. This approach allowed us to integrate the continuous production of dust from these impacts. By combining the natural decay of dust particles with the new dust generated from collisions with Aegaeon, we could compute dust population within the arc.

Figure 6 shows the moving average of dust quantity (normalized by the current dust amount in the arc, approximately 10^6 kg) over time for each scenario at $v = 5v_{esc}$. The evolution patterns

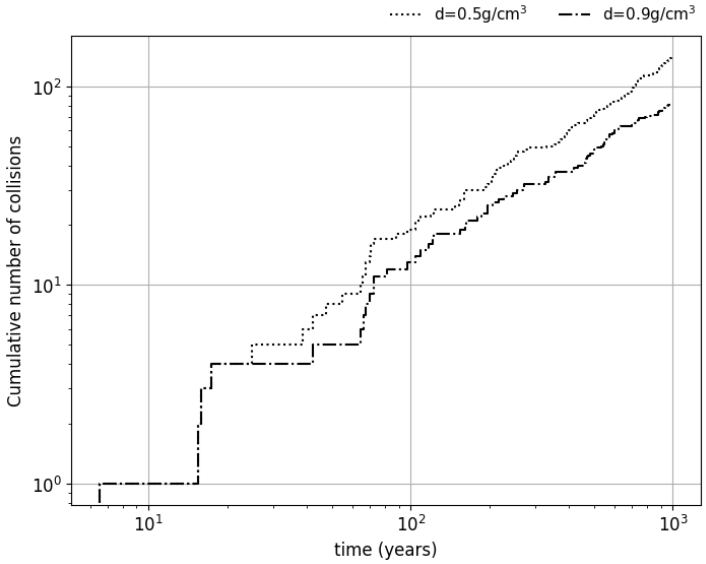

Figure 5: Cumulative number of collisions with the satellite Aegaeon for bodies with densities of 0.5 g/cm^3 and 0.9 g/cm^3.

for dust particles at $v = 1v_{esc}$ and $v = 10v_{esc}$ show similar general behaviors, as the focus is on the moving average of dust quantity.

Our findings suggest it is possible to maintain dust population in the arc for the simulated period of 1000 years, both for the porous or non-porous scenarios. However, keeping 1μm particles is challenging due to their short lifespan. We then propose that the arc's dust could originate from collisions between macroscopic bodies and Aegaeon, leading to their fragmentation and dust generation. This hypothesis becomes more compelling when considering an underestimation of collision frequency with Aegaeon, as we only accounted for 20 m radius bodies. A more realistic scenario with bodies ranging from 1 to 50 m in radius could significantly increase collision rates and dust production. Such a scenario supports the theory that the G-ring arc may have originated from a super-catastrophic collision, fragmenting a larger body into Aegaeon (the largest fragment) and numerous smaller fragments, which continue to generate dust in the arc.

The impacts studied can effectively replenish the dust particles within the arc, and the arc lifetime depends on the quantity of bodies immersed in it. Under the examined scenario, a balanced system could be sustained for at least a thousand years as these bodies gradually fragment. Nonetheless, it is evident that this system is transitory.

Estimating the distribution of these bodies in terms of radius is challenging, but it is clear that a higher number of bodies would prolong the arc's existence. Moreover, our impact rate estimation with Aegaeon is conservative, as we have not include in the analysis the likelihood of subsequent collisions involving fragments generated from initial impacts.

Additionally, we might consider the possibility of a 'firefly' behaviour characterized by fluctuating brightness. In a situation with few bodies in the arc, the frequency of impacts with Aegaeon would reduce significantly, leading to brief periods of intensified brightness following each collision. This hypothesis highlights the dynamic nature of the arc's brightness based on the population and activity of macroscopic bodies within it.

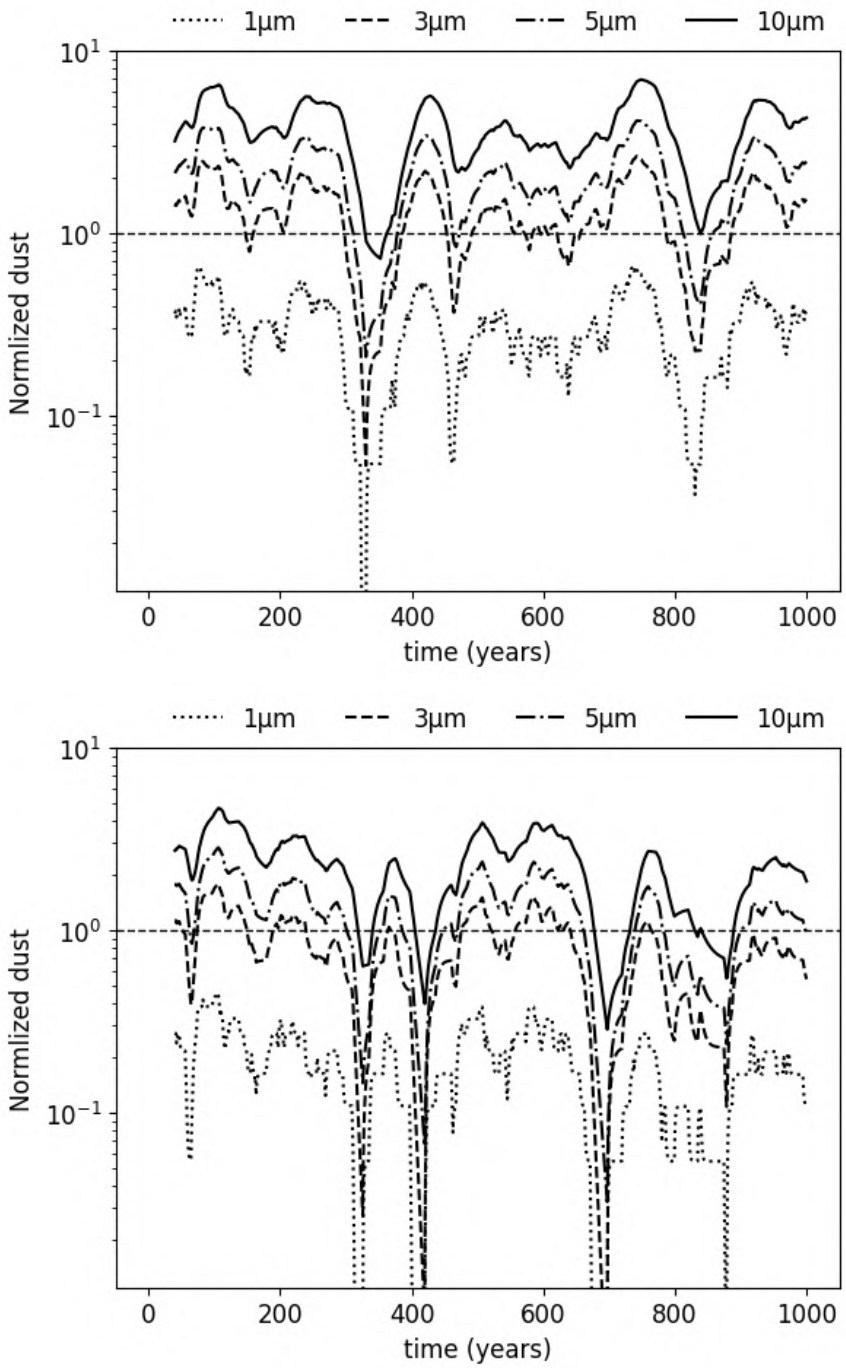

Figure 6: Normalized dust quantity (by the current dust amount in the arc) over time. The plots represent dust produced by collisions between 20 m radius bodies and Aegaeon, interpolated with decay due to solar pressure radiation for particles of 1μm, 3μm, 5μm, and 10μm. The upper panel is for collisions with 0.5 g/cm^3 density bodies, and the bottom for 0.9 g/cm^3. The dashed line represents the current dust amount in the arc, approximately 10^6 kg.

6. Mass Evolution of Aegaeon

We also examined the mass evolution of Aegaeon through its collisions with the bodies within the arc. Across all simulations, Aegaeon did not experience any catastrophic collision, nor did it lose a significant amount of mass. The satellite sustained minimal damage and remained intact in all types of collisions modeled in the N-body simulations. These findings imply that the macroscopic bodies, being at least three orders of magnitude less massive than Aegaeon, can coexist with the satellite without substantially affecting its mass. Drawing from [2], these bodies are believed to be no larger than 50 meters in diameter, insufficient to cause significant destruction to Aegaeon, given the relative velocities observed in the arc.

For completeness, we also simulated the arc with 2000 larger bodies, ranging from 50 to 100 meters, under the assumption of perfect merging to potentially create a second body comparable in mass to Aegaeon. Two sets of simulations were conducted: one including Aegaeon and the other without it. These simulations revealed that when Aegaeon was present, it grew in size but prevented other bodies from similarly increasing in mass. Conversely, in the simulation without Aegaeon, a single body rapidly gained mass while inhibiting growth in others. These outcomes suggest that the formation of other massive bodies through collisions is unlikely, as Aegaeon or another dominant body tends to block the mass accumulation in other bodies within the arc.

7. Final Remarks

The G-ring arc is predominantly composed of micrometric particles, which are greatly influenced by external forces, particularly solar radiation pressure. This pressure results in the removal of these particles from the arc in under 40 years. Aegaeon, the satellite, cannot replenish these particles at a rate enough through collisions with interplanetary particles, as it requires at least 3000 years to generate the current dust mass. Consequently, an alternative mechanism is necessary to keep the dust population in the arc.

One possible mechanism involves the macroscopic bodies present in the arc. Collisions between these bodies, as well as with Aegaeon, could be a source of dust. This study investigated this theory through N-body and SPH simulations, focusing on the dust generated by such collisions. The findings indicate that collisions among macroscopic bodies alone are insufficient to replenish the arc's dust. However, impacts involving Aegaeon can convert 10-60% of the impactor mass into dust, depending on the collision parameters. A standard collision was assumed in this study, with a relative velocity of 5 m/s and an impact angle of 45°, and it was posited that each impact with Aegaeon could convert 10% of the impactor's mass into dust, aiding in arc replenishment.

The results demonstrate that the arc can survive for thousands of years due to impacts with Aegaeon. These impacts do not lead to significant mass loss for Aegaeon, which remains intact post-collision. The study modeled the macroscopic body population as exclusively comprising 20 m bodies. From the SPH collision simulations, it is apparent that even a single impact is sufficient to repopulate the arc's dust material. However, as these bodies gradually break apart, the material for generating new dust diminishes, and the impact frequency decreases. Thus, the arc's lifespan depends on the distribution and total number of macroscopic bodies present. The study did not account for the possibility that each collision could produce additional fragments that may collide again with Aegaeon, potentially extending the arc's lifespan.

In conclusion, the G-ring arc may be temporary and exhibits fluctuating dust levels, dependent on the number and size distribution of macroscopic bodies. Precisely estimating the arc's lifespan is challenging due to these variables. Nonetheless, the presence of these bodies, if confirmed, could be crucial for maintaining the arc through collisions with Aegaeon. A small number of bodies in the arc could lead to intermittent brightness spikes following impacts, whereas a larger population might result in a more stable and consistently bright system. Future work will involve additional SPH simulations to gain deeper insights into dust production and the trajectories and

velocities of smaller bodies generated by these impacts. The findings from these studies will be detailed in a forthcoming paper.

Data Accessibility. The data is available through contact with the authors.

Funding. This work was supported by the following entities:
CAPES - Coordenação de Aperfeiçoamento de Pessoa de Nível Superior - Process Number: 1684418
CAPES - Coordenação de Aperfeiçoamento de Pessoal de Nível Superior - Brasil (CAPES) - Finance Code 001
DFG German Research Foundation project 446102036
FAPESP (Processo 2016/24561-0)

Conflict of interests. The authors declare no conflict.

References

1. Hedman M, Burns JA, Tiscareno MS, Porco CC, Jones GH, Roussos E, Krupp N, Paranicas C, Kempf S. 2007 The Source of Saturn's G Ring. *Science* **317**, 653–656.
2. Hedman M, Cooper NJ, Murray CD, Beurle K, Evans MW, Tiscareno MS, Burns JA. 2010 Aegaeon (Saturn LIII), a G-ring object. *Icarus* **207**, 433–447.
3. El Moutamid M, Renner S, Sicardy B. 2011 Dynamics of the small moons perturbed by Mimas. In *AAS/Division for Planetary Sciences Meeting# 43* p. 972.
4. El Moutamid M, Sicardy B, Renner S. 2014 Coupling between corotation and Lindblad resonances in the presence of secular precession rates. *Celestial Mechanics and Dynamical Astronomy* **118**, 235–252.
5. Rodríguez A, Callegari Jr N. 2021 Dynamical stability in the vicinity of Saturnian small moons: the cases of Aegaeon, Methone, Anthe, and Pallene. *Monthly Notices of the Royal Astronomical Society* **506**, 5093–5107.
6. Madeira G, Giuliatti Winter SM. 2020 Effects of immersed moonlets in the ring arc particles of Saturn. *European Physical Journal Special Topics* **229**, 1527–1543. (10.1140/epjst/e2020-900129-5)
7. Sun KL, Seiß M, Hedman M, Spahn F. 2017 Dust in the arcs of Methone and Anthe. *Icarus* **284**, 206–215.
8. Madeira G, Sfair R, Mourão DC, Giuliatti Winter SM. 2018 Production and fate of the G ring arc particles due to Aegaeon (Saturn LIII). *Monthly Notices of the Royal Astronomical Society* **475**, 5474–5479.
9. A'Hearn JA, Hedman MM, El Moutamid M. 2019 Dynamics of multiple bodies in a corotation resonance: Conserved quantities and relevance to ring arcs. *The Astrophysical Journal* **882**, 66.
10. Araujo NCS, Vieira Neto E, Foryta DW. 2016 Formation of the G-ring arc. *Monthly Notices of the Royal Astronomical Society* **461**, 1868–1874.
11. El Moutamid M, Sicardy B, Renner S. 2017 Derivation of capture probabilities for the corotation eccentric mean motion resonances. *Monthly Notices of the Royal Astronomical Society* **469**, 2380–2386.
12. Rein H, Liu SF. 2012 REBOUND: an open-source multi-purpose N-body code for collisional dynamics. *Astronomy and Astrophysics* **537**.
13. Rein H, Spiegel DS. 2015 IAS15: a fast, adaptive, high-order integrator for gravitational dynamics, accurate to machine precision over a billion orbits. *Monthly Notices of the Royal Astronomical Society* **446**, 1424–1437.
14. Renner S, Sicardy B. 2006 Use of the Geometric Elements in Numerical Simulations. *Celestial Mechanics and Dynamical Astronomy* **94**, 237 – 248.
15. Borderies-Rappaport N, Longaretti PY. 1994 Test particle motion around an oblate planet. *Icarus* **107**, 129–141.
16. Leinhardt ZM, Stewart ST. 2012 Collisions between Gravity-dominated Bodies. I. Outcome Regimes and Scaling Laws. *The Astrophysical Journal* **745**, 79.
17. Fish, M. A. 1997 Ice strength as a function of hydrostatic pressure and temperature. *Cold Regions Research and Engineering Laboratory (U.S.)* **97**.
18. Benz W, Asphaug E. 1999 Catastrophic Disruptions Revisited. *Icarus* **142**, 5–20. (10.1006/icar.1999.6204)
19. Grady D, Kipp M. 1980 Continuum modelling of explosive fracture in oil shale. *International Journal of Rock Mechanics and Mining Sciences &amp Geomechanics Abstracts* **17**, 147–157. (10.1016/0148-9062(80)91361-3)

20. Lange MA, Ahrens TJ, Boslough MB. 1984 Impact cratering and spall failure of gabbro. *Icarus* **58**, 383–395. (10.1016/0019-1035(84)90084-8)
21. Tillotson JH. 1962 Metallic Equations of State For Hypervelocity Impact. General Atomic Report GA-3216. 1962. Technical Report.
22. Burger C, Maindl TI, Schäfer CM. 2017 Transfer, loss and physical processing of water in hit-and-run collisions of planetary embryos. *Celestial Mechanics and Dynamical Astronomy* **130**. (10.1007/s10569-017-9795-3)

A. Simulation Snapshots

(a) r = 1m

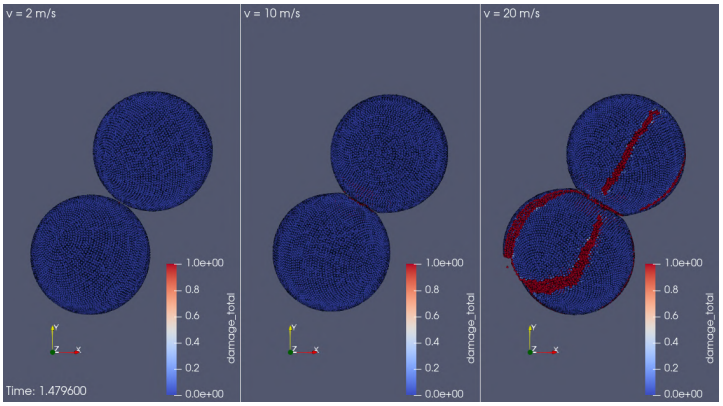

(b) r = 5m

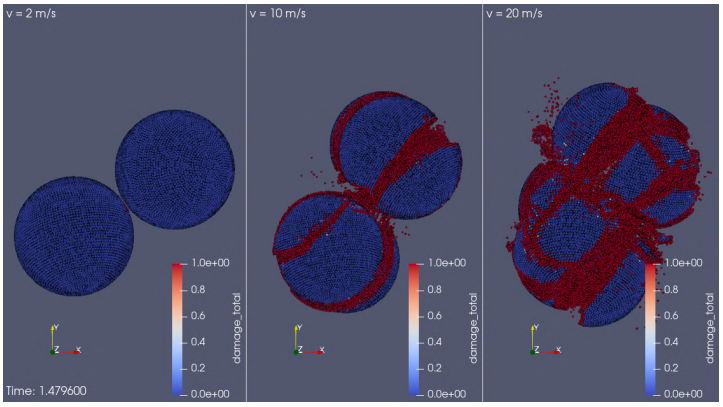

(c) r = 10m

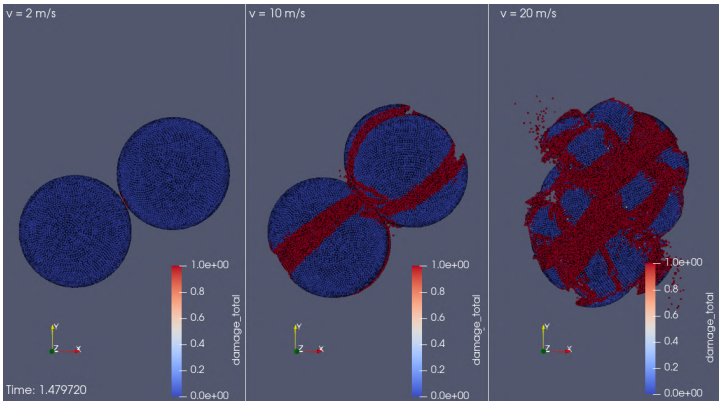

(d) r = 20m

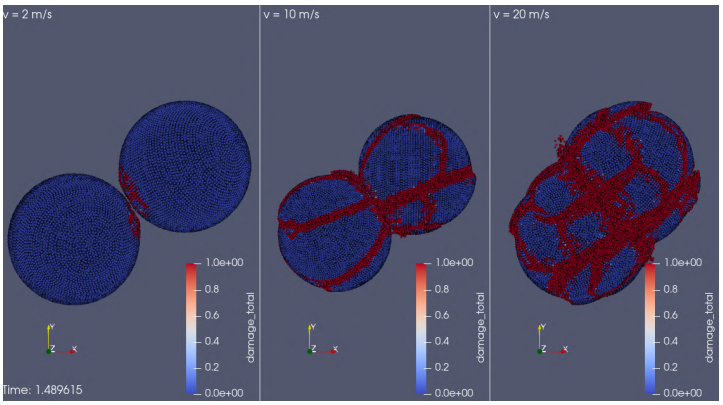

Figure 7: Snapshots from different collision setups using a fixed impact angle ($\theta = 30°$).

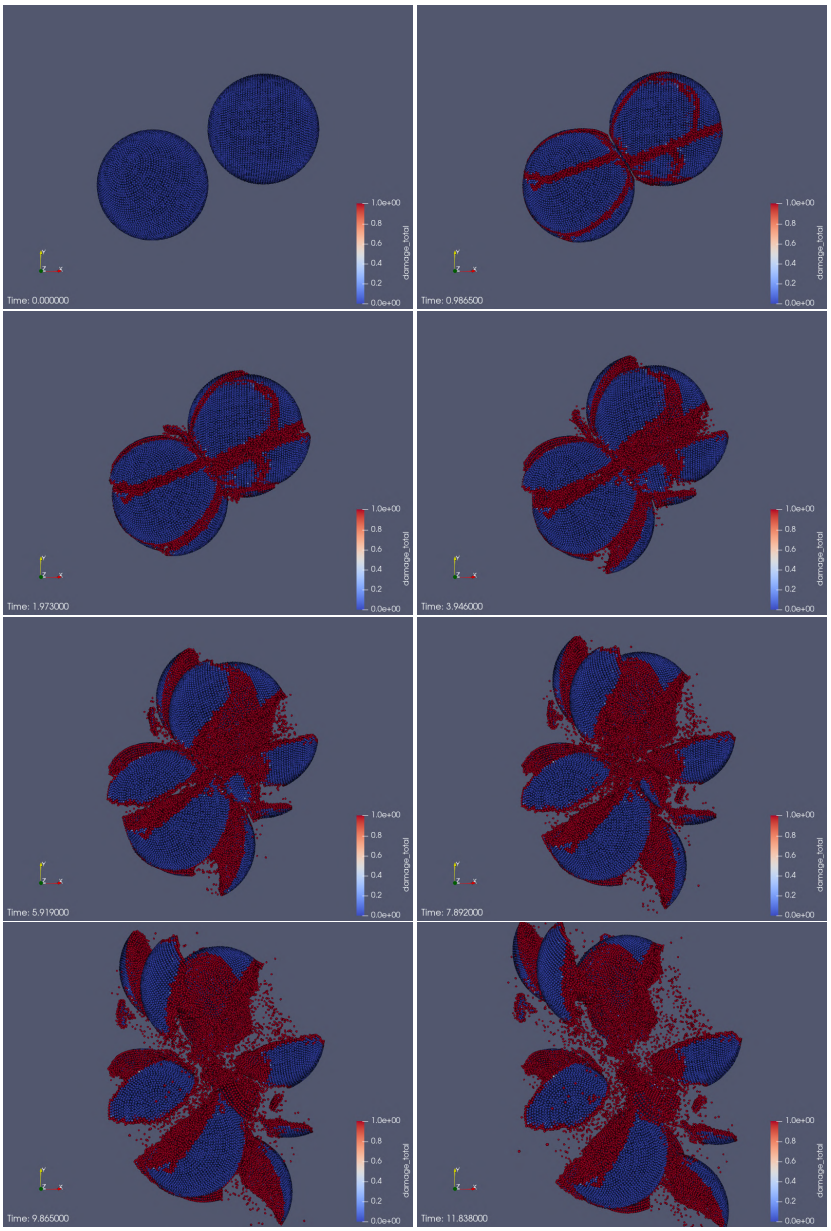

Figure 8: Snapshots showing the damage from two equal 20 m-sized bodies at v = 10 m/s and $\theta = 30^\circ$ angle of impact.

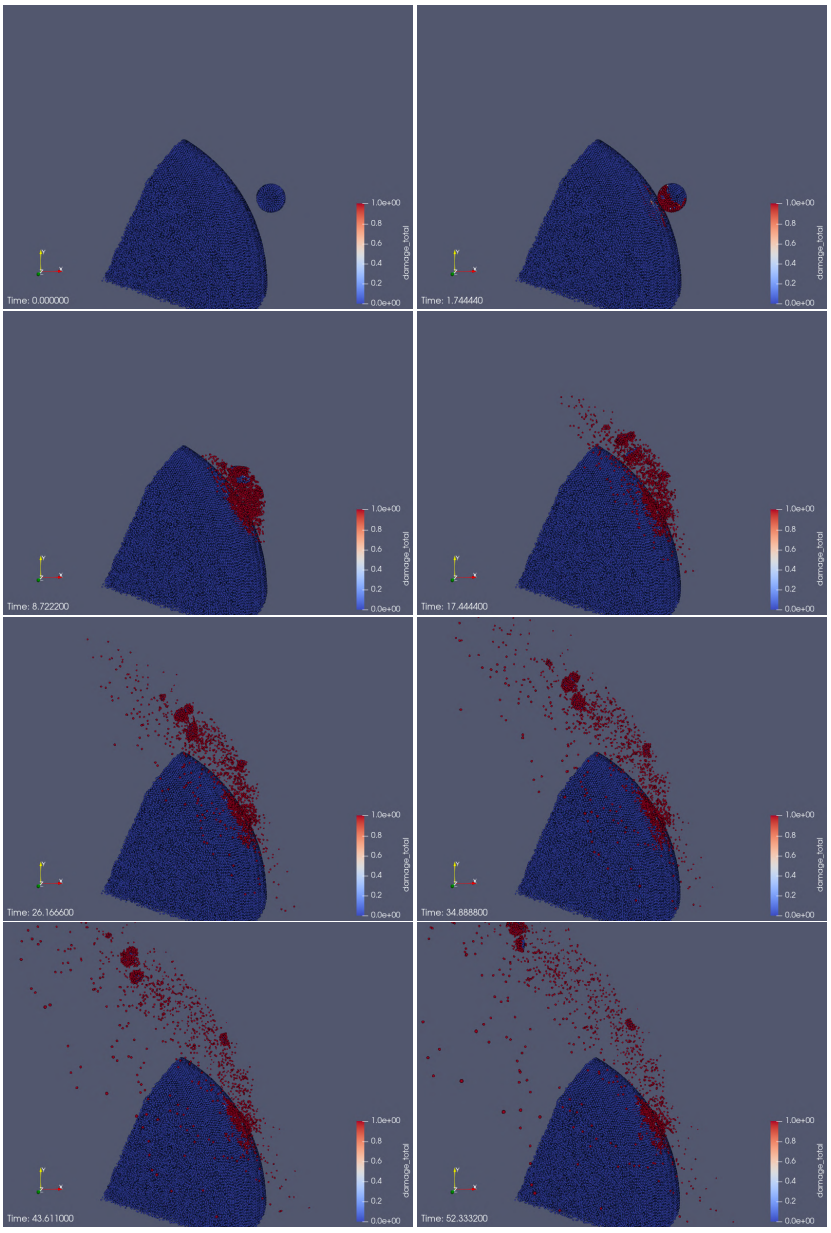

Figure 9: Snapshots of Aegeon impacted by a 20 m-sized projectile at 10 m/s and an angle of $45°$.

APPENDIX B – WATER DELIVERY DURING THE PLANET FORMATION

B.1 SYSTEMS FORMED FROM DIFFERENT SETUPS FOR THE FORMATION OF THE SOLAR SYSTEM

Here we illustrate the systems formed in different setups for the formation of the Solar System. We present the radial distribution of planets and the mass compared to the Solar System planets. The color of the dots represent the amount of water delivery to each planet considering a H_20 zone ring with a total mass of one Earth mass.

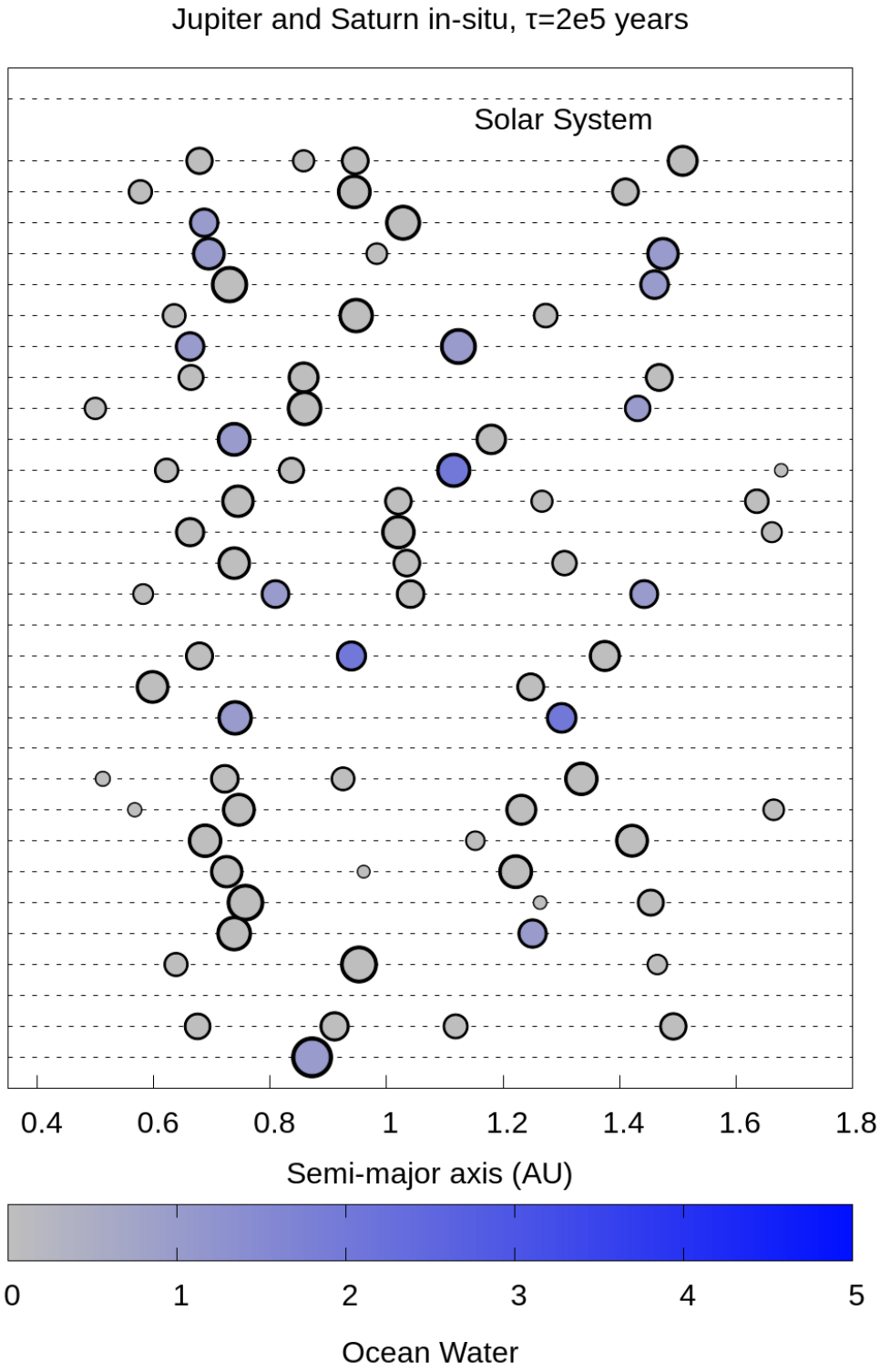

Figure B.1 – Systems formed by invoking early instability, with Jupiter and Saturn growing in situ in 200 thousand years. The plot shows the number and position of the planets for each simulation using the same numerical setup. The color represents the amount of water delivered by the C-type planetesimals originating from the H_2O zone ring. The amount of water was calculated using a distribution of 1 Earth Mass distributed across the planetesimals in the H_2O zone ring.

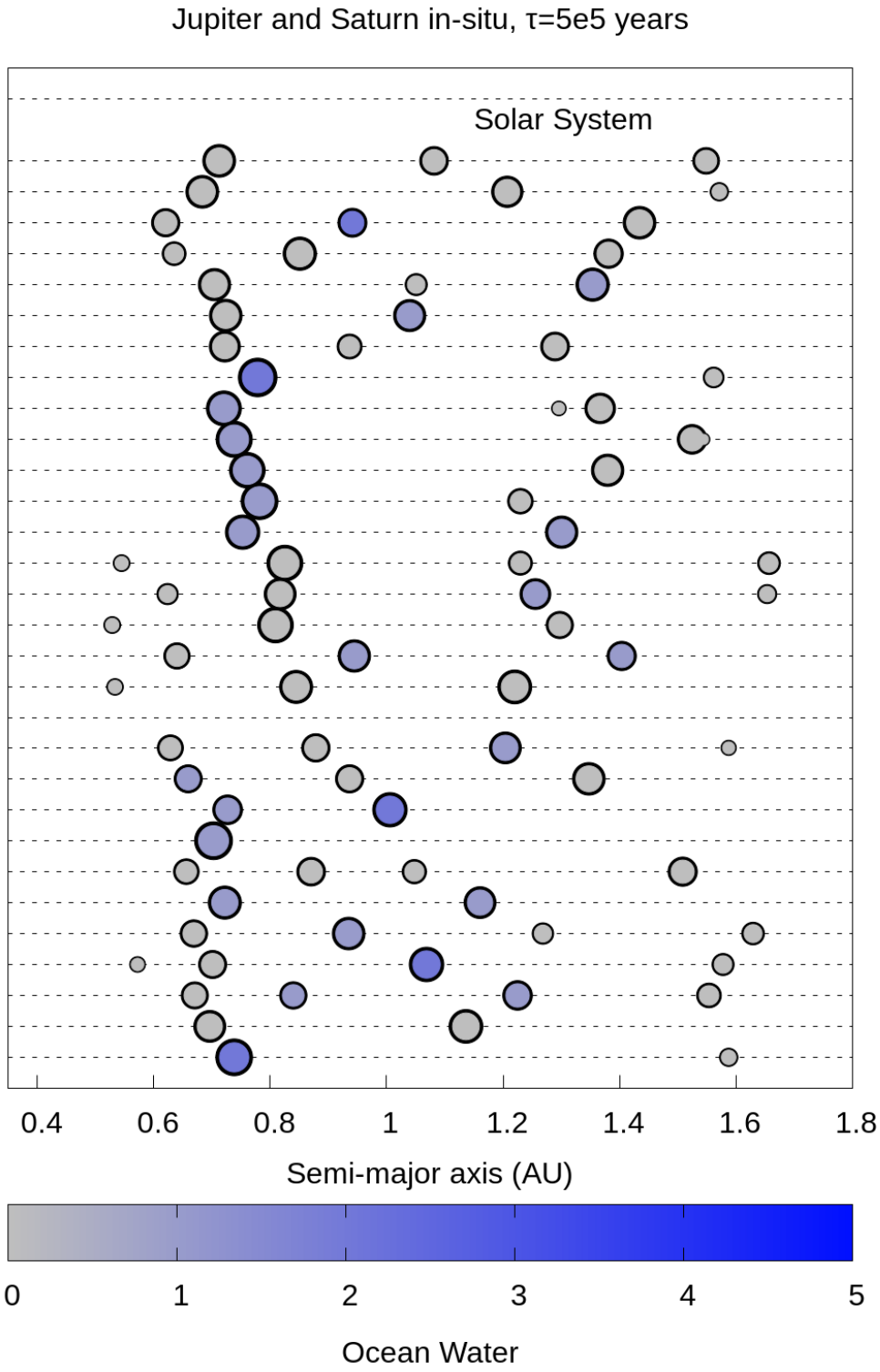

Figure B.2 – Systems formed by invoking early instability, with Jupiter and Saturn growing in situ in 500 thousand years. The plot shows the number and position of the planets for each simulation using the same numerical setup. The color represents the amount of water delivered by the C-type planetesimals originating from the H_2O zone ring. The amount of water was calculated using a distribution of 1 Earth Mass distributed across the planetesimals in the H_2O zone ring.

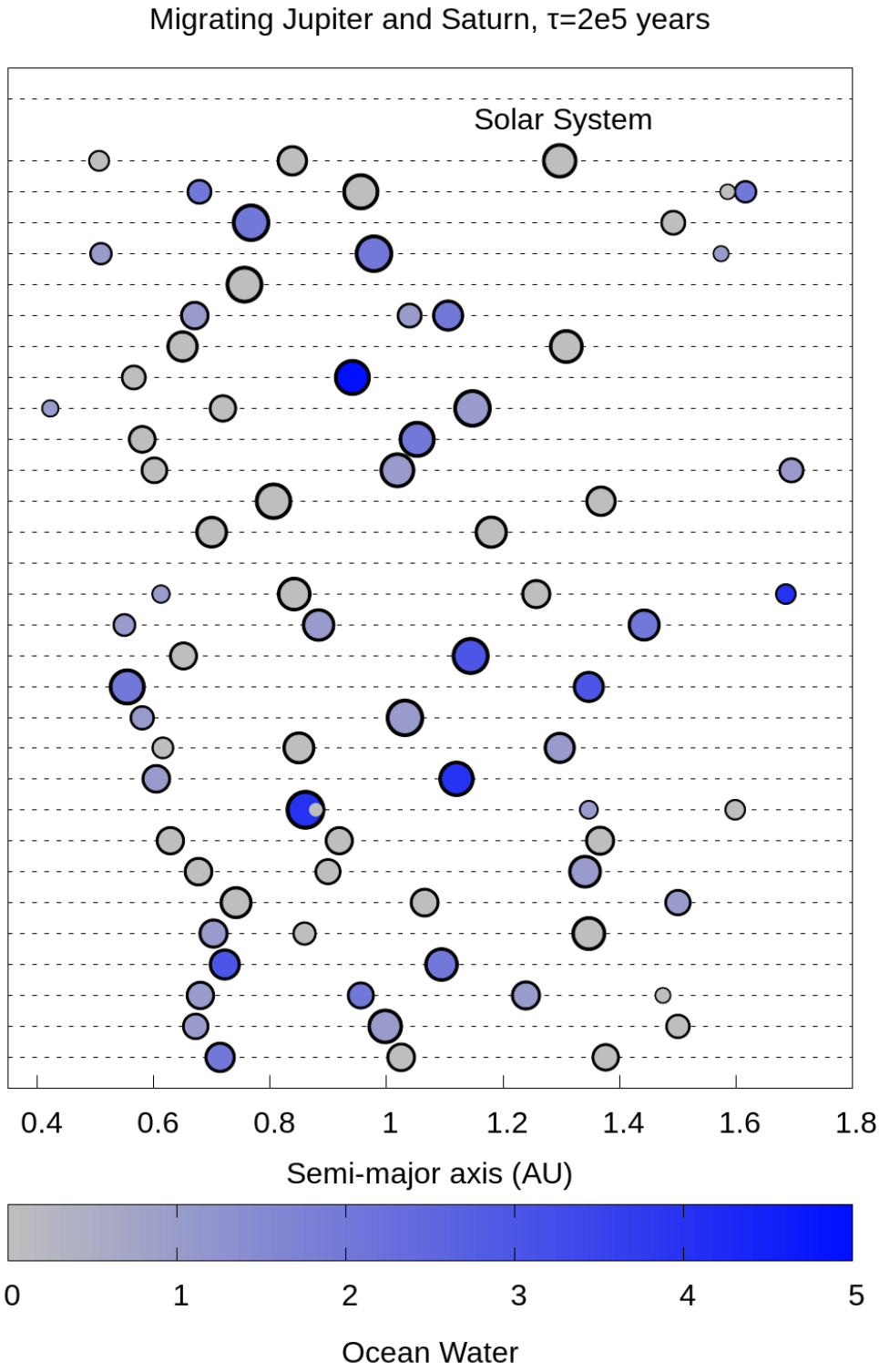

Figure B.3 – Systems formed invoking early instability, migrating Jupiter and Saturn and growing in 200 thousand years. The plot shows the number and position of the planets for each simulation using the same numerical setup. The color represents the amount of water delivered by the C-type planetesimals originating from the H_2O zone ring. The amount of water was calculated using a distribution of 1 Earth Mass distributed across the planetesimals in the H_2O zone ring.

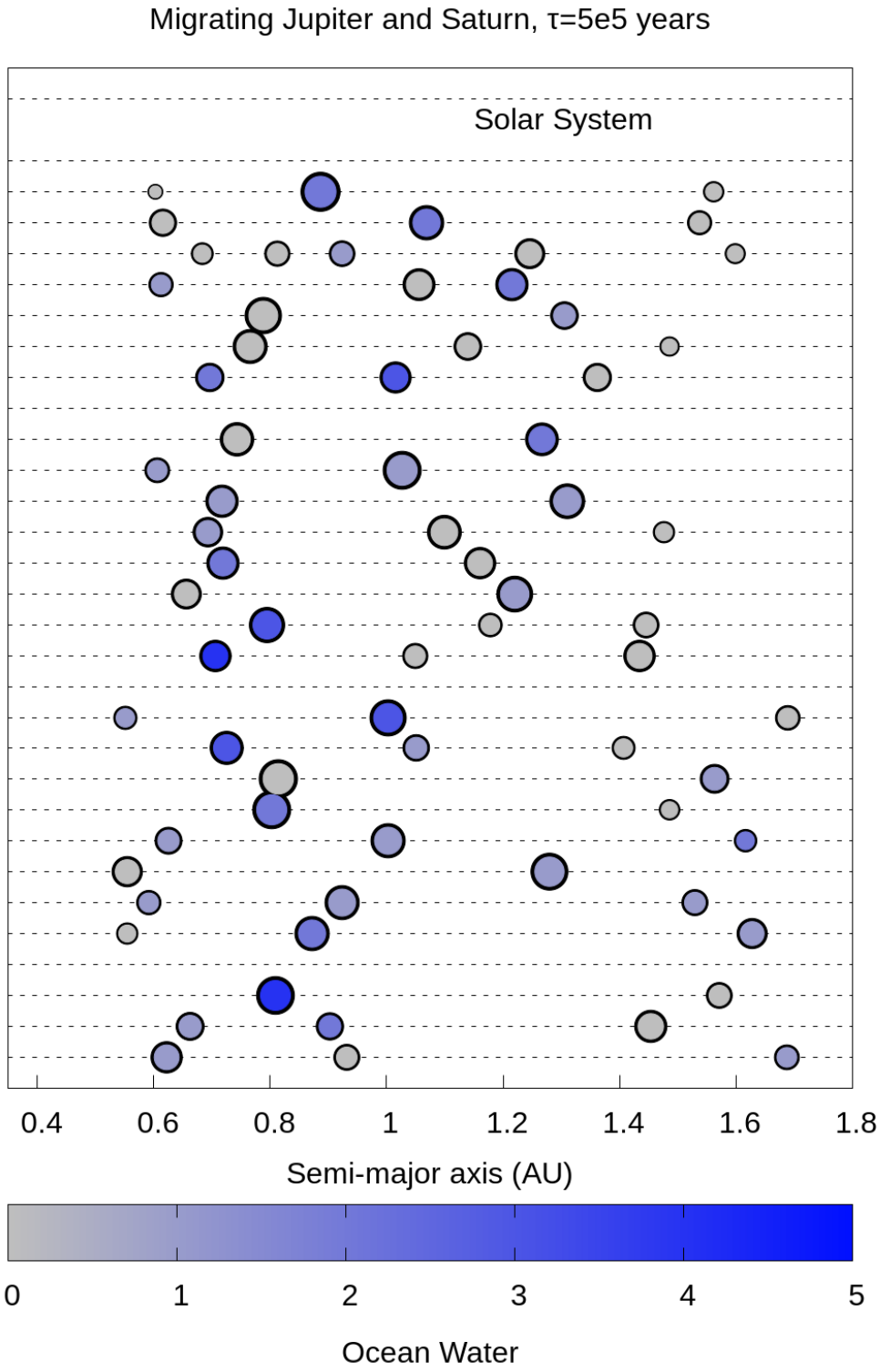

Figure B.4 – Systems formed invoking early instability, migrating Jupiter and Saturn and growing in 500 thousand years. The plot shows the number and position of the planets for each simulation using the same numerical setup. The color represents the amount of water delivered by the C-type planetesimals originating from the H_2O zone ring. The amount of water was calculated using a distribution of 1 Earth Mass distributed across the planetesimals in the H_2O zone ring.

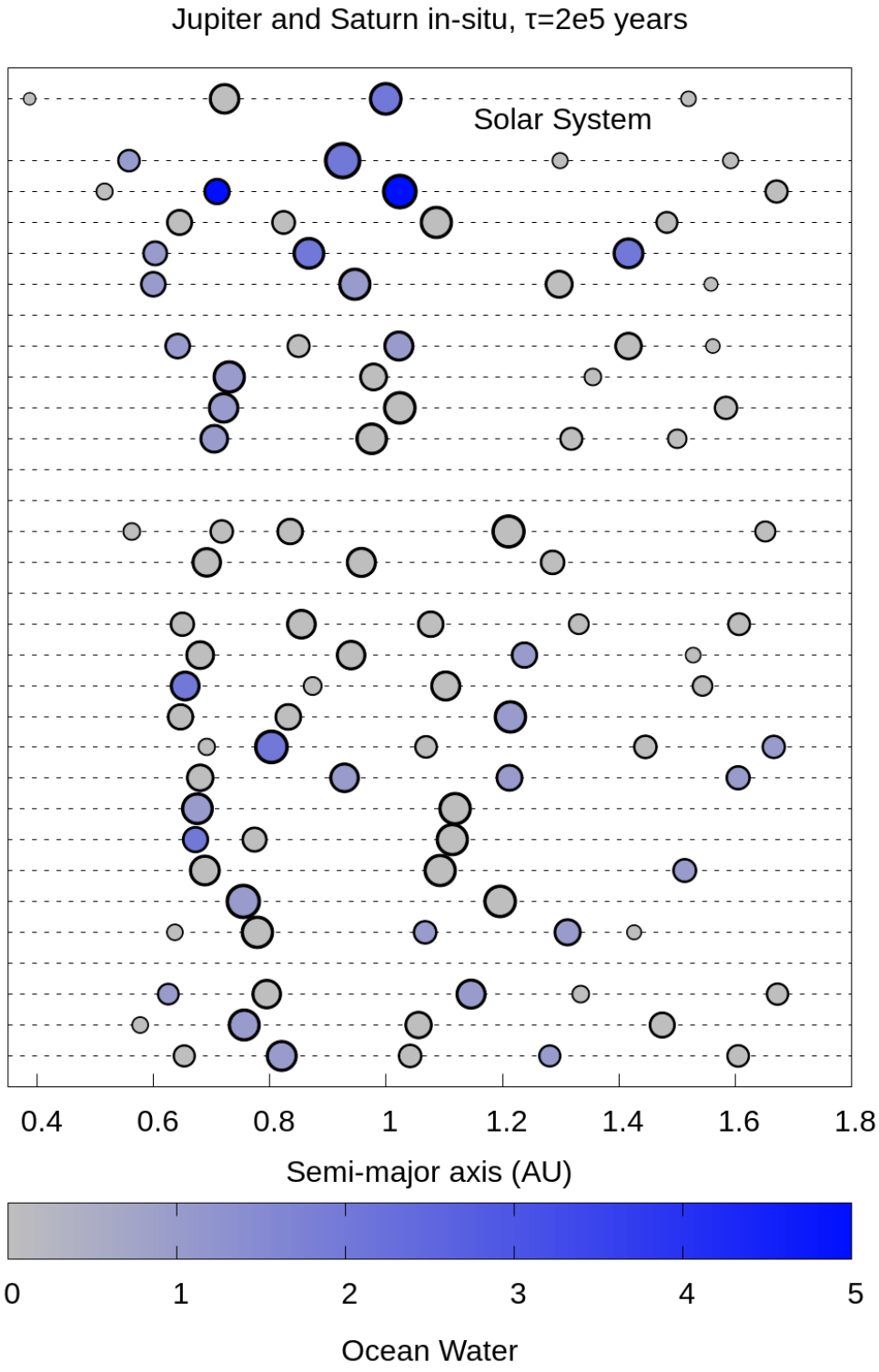

Figure B.5 – Systems formed without invoking early instability, with Jupiter and Saturn growing in situ in 200 thousand years. The plot shows the number and position of the planets for each simulation using the same numerical setup. The color represents the amount of water delivered by the C-type planetesimals originating from the H_2O zone ring. The amount of water was calculated using a distribution of 1 Earth Mass distributed across the planetesimals in the H_2O zone ring.

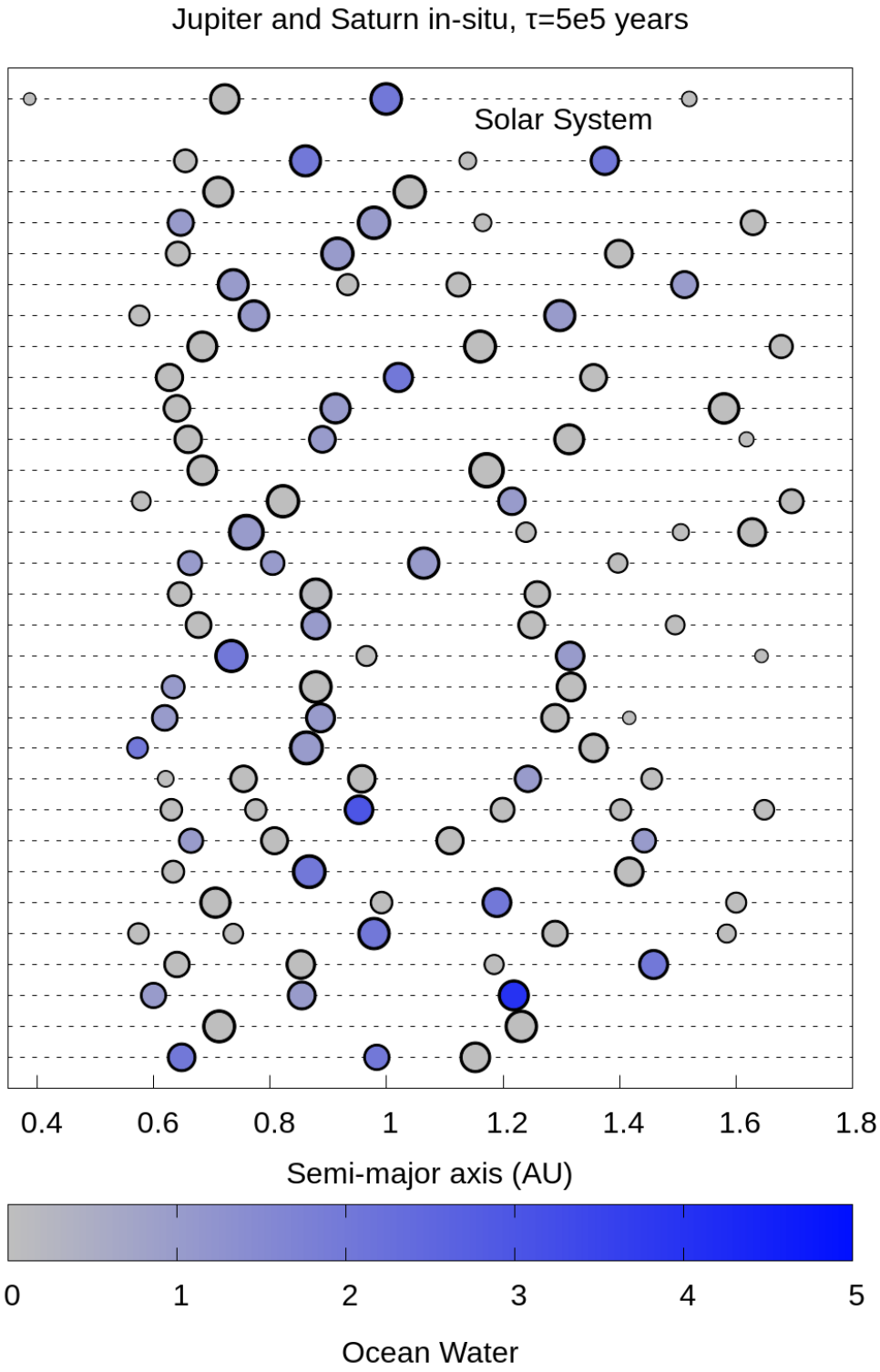

Figure B.6 – Systems formed without invoking early instability, with Jupiter and Saturn growing in situ in 500 thousand years. The plot shows the number and position of the planets for each simulation using the same numerical setup. The color represents the amount of water delivered by the C-type planetesimals originating from the H_2O zone ring. The amount of water was calculated using a distribution of 1 Earth Mass distributed across the planetesimals in the H_2O zone ring.

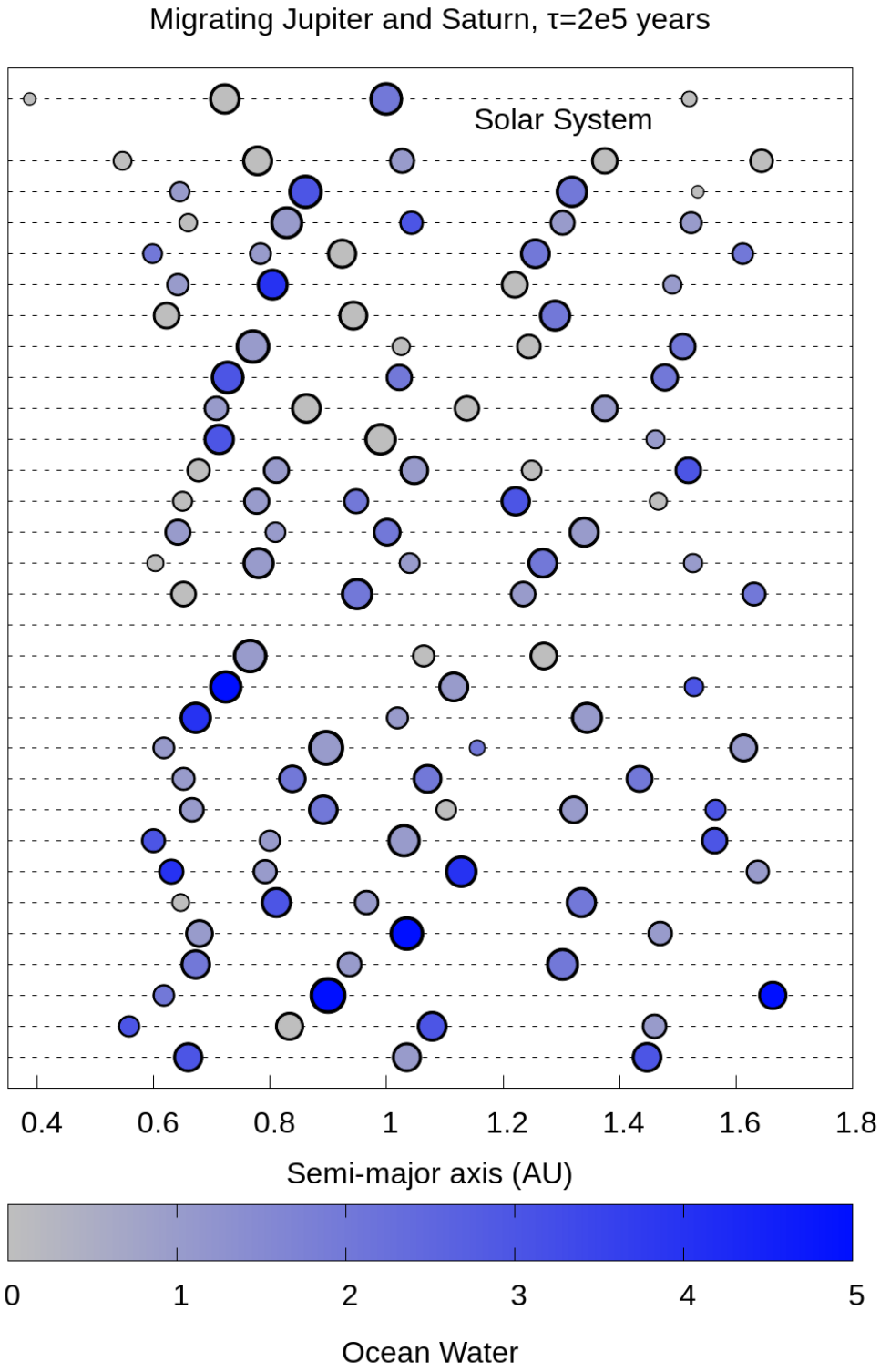

Figure B.7 – Systems formed without invoking early instability, migrating Jupiter and Saturn and growing in 200 thousand years. The plot shows the number and position of the planets for each simulation using the same numerical setup. The color represents the amount of water delivered by the C-type planetesimals originating from the H_2O zone ring. The amount of water was calculated using a distribution of 1 Earth Mass distributed across the planetesimals in the H_2O zone ring.

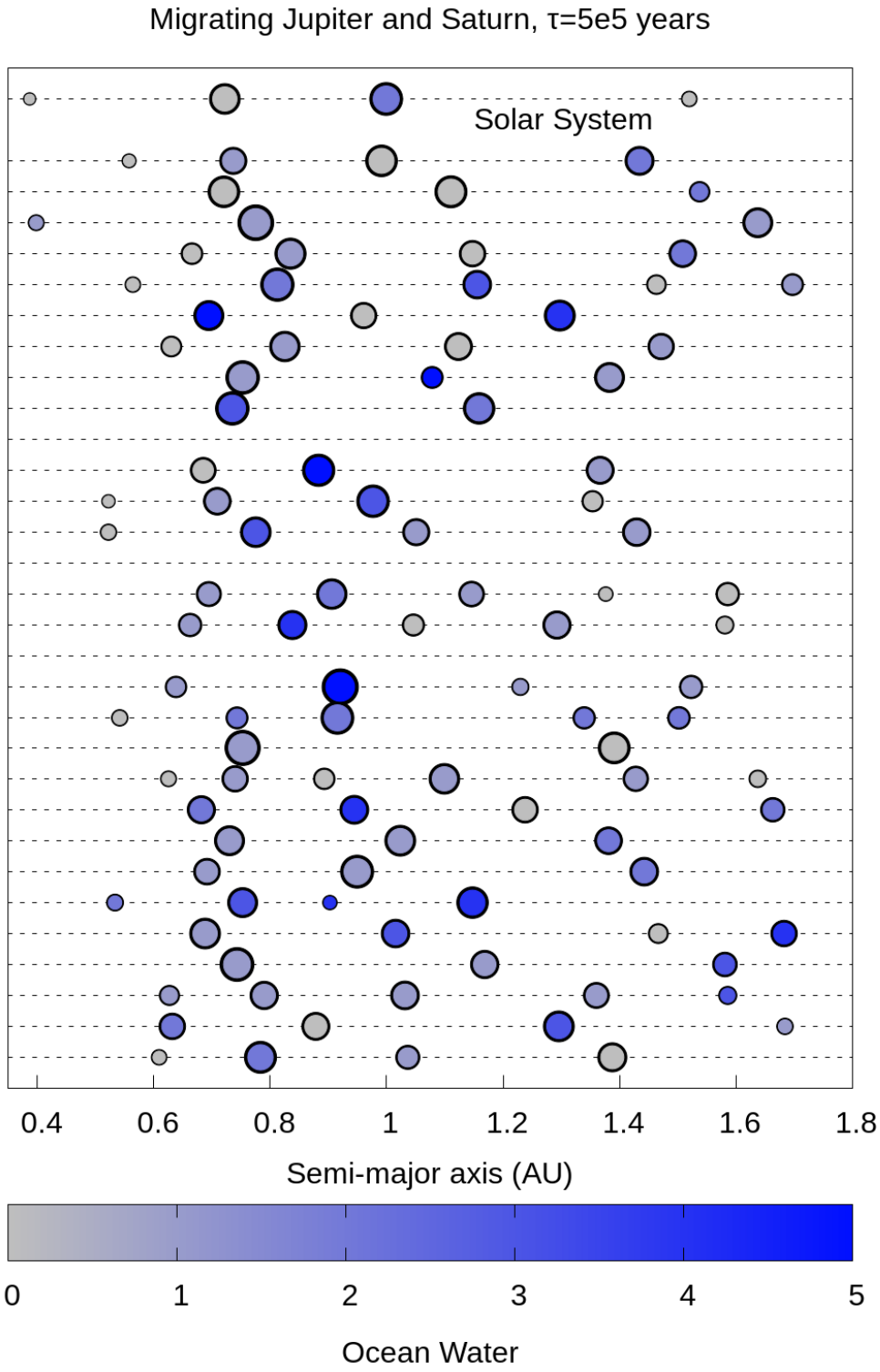

Figure B.8 – Systems formed without invoking early instability, migrating Jupiter and Saturn and growing in 500 thousand years. The plot shows the number and position of the planets for each simulation using the same numerical setup. The color represents the amount of water delivered by the C-type planetesimals originating from the H_2O zone ring. The amount of water was calculated using a distribution of 1 Earth Mass distributed across the planetesimals in the H_2O zone ring.

B.2 SOLAR SYSTEM ANALOGS FORMED FROM DIFFERENT SETUPS FOR THE FORMATION OF THE SOLAR SYSTEM

Here we illustrate the Solar System analogs formed in different setups for the formation of the Solar System. We consider a Solar System analog one system with at least 3 planets and a low mass planet beyond 1.4 AU. We also look to systems where we have two massive bodies in the orbits of Venus and Earth. The systems was chosen by ourselves looking at all the systems formed.

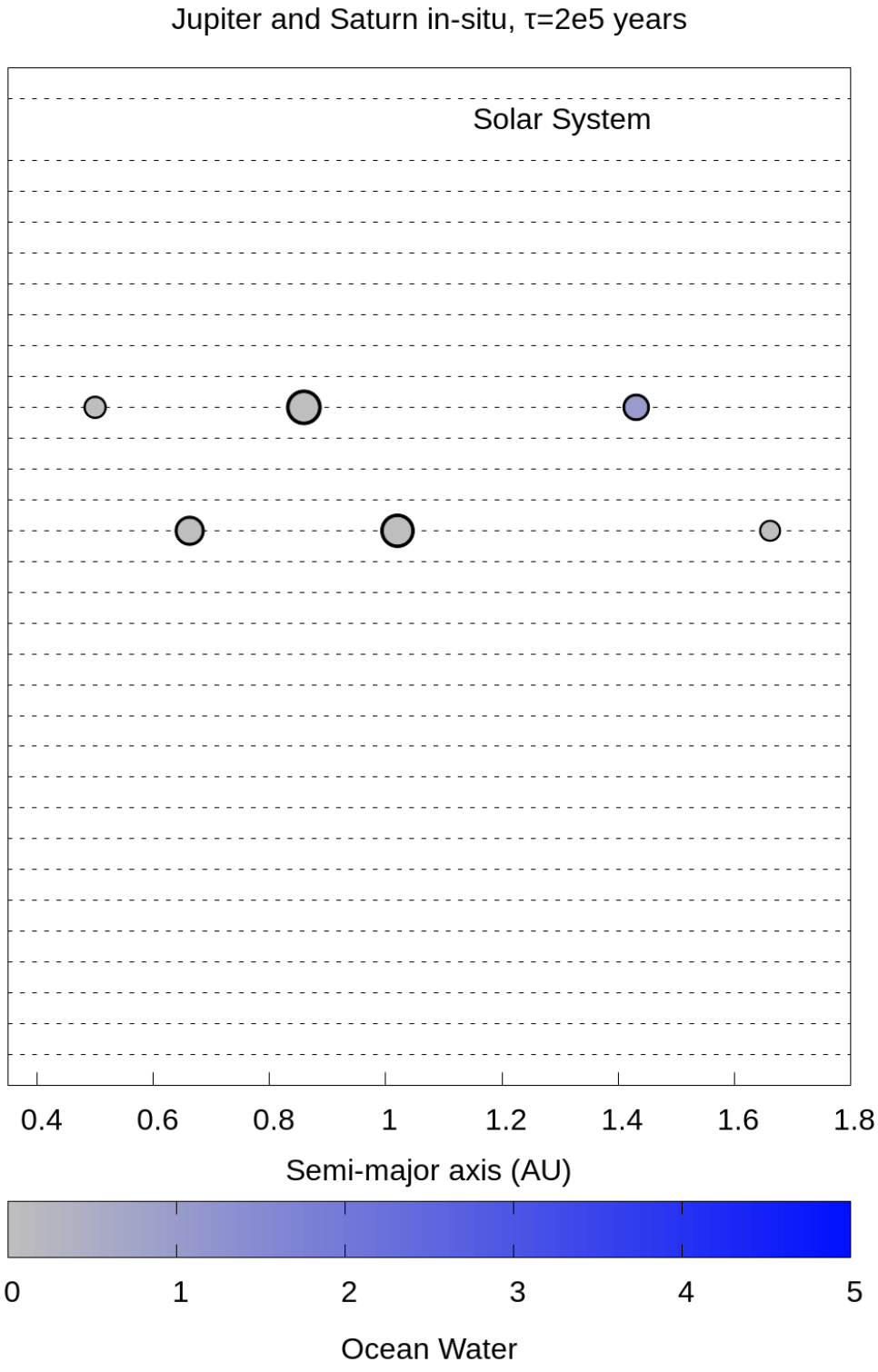

Figure B.9 – Solar System analogs formed by invoking early instability, with Jupiter and Saturn growing in situ in 200 thousand years. The plot shows the number and position of the planets for each simulation using the same numerical setup. The color represents the amount of water delivered by the C-type planetesimals originating from the H_2O zone ring. The amount of water was calculated using a distribution of 1 Earth Mass distributed across the planetesimals in the H_2O zone ring.

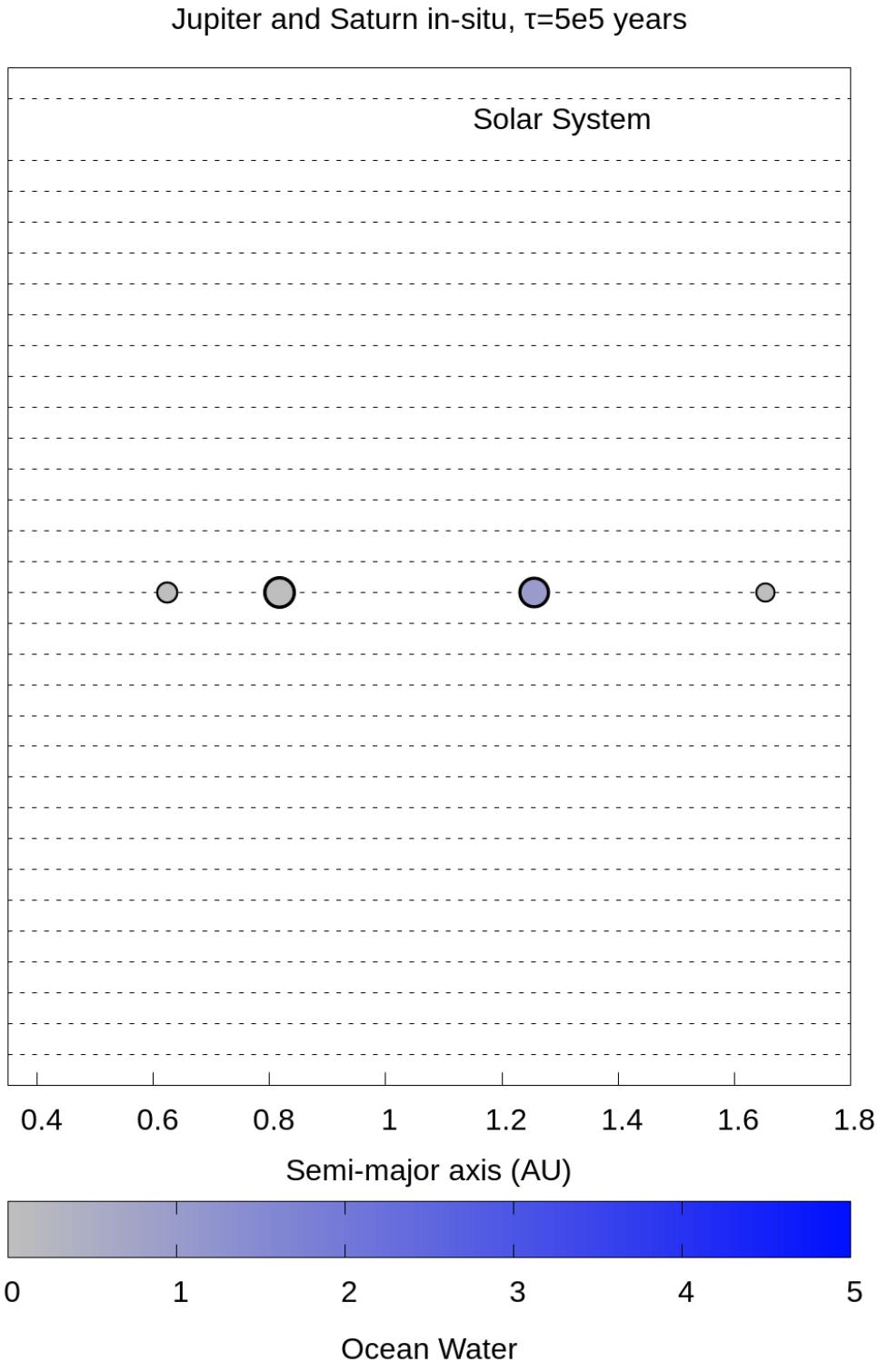

Figure B.10 – Solar System analogs formed by invoking early instability, with Jupiter and Saturn growing in situ in 500 thousand years. The plot shows the number and position of the planets for each simulation using the same numerical setup. The color represents the amount of water delivered by the C-type planetesimals originating from the H_2O zone ring. The amount of water was calculated using a distribution of 1 Earth Mass distributed across the planetesimals in the H_2O zone ring.

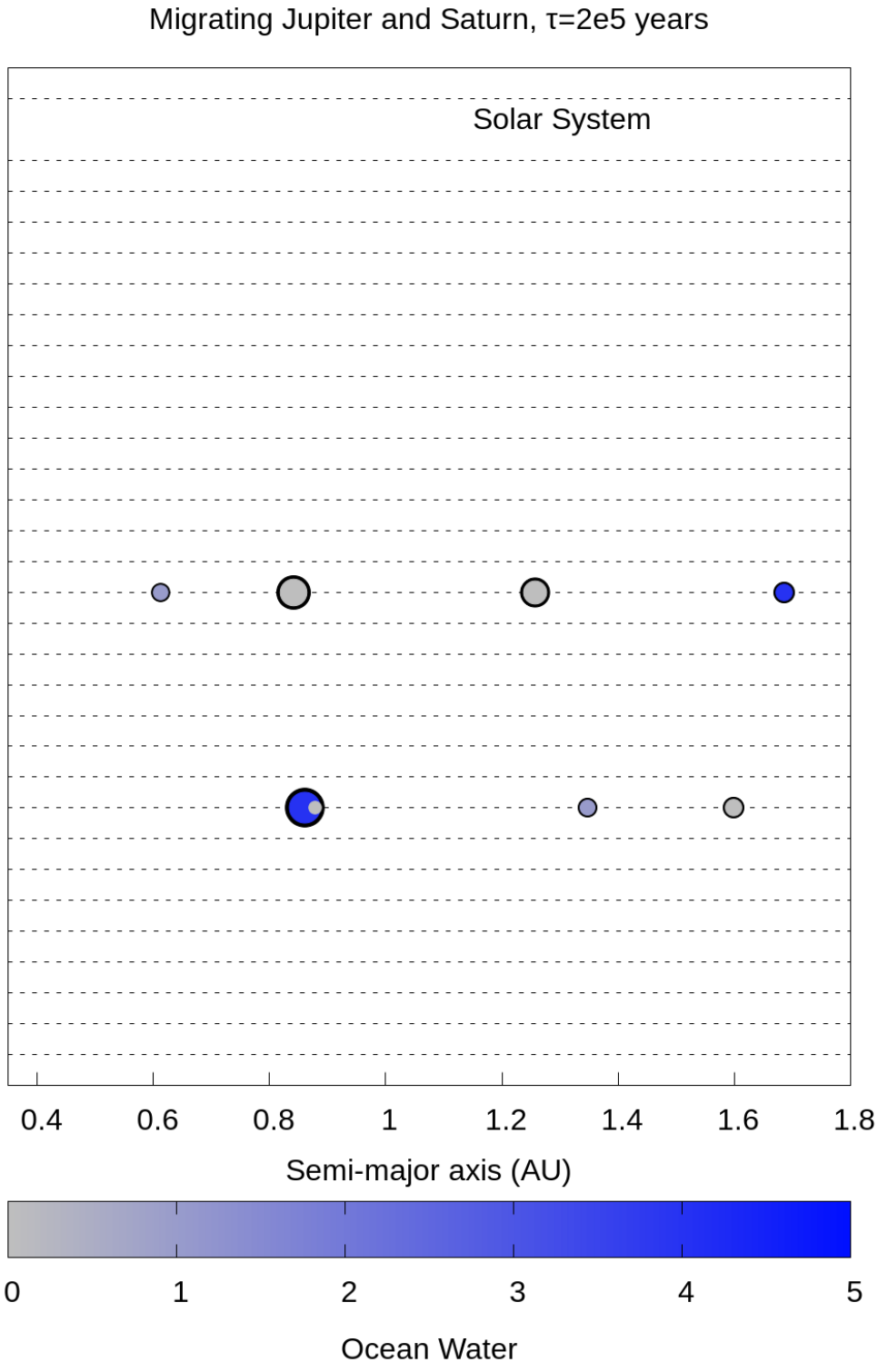

Figure B.11 – Solar System analogs formed invoking early instability, migrating Jupiter and Saturn and growing in 200 thousand years. The plot shows the number and position of the planets for each simulation using the same numerical setup. The color represents the amount of water delivered by the C-type planetesimals originating from the H_2O zone ring. The amount of water was calculated using a distribution of 1 Earth Mass distributed across the planetesimals in the H_2O zone ring.

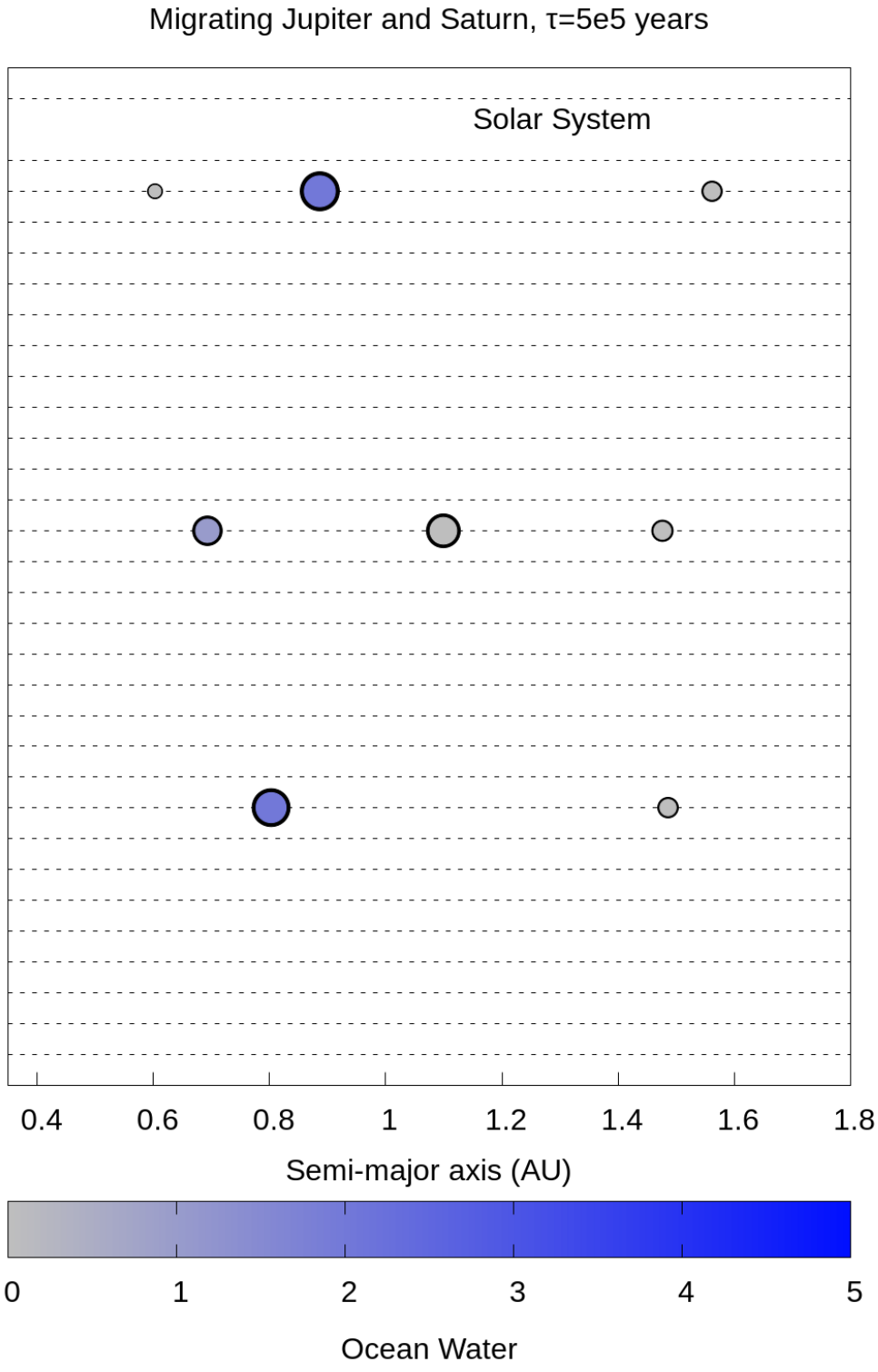

Figure B.12 – Solar System analogs formed invoking early instability, migrating Jupiter and Saturn and growing in 500 thousand years. The plot shows the number and position of the planets for each simulation using the same numerical setup. The color represents the amount of water delivered by the C-type planetesimals originating from the H_2O zone ring. The amount of water was calculated using a distribution of 1 Earth Mass distributed across the planetesimals in the H_2O zone ring.

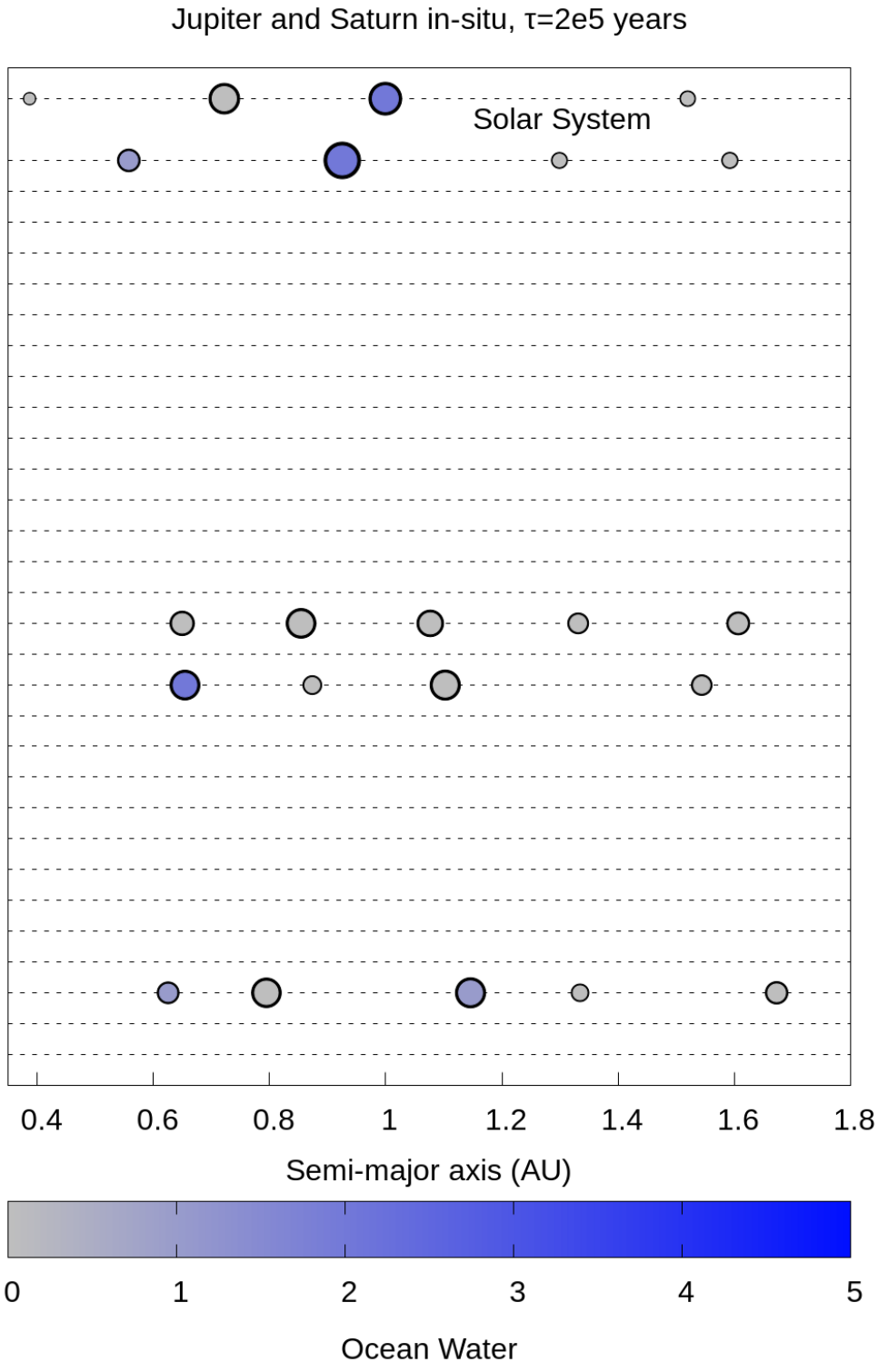

Figure B.13 – Solar System analogs formed without invoking early instability, with Jupiter and Saturn growing in situ in 200 thousand years. The plot shows the number and position of the planets for each simulation using the same numerical setup. The color represents the amount of water delivered by the C-type planetesimals originating from the H_2O zone ring. The amount of water was calculated using a distribution of 1 Earth Mass distributed across the planetesimals in the H_2O zone ring.

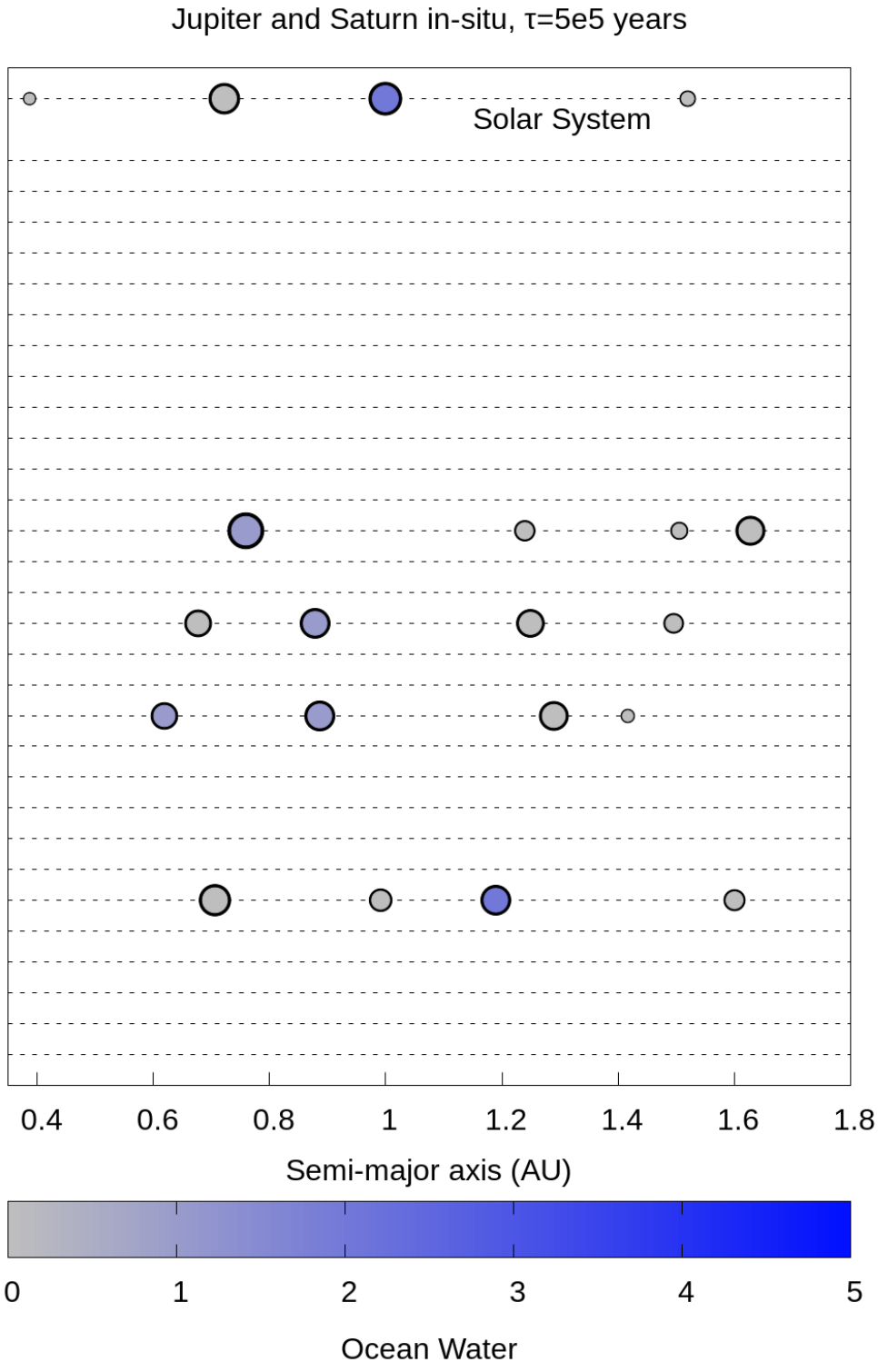

Figure B.14 – Solar System analogs formed without invoking early instability, with Jupiter and Saturn growing in situ in 500 thousand years. The plot shows the number and position of the planets for each simulation using the same numerical setup. The color represents the amount of water delivered by the C-type planetesimals originating from the H_2O zone ring. The amount of water was calculated using a distribution of 1 Earth Mass distributed across the planetesimals in the H_2O zone ring.

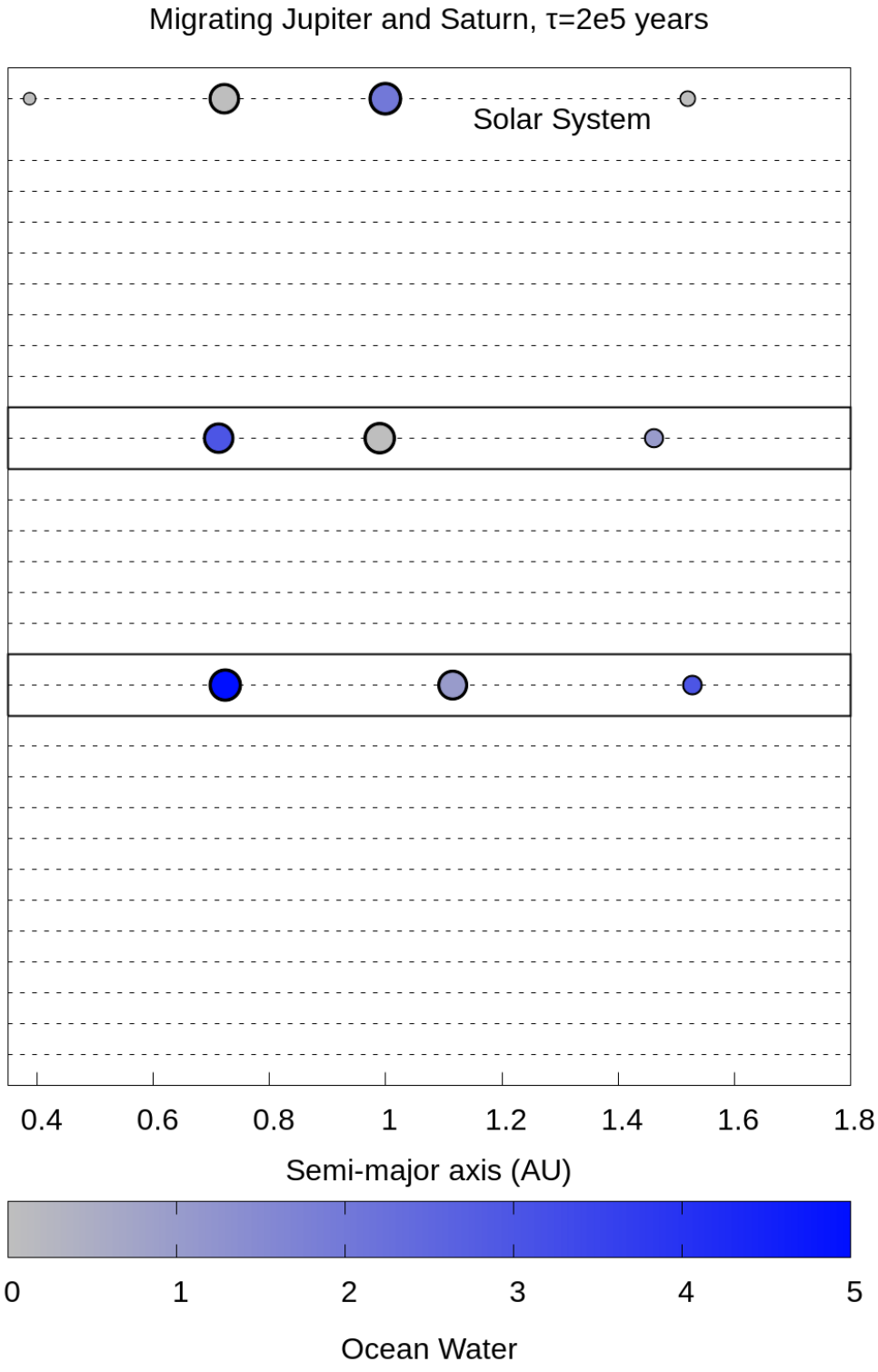

Figure B.15 – Solar System analogs formed without invoking early instability, migrating Jupiter and Saturn and growing in 200 thousand years. The plot shows the number and position of the planets for each simulation using the same numerical setup. The color represents the amount of water delivered by the C-type planetesimals originating from the H_2O zone ring. The amount of water was calculated using a distribution of 1 Earth Mass distributed across the planetesimals in the H_2O zone ring.

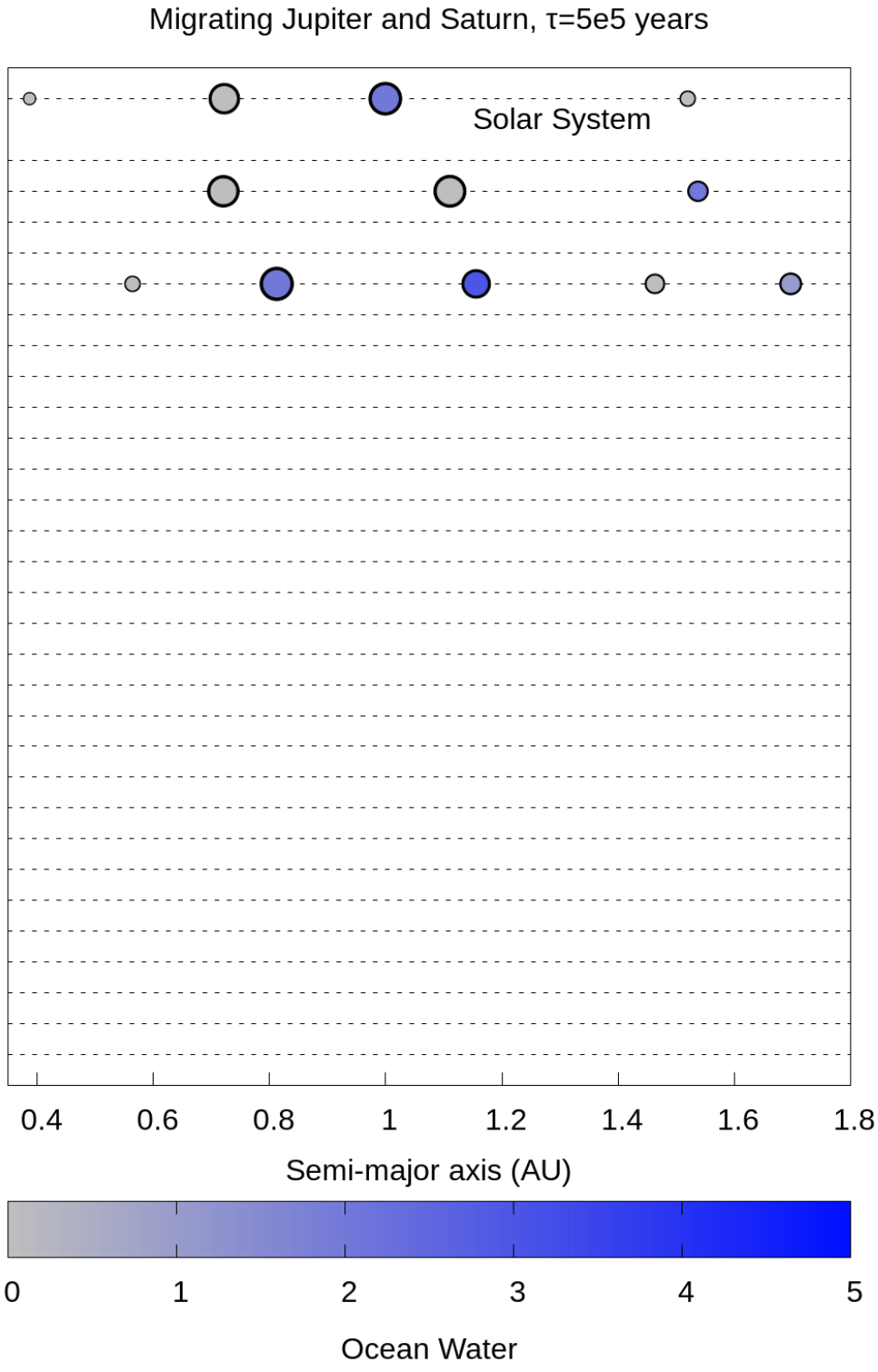

Figure B.16 – Solar System analogs formed without invoking early instability, migrating Jupiter and Saturn and growing in 500 thousand years. The plot shows the number and position of the planets for each simulation using the same numerical setup. The color represents the amount of water delivered by the C-type planetesimals originating from the H_2O zone ring. The amount of water was calculated using a distribution of 1 Earth Mass distributed across the planetesimals in the H_2O zone ring.